UNIVERSITAT POLITÈCNICA DE CATALUNYA
BARCELONATECH

Escola Tècnica Superior d'Enginyeria
de Telecomunicació de Barcelona

DESIGN AND ANALYSIS OF AN EMBEDDED SECONDARY AND TERTIARY DISTRIBUTED HIERARCHICAL CONTROL FOR AN AC MICROGRID

A Master's Thesis

Submitted to the Faculty of the

Escola Tècnica d'Enginyeria de Telecomunicació de Barcelona

Universitat Politècnica de Catalunya

by

Alex Sanchez i Benet

In partial fulfilment

of the requirements for the degree of

MASTER IN TELECOMMUNICATIONS ENGINEERING

Advisor: Cristian Chillón Antón and Francesc Guinjoan Gispert

Barcelona, May 2022

Title of the thesis: Design and Analysis of an Embedded Secondary and Tertiary Distributed Hierarchical Control for an AC Microgrid

Author: Alex Sanchez i Benet

Advisor: Cristian Chillón Antón and Francesc Guinjoan Gispert

Abstract

This project aims to develop an alternative distributed hierarchical control algorithm for a laboratory microgrid with droop control as the primary level, aiming to emulate the voltage and frequency variations of synchronous machines' inertial behaviour. The objective of the alternative control is to be able to work either in grid-connected or islanded mode without changes in the inverter control, operating always as a controllable voltage source. Moreover, it aims to unify the restoration of the voltage and power control levels to avoid undesired interactions between the two control layers. This approach will be based on consensus distributed control technique where each DER will use its local measurement and the neighbours' ones to calculate its control action.

Revision history and approval record

Revision	Date	Purpose
0	15/11/2021	Document creation
1	11/05/2022	Document revision
2	16/05/2022	Document approved

Written by:		Reviewed and approved by:	
Date	11/05/2022	Date	16/05/2022
Name	Alex Sánchez i Benet	Name	Cristian Chillón Antón
Position	Project Author	Position	Project Supervisor

Table of contents

List of Figures

List of Tables

1. Introduction

At present, most of the global electric energy generation is based on non-renewable sources, such as coal, fuel or nuclear. Obtaining energy from these sources is one of the main emitters of greenhouse gases. In addition to the decrease in fossil fuel reserves, the increase in their price and relatively low efficiency leads the society to the need to generate clean energy through renewable sources.

During the last decades, renewable sources have seen a growth in the energy industry with a trend to rise at a global level. According to the IEA report [1], in 2021, renewable electricity generation has expanded by more than 8%, being the wind for almost half of the global increase. Figure 1 shows an increase of up to 30% in the usage of renewable sources and a decrease in coal and nuclear energy in 2021.

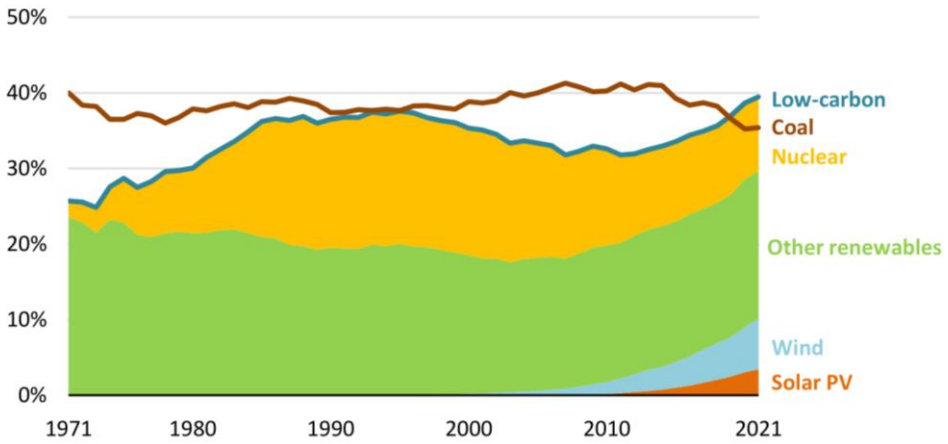

Figure 1 – Share of renewable and non-renewable sources in global electricity generation, 1971-2021 [1]

Furthermore, renewable energies have increased their share in peninsular Spain, going from 45.5% in 2020 to 48.4% in 2021 [2]. Wind energy again stands out with 24% of total electricity production, followed by hydro and solar photovoltaic with 12% and 8.3%, respectively.

The previously mentioned renewable sources create the need to evolve the conventional power grid scheme. Now, the infrastructure is concentrated in massive power plants to subsequently transport the energy to the consumers, which implies significant losses. This results in a massive high voltage grid that connects all the countries employing long transportation lines. The difficulty of extending this conventional grid and the added need for renewable generators to develop distributed and flexible systems make the concept of distributed generation come out.

The distributed grids integrate distributed energy resources (DER) that can be connected to any point of the grid, being able to generate energy locally and be integrated near consumption points. The DER can be either distributed generators (DG) or distributed storage elements (DS). The large-scale introduction of DER has the disadvantage that production and demand are not necessarily always overlapping as in the cases of photovoltaic or wind generation. The integration of the DER takes place in the transformation of the electrical grid from a centralized system to a distributed system. This adds flexibility to the grid at the expense of increased difficulty in coordinating these resources. From this need arises the concept of microgrid [3], which aims to improve the system's overall efficiency.

1.1. Microgrids

The microgrid concept refers to a group of DERs and interconnected loads that work as a single controllable entity capable of being connected and disconnected from the power grid. Thus, operating in two modes: connected to the grid or disconnected, also called island mode [4]. These systems have become an essential field of study since the grid tends to be more distributed, flexible, intelligent, and based on power-electronic devices.

The point of common coupling (PCC) marks the physical boundary between the main grid and the microgrid, and depending on the status of this point, microgrids work in one mode or another [5]. In grid-connected mode, the microgrids must be able to control the bidirectional power flow. On the other hand, the island mode allows the microgrid to work independently and requires one of the DERs to impose the voltage. A microgrid must have the capability to connect or disconnect depending on the situation. For example, the disconnection of the grid in the event of a failure or the synchronization of the microgrid voltage for the correct reconnection to the grid.

Moreover, the microgrids can be classified according to management, architecture or the type of voltage they supply [6]:

- Types of management: The control of a microgrid needs to be conceived by a manager that administrates the energy, the excess of storage and the other parts of the system, as well as the proper connection or disconnection to the power grid. In order to achieve all these objectives, the management can be intelligent and centralized if one element controls the microgrid; or distributed if each element contributes to the control.
  The microgrid distribution or topology also affects the management. Among these possible topologies, the star, the ring or the bus distributions can be considered.

- Types of architecture: Depending on the kind of loads connected, the location of the microgrid, the available infrastructure and the ownership of the land, three types of architecture can be defined:
  - The utility microgrids are a way to integrate different distributed energy resources and obtain large-scale deployments.
  - Industrial/commercial microgrids prioritize power quality, reliability and flexibility and take advantage of the capability to be connected and disconnected to the grid.
  - Finally, remote microgrids focus on the supply of the geographical areas or communities without electrical infrastructure.

- Types of voltage: A microgrid can also be classified according to the voltage link supply DC or AC. DC microgrids are starting to be an attractive way to distribute energy due to the high penetration of DG. On the other hand, AC microgrids are intended to provide electrical energy for common residential or industrial consumption.

In conclusion, microgrids can transform current infrastructure into more efficient systems, improving reliability, stability, compatibility, flexibility, scalability, efficiency and economics [7]. However, the microgrids also have some drawbacks like the need for DSs, which can cause large space requirements or the microgrid's low inertia.

In electrical systems, the generators rotate in synchronism under normal operating conditions and generate the power demanded by the loads. If this power increases but the mechanical power provided by the turbines remains constant, the increased energy demand of the system can only be obtained from the kinetic energy stored in the rotor mass. This implies a decrease in the rotational speed of the generators that causes a drop in the electrical frequency of the system [8]. When microgrids work in stand-alone mode, they do not have this inertia since electrical machines do not form them. This must be emulated by controlling the power supplied by the generators.

The hierarchical control scheme is the most used control scheme to resolve the presented challenges in AC microgrids when connected to the power grid or working stand-alone [9]. Among these challenges, the control and stability of variables such as frequency and voltage or the power flow between the DER and the grid and the switching between operation modes are the ones that stand out the most. In particular, when microgrids work in island mode, the responsibility for generating the voltage must be of all elements working as voltage sources.

This way, this master's thesis pretends to develop a control approach based on the hierarchical control scheme that allows the system elements to work as voltage sources at any time and in both grid-connected or island mode.

1.2. Objectives

This master's thesis aims to design and analyse a hierarchical control for an AC laboratory microgrid that does not require modifications to work in both operating modes by unifying the upper layers of the hierarchical control. For this purpose, this document has the following objectives:

- Research on the principles of the hierarchical control approaches and their layers.
- Describe the microgrid system under study.
- Present the proposed control approach.
- Design the control of the AC microgrid for a single generator.
- Validate the design in a single generator simulation setup.
- Simulate and study the functional behaviour of the designed control in the microgrid system setup.

1.3. Organization and planning

Considering all the previously presented objectives, this document is arranged in the following sections:

1. Introduction: In this section, the theme, the objectives, and the organization of this thesis are introduced.
2. Principles of AC microgrid hierarchical control: This chapter summarises the principles of hierarchical control.
3. Proposed AC microgrid hierarchical control: The *Proposed AC microgrid hierarchical control* section presents the microgrid under study, the proposed control approach, and the calculations and assumptions taken to design the control.
4. Results: The one generator setup and the microgrid system setup are presented in this chapter. Besides, the validation and simulations are shown and commented.
5. Budget: This section exhibits the approximate cost of the used software and the researching, designing and simulating tasks.

6. Conclusions and future development: To conclude, this last chapter summarizes the works carried out and proposes future research lines.

Regarding the planning of the master's thesis, the following Gantt diagram has been developed:

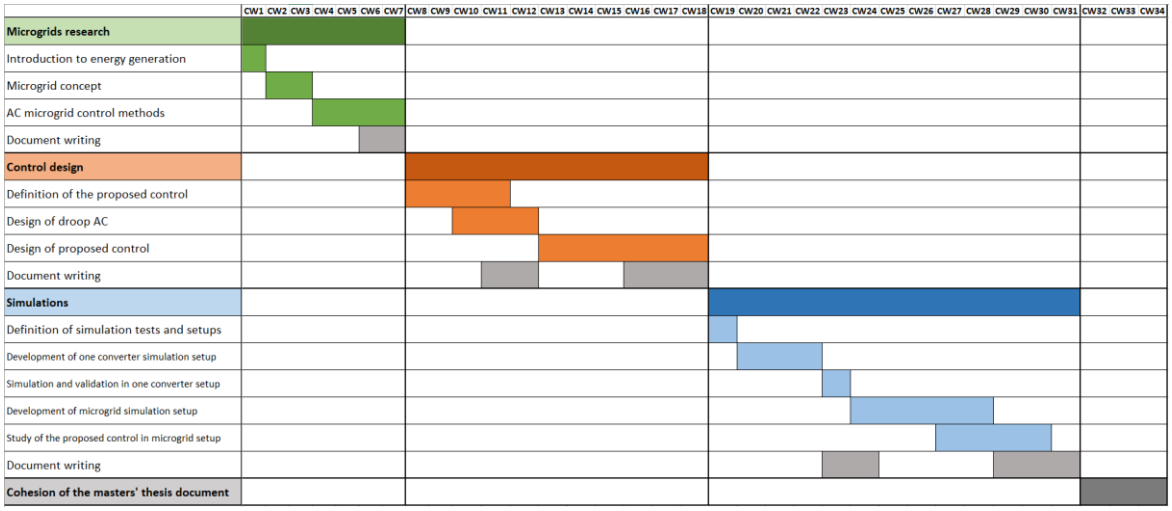

Figure 2 – Gantt diagram planning

As can be seen, the planning has been divided into 34 calendar weeks (CW) in which the tasks have been developed.

2. Principles of AC microgrid hierarchical control

The hierarchical control comprises primary control, secondary control, and tertiary control, as seen in Figure 3. The first layer oversees the frequency and voltage stability and the power distribution. The second layer aims to restore the frequency and voltage levels to the desired ones, and it can include a synchronisation control loop to switch from grid-connected mode to island mode and vice versa. Finally, the tertiary control deals with the power flow between the distributed generators and the grid at the PCC. It should be noted that even though all the layers can be applied together, each one works at a different bandwidth, the primary control being the fastest and the tertiary control the slowest.

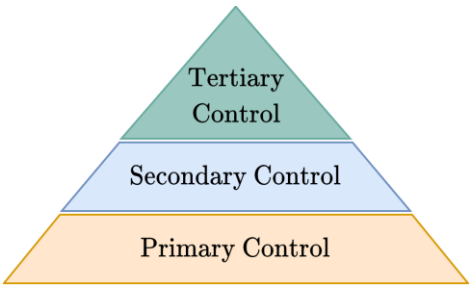

Figure 3 - Hierarchical control

2.1. Principles of primary control

The primary layer that forms the hierarchical control is responsible for the power-sharing and stabilisation of voltage frequency and amplitude in each converter. It shares the total load demand among sources in proportion to their power ratings and is commonly used to avoid the power converters overstressing and ageing. Thus, the primary control is formed by internal loops, usually consisting of a voltage and a current loop, the virtual impedance loop, and the control known as droop control, which deals with the power exchange. Figure 4 shows the completed structure of the primary control loop.

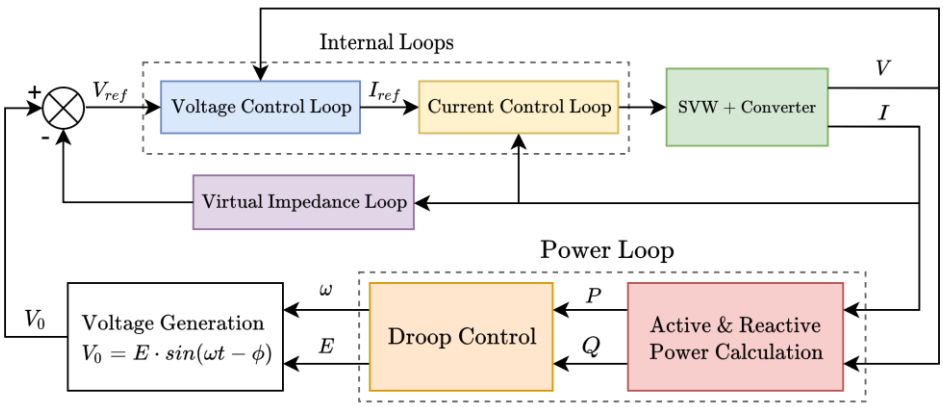

Figure 4 - Primary Control Block Diagram Completed

The internal loops have the function of controlling the converters of each DER so that the frequency and voltage output are stable. They can be embedded in the same processor to improve the dynamics of the microgrid. On the other hand, the virtual impedance loop allows adapting the output impedance, meaning the inductance and resistance, of the line to increase the droop control efficiency and improve power quality. The power loop based on the already mentioned droop control is based on conventional electrical grids formed by

synchronous machines and intends to imitate the dynamics of these systems. AC microgrids, unlike traditional grids, use power electronic converters to control their variables. Still, despite its rapid response to any variation, it has certain limitations, such as the low inertia of the system or the intermittency of distributed generators in the case of renewable sources.

Droop control

Microgrids formed by several inverters carry out the power-sharing control and stabilisation of the voltage frequency and amplitude through control methods with or without communications. Control methods solely based on local measurements show better reliability since they do not depend on communications in exchange for permitting a small error. These techniques are generally called droop control methods.

The droop control subtracts proportional parts of the output average active and reactive powers from the frequency and voltage amplitude to emulate virtual inertia. This way, the behaviour of the synchronous generators is imitated in exchange for frequency and voltage steady-state deviations.

Although droop control is the most used control method, there are alternatives. For example, in the bibliography, there are methods in which each inverter is considered an agent of a multiagent system and exchanges data with a few other neighbour generators. This information is used to update the local voltage set points and synchronise the normalised power and frequency of DERs [10].

This thesis focuses on droop control, and in this section, the basis of this control method is developed. The basic principles of the droop control, [11], can be deduced from the power equation through a line from a point A to a point B expressed at (2.1), as well in Figure 5.

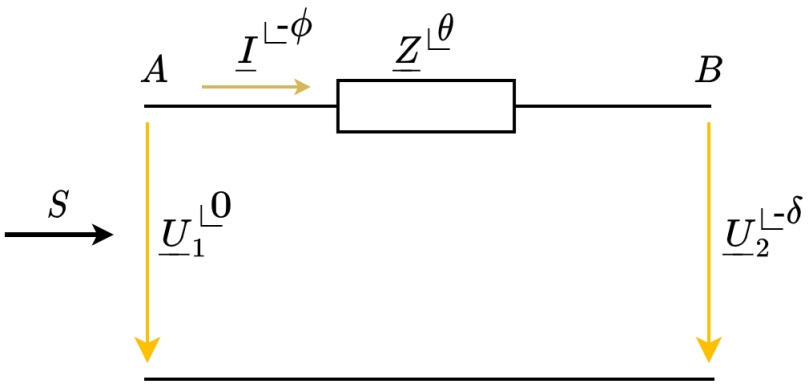

Figure 5 – Power flow through a line

Figure 5 shows a line represented by an impedance Z that connects two nodes. A voltage source imposes the voltage U_A to node A, and node B indicates the connection point of the rest of the system. This way, the equation of the complex power flowing is represented by:

$$\underline{S} = P + jQ = \underline{U_A}\underline{I}^* = \underline{U_A}\left(\frac{\underline{U_A} - \underline{U_B}}{\underline{Z}}\right)^* = U_A\left(\frac{U_A - U_B e^{j\delta}}{Ze^{-j\theta}}\right) = \frac{{U_A}^2}{Z}e^{j\theta} - \frac{U_A U_B}{Z}e^{j(\delta+\theta)} \quad (2.1)$$

From the previous equations, and using the Euler's formula that states that for any real number x: $e^{jx} = \cos x + j \sin x$, the active and reactive power flowing into the line can be written as:

$$P = \frac{{U_A}^2}{Z}\cos\theta - \frac{U_A U_B}{Z}\cos(\delta + \theta) \tag{2.2}$$

$$Q = \frac{{U_A}^2}{Z}\sin\theta - \frac{U_A U_B}{Z}\sin(\delta + \theta) \tag{2.3}$$

From equations (2.2) and (2.3), the trigonometric identities that declare: $\cos(x \pm y) = \cos x \cdot \cos y \mp \sin x \cdot \sin y$ and $\sin(x \pm y) = \sin x \cdot \cos y \pm \cos x \cdot \sin y$ and taking into account that: $R = Z \cdot \cos\theta$, $X = Z \cdot \sin\theta$ and $Z^2 = R^2 + X^2$, then the next equations can be obtained:

$$\begin{aligned} P &= \frac{{U_A}^2 Z}{Z^2}\cos\theta - \frac{U_A U_B Z}{Z^2}\cos(\delta + \theta) \\ &= \frac{U_A}{Z^2}[U_A Z\cos\theta - U_B Z\,(\cos\delta\cos\theta - \sin\delta\sin\theta)] \\ &= \frac{\boldsymbol{U_A}}{\boldsymbol{R^2 + X^2}}[\boldsymbol{R(U_A - U_B\cos\delta) + XU_B\sin\delta}] \end{aligned} \tag{2.4}$$

$$\begin{aligned} Q &= \frac{{U_A}^2}{Z}\sin\theta - \frac{U_A U_B}{Z}\sin(\delta + \theta) \\ &= \frac{U_A}{Z^2}[U_A Z\sin\theta - U_B Z\,(\sin\delta\cos\theta + \cos\delta\sin\theta)] \\ &= \frac{\boldsymbol{U_A}}{\boldsymbol{R^2 + X^2}}[-\boldsymbol{RU_B\sin\delta + X(U_A - U_B\cos\delta)}] \end{aligned} \tag{2.5}$$

Finally, considering that the line is inductive $X \gg R$, which means that the resistance may be neglected, and the power angle δ is small so that $\sin\delta \approx \delta$ and $\cos\delta \approx 1$, the equations (2.4) and (2.5) are rewritten as:

$$\delta \approx \frac{X}{U_A U_B}P \tag{2.6}$$

$$U_A - U_B = \frac{X}{U_A}Q \tag{2.7}$$

The expressions (2.6) and (2.7) show that the power angle depends on the active power that flows through the line, while the potential difference between nodes A and B depends on the reactive power. Therefore, the frequency and voltage amplitude are determined by controlling the inverter's power. These conclusions lead to the control basic equations of the droop control:

$$\omega - \omega_0 = -k_p(P - P_0) \tag{2.8}$$

$$E - E_0 = -k_q(Q - Q_0) \tag{2.9}$$

Where ω and ω_0 are the actual and the nominal frequency values, whereas E and E_0 are the actual and the nominal voltage values at node A respectively. The equations (2.8) and (2.9) are represented as a block diagram as follows:

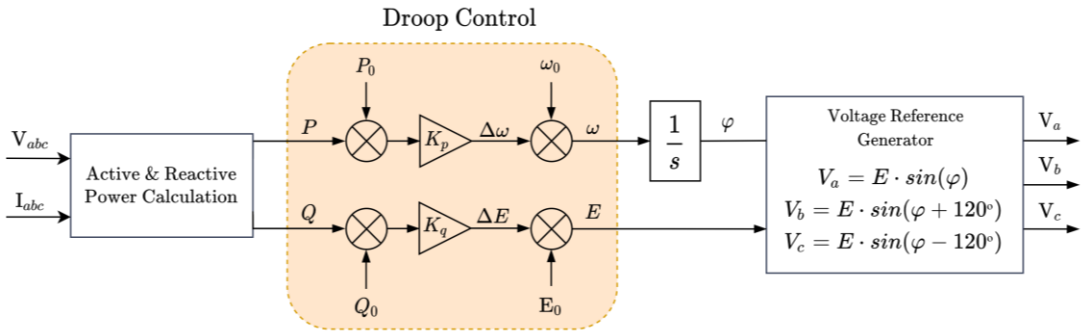

Figure 6 - Primary regulation using droop control block diagram

As noted in Figure 6, the differences between power set points, P_0, and Q_0, and the active and reactive power at the output filter capacitor employing the phase voltages and currents (V_{abc} and I_{abc}), P and Q, are multiplied by the droop control gains, k_p and k_q respectively, to obtain the frequency and voltage amplitude deviations $\Delta\omega$ and ΔE that corresponds to the virtual inertia. Then, these are subtracted from the nominal frequency of the line, ω_0, and the voltage amplitude at the node A, E_0, to obtain the new output frequency and voltage amplitude ω and E. In the case of frequency, it is integrated to obtain the corresponding angle ϕ. Finally, the voltage references of each phase are generated with the calculated voltage amplitude and angle.

Frequency droop control

Frequency droop control action is graphically represented as follows in Figure 7.

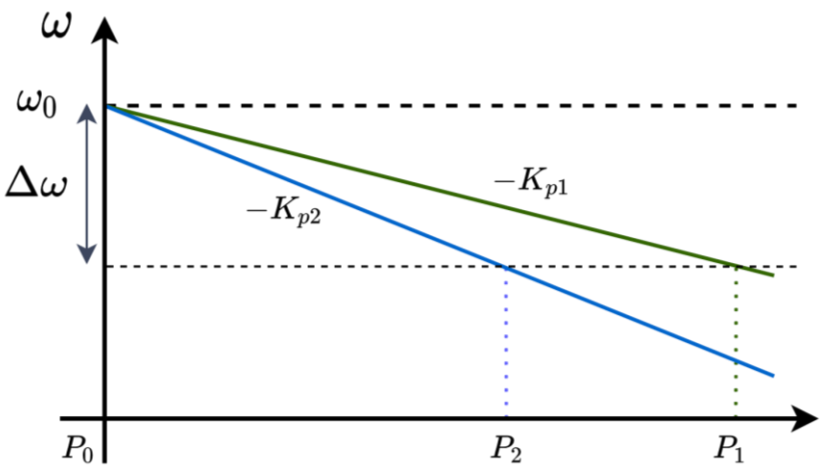

Figure 7 - Frequency droop control action

The graph in Figure 7 represents the drop of frequency of two generator units with different frequency droop gains, K_{p1} and K_{p2}. Initially, the system frequency is equal to the nominal value, ω_0, when both generators supply active power equal to the power set points P_0, usually 0 W. Once a load is added to the system, the converters provide the required active power, P_1 and P_2, proportionately distributed and the frequency at the converter output, ω_1 and ω_2, droops to a specific value. The frequency is a global variable throughout the system, and consequently, the converters contemplate the same frequency deviation, $\Delta\omega$, in

steady-state. This way, depending on the generators' nominal power, the droop gains of each one can be selected to carry out the correct distribution of the active power by following the expression (2.8). As seen in the graph in Figure 7, the higher the droop gain value, the lower the active power supplied by the converter at the same frequency value. However, there are other considerations to study when selecting the droop constant, such as the maximum frequency deviation and the system stability, settling time, and inertia.

Voltage droop control

On the other hand, the voltage droop control action is shown in Figure 8. As in the case of the frequency, the distribution of the reactive power supplied by each generator unit, Q_1, and Q_2, is realised proportionally with the voltage droop gains K_{q1} and K_{q2}. However, in this instance, the control variable is not global, and the voltage levels at the converters' outputs, E_1 and E_2, are different due to the line impedance effect. This fact makes the voltage deviation of each generator, ΔE_1, and ΔE_2, also different. Consequently, the reactive power-sharing is not accurate, which can lead to an overload of the generators. This problem can be corrected by employing the second and third layers of the hierarchical control. The voltage droop gain must also be selected considering the maximum voltage deviation, the desired reactive power distribution, the system stability, settling time, and voltage quality.

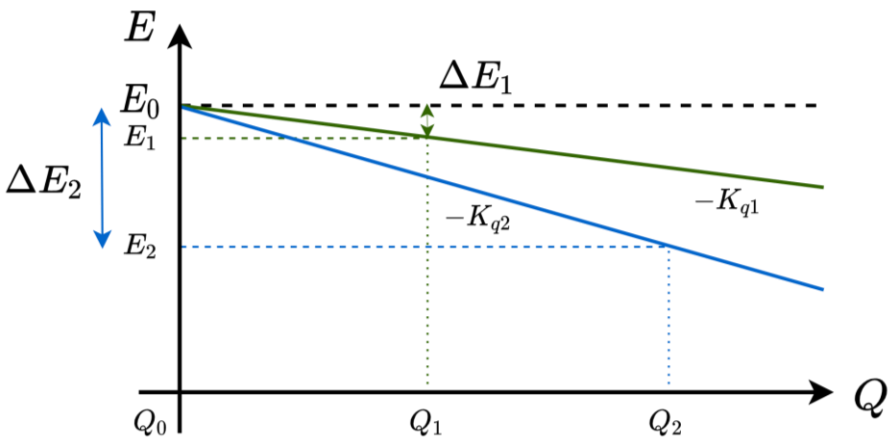

Figure 8 - Voltage amplitude droop control action

2.2. Principles of secondary control

The second layer of the hierarchical control is in charge of correcting the deviations in the steady state of voltage frequency and amplitude originated in the droop control. The secondary control can also be used to improve the accuracy of reactive power distribution, remove harmonics, improve the quality of supply, and ensure proper synchronisation of the microgrid with the electrical grid. To correct errors produced in the droop control, two terms, δ_i^{ω} and δ_i^{E}, are added to the equations (2.8) and (2.9):

$$\omega_i = \omega_0 - m_i P_i + \delta_i{}^{\omega} \tag{2.10}$$

$$E_i = E_0 - n_i Q_i + \delta_i{}^{E} \tag{2.11}$$

Frequency restoration secondary control

The expression (2.10) ensures that the DGs frequency and voltage magnitudes are restored to the nominal values.

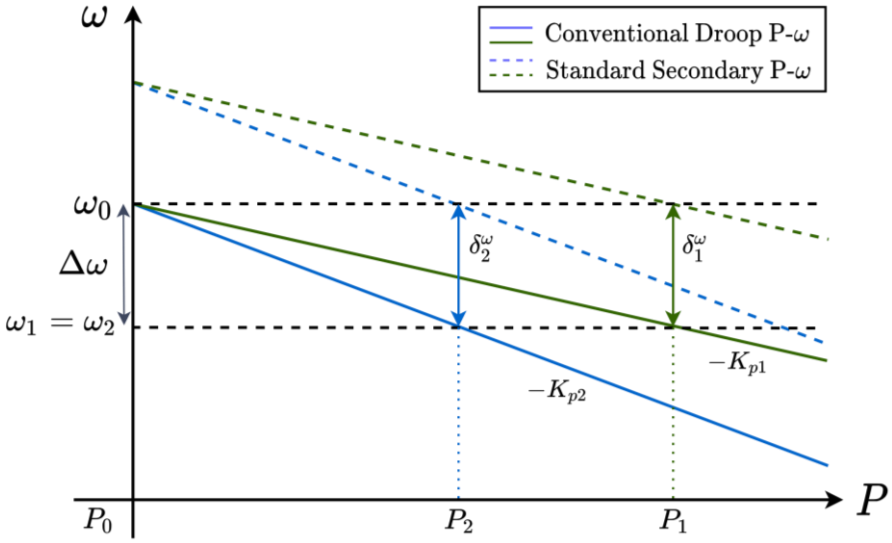

Figure 9 - Frequency restoration secondary control action

Figure 9 shows the active power distribution of two DGs carried out by the primary control in addition to the secondary control action represented as a vertical displacement. As can be seen, the second layer modifies the frequency reference of each generator unit to remove the frequency error without changing the power supplied.

Voltage restoration secondary control

In the case of the voltage restoration control, the secondary control action becomes more complex since a conflict exists between the voltage restoration and reactive power-sharing [12]. In or highlight the problematics, two secondary control approaches are outlined.

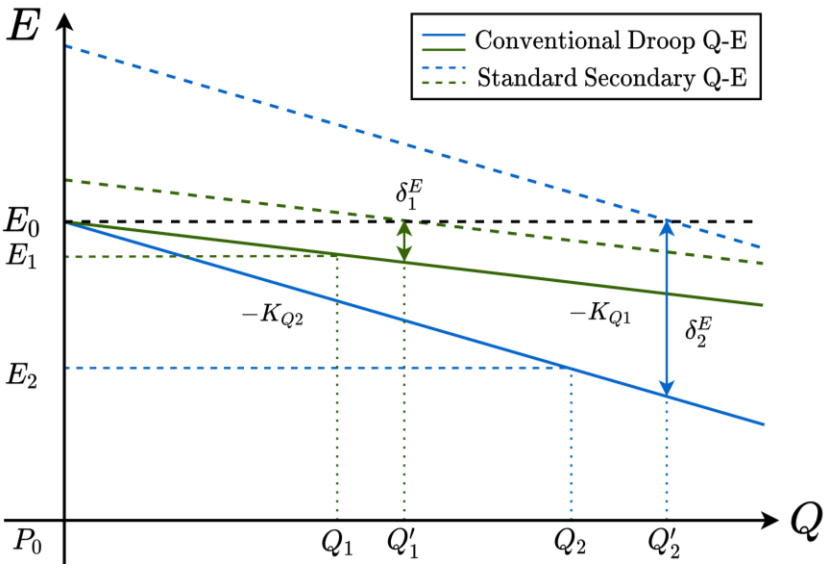

Figure 10 - Voltage restoration secondary control action

The first one is shown in Figure 10 and is focused on voltage restoration. The application of voltage-regulating secondary control ensures that both DGs voltages are restored to the

nominal value but leads to significant errors in reactive power sharing due to the line impedance effect.

In contrast, the second approach is focused on reactive power-sharing, represented in Figure 11. The application of this secondary control enforces the power-sharing at the expense of worsening the voltage profiles at the converter outputs.

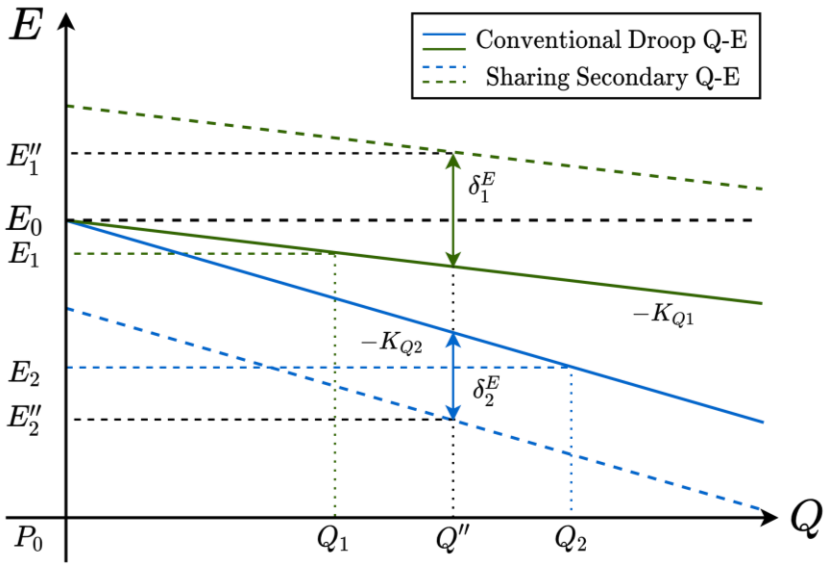

Figure 11 - Power sharing secondary control action

The secondary control can be classified into various categories depending on the architecture. Among them are the centralised, distributed, and decentralised structures [13].

2.2.1. Centralised secondary control

The centralised structure uses a microgrid central control (MGCC) which collects the data sent by the DGs through a high-speed communication interface and coordinates them to restore the frequency and voltage amplitude. These communications follow a master-slave scheme where do not exist direct communications between the generator units, but the communication channels are only between the MGCC and the inverters. Figure 12 represents the centralised structure:

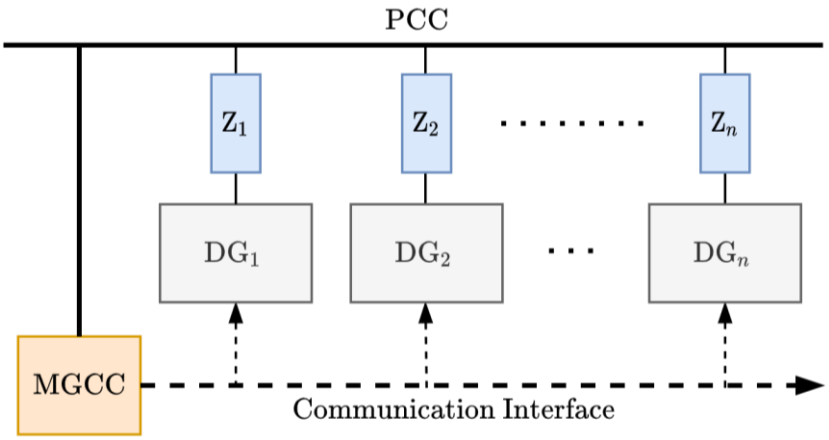

Figure 12 - Centralized Secondary Control Structure

Commonly, the controlled node in this type of secondary control is at the microgrid PCC, where the main grid is connected. This way, the terms for each DG controlled are calculated with the same error, measured in the PCC as follows:

$$\delta_i{}^{\omega} = K_{\omega}(s)\left(\omega_{ref} - \omega_{PCC}\right) \tag{2.12}$$

$$\delta_i{}^{E} = K_{E}(s)\left(E_{ref} - E_{PCC}\right) \tag{2.13}$$

being $K_{\omega}(s)$ and $K_E(s)$ the controllers of the P-ω and Q-E loops, respectively. Their type and control parameters are selected according to a desired secondary control dynamic.

If the topology of the microgrid is known and since the voltage profile is not a global variable, the output voltage of each DG can be controlled to achieve the desired voltage profile. Each DG receives a different term depending on its voltage reference value, E_{ref}, and the voltage read at the converter *i* output, E_i, as seen in the following equation:

$$\delta_i{}^{E} = K_{E}(s)\left(E_{i\,ref} - E_i\right) \tag{2.14}$$

In terms of design, this approach is practical since several aspects of the microgrid can be controlled with a single entity. However, microgrids with elements separated by large distances or by difficult areas, such as water surfaces, may be formed by extensive communication systems and complex interfaces, leading to high costs. Furthermore, using this architecture also compromise the scalability of the system, the distributed generation, and plug-and-play, which are the paradigms of the microgrid concept, since the dependence on the MGCC [14]. The centralised secondary control scheme addresses harmonic cancellation, unbalanced current reduction, and power quality in the literature [15].

2.2.2. Distributed secondary control

The distributed architecture is based on multiagent system theory (MAS). It improves the system adaptability and robustness compared to the centralised scheme since the DG cooperates to control the microgrid. It does not depend on a single unit as an MGCC. This way, a microgrid can be represented from the point of view of graph theory symbolising sources DG as vertices and communication between them as edges, as seen in Figure 13.

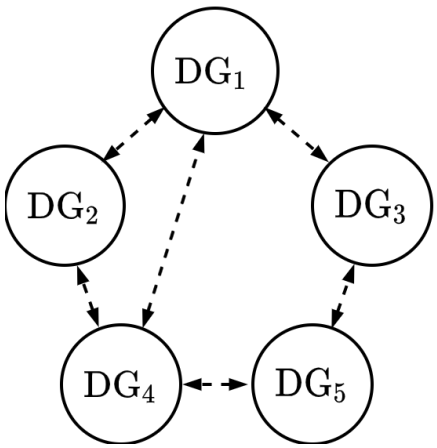

Figure 13 - Example of a multiagent system with communications

In this case, the MGCC is no longer required as each generator unit is controlled using its local data and those sent by other inverters. This makes the control more robust, considering that the tasks are divided between the sources, and it is not dependent on a single controller to do all calculations. However, the third layer of the hierarchical control and other control system elements may require a central controller. Another point favouring this architecture is adaptability since the connection or disconnection of a source does not require modifying the algorithm of any system component.

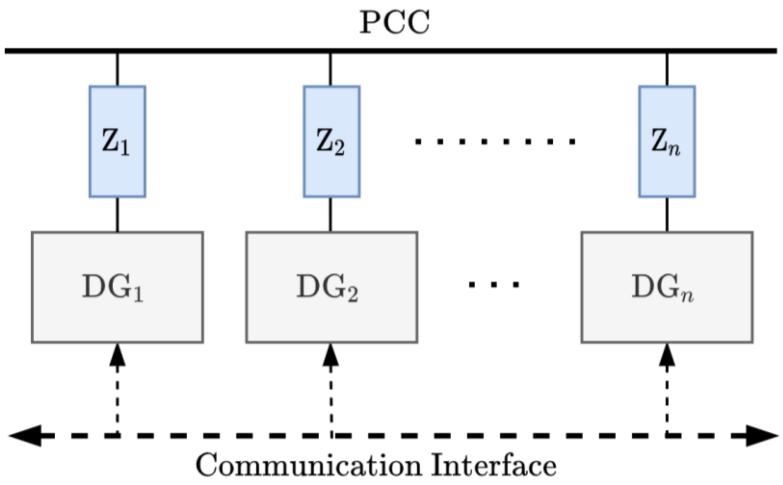

Figure 14 - Distributed Secondary Control Structure

A general scheme of this approach is shown in Figure 14. The distributed control architecture can be classified according to the techniques used to calculate the control.

a. Averaging control technique

Each DG measures its frequency and voltage amplitude in the averaging-based structure and communicates them to all other generator units. This way, each converter computes its secondary terms, calculating the average frequency and the voltage amplitude with this data as follows:

$$\delta_i{}^x = K_{i\,x}(s)\left(x_{ref} - \frac{1}{n}\sum_{j=1}^{n} x_j\right) \tag{2.15}$$

Being x the variable of interest controlled by the second layer control and $K_{i\,x}(s)$ the compensator used by converter i and n the total number of DGs connected to the microgrid.

In the case of the frequency, since it is a global variable and the same throughout the system in steady-state, it must be estimated locally by each inverter and sent to all the other inverters to calculate the average frequency to compute the secondary term as shown in the equation (2.16):

$$\delta_i{}^{\omega} = K_{i\,\omega}(s)\left(\omega_{ref} - \frac{1}{n}\sum_{j=1}^{n} \omega_j\right) \tag{2.16}$$

On the other hand, the voltage amplitude is not common in the whole system, and the impedance between DG is not necessarily the same. This fact makes precise reactive

power sharing difficult, as explained at the beginning of this section. Because of this, an alternative control (2.17) has been developed that consists of implementing a distributed average reactive power-sharing that results in the following equations [16]:

$$\delta_i{}^{E} = \delta_i{}^{Eave} + \delta_i{}^{Qave} \tag{2.17}$$

$$\delta_i{}^{Eave} = K_{i\,E}(s)\left(E_{ref} - \frac{1}{n}\sum_{j=1}^{n} E_j\right) \tag{2.18}$$

$$\delta_i{}^{Qave} = K_{i\,Q}(s)\left(Q_i - \frac{1}{n}\sum_{j=1}^{n} Q_j\right) \tag{2.19}$$

Where δ_i^{Eave} is the term that aims to correct the voltage amplitude while δ_i^{Qave} is the one responsible for reactive power-sharing. The secondary control term for the voltage amplitude correction is calculated from the sum of two expressions. The equation (2.18) considers the amplitude restoration, and the expression (2.19) is in charge of the reactive power-sharing. This way, power-sharing is independently achieved from voltage sensing mismatches or line impedance values of the microgrid.

b. Consensus control technique

As the average method, the consensus technique for secondary control uses local and transmitted measured signals to calculate the secondary term. However, in this case, the communication system follows a neighbour-to-neighbour scheme. Each generator unit uses the data sent by the DGs set by MAS theory, which defines the information exchange rules. This technique follows the following equation:

$$\delta_i{}^{x} = K_{i\,x}(s)\sum_{\substack{j=1\\ j\neq i}}^{n} \alpha_{ij}\left(x_j(t) - x_i(t)\right) \tag{2.20}$$

The objective of consensus control is to hold that $x_i = x_j$ in steady state, being *i* the generator unit in which the secondary term is applied and *j* all other DGs. As can be seen in equation (2.20), the term α_{ij} is related to the associated adjacency matrix, which is the matrix that describes the communication links between the elements of the microgrid.

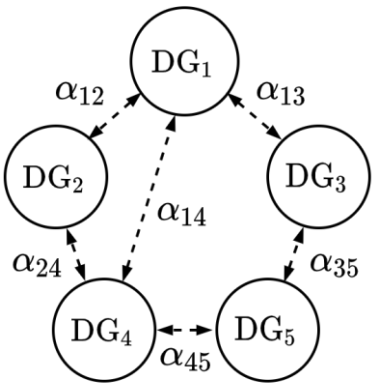

$$\alpha_{ij} = \begin{pmatrix} 0 & \alpha_{12} & \alpha_{13} & \alpha_{14} & 0 \\ \alpha_{21} & 0 & 0 & \alpha_{24} & 0 \\ \alpha_{31} & 0 & 0 & 0 & \alpha_{35} \\ \alpha_{41} & \alpha_{42} & 0 & 0 & \alpha_{45} \\ 0 & 0 & \alpha_{53} & \alpha_{54} & 0 \end{pmatrix}$$

Figure 15 - Example of a multi agent and its associated adjacency matrix

Figure 15 shows an example of a system with five DGs and a communication system in addition to the adjacency matrix associated. As seen in this matrix, the term is nonnegative when there is a relationship between generators and can weigh from 0 to 1. This matrix allows also representing unidirectional connections in which $\alpha_{ij} \neq \alpha_{ji}$.

The equation (2.21) for the frequency secondary control term proposed in [17] considers the frequency correction and the consensus of the DGs connected to ensure the same shift in the droop curves, guaranteeing the active power-sharing. The adjacency matrix and the controller parameters $K_{i\,\omega}(s)$ do not determine the algorithm's performance; they just control the transient behaviour.

$$\delta_i{}^{\omega} = K_{i\,\omega}(s)\left(\left(\omega_{ref} - \omega_i\right) + \sum_{j=1\ j\neq i}^{n} \alpha_{ij}\left(\delta_j{}^{\omega} - \delta_i{}^{\omega}\right)\right) \tag{2.21}$$

As the droop control cannot accurately share reactive power between generator units, equation (2.22) is also proposed in [17] to calculate the secondary control term for the voltage amplitude restoration and reactive power share. The first part of the expression is responsible for correcting the voltage amplitude deviation. In contrast, the second one aims to control the reactive power supplied by DGs to distribute the reactive power supply proportionally to their nominal power. This way, the secondary control achieves a compromise between reactive power sharing and voltage regulation based on the relative size of the adjacency matrix β_{ij} and the weight b_{ij}.

$$\delta_i{}^{E} = K_{i\,E}(s)\left(b_{ij}\left(E_{ref} - E_i\right) + \sum_{j=1\ j\neq i}^{n} \beta_{ij}\left(\frac{Q_j}{Q_{j\,nom}} - \frac{Q_i}{Q_{i\,nom}}\right)\right) \tag{2.22}$$

The consensus control allows for reducing the size of the communication infrastructure since it is not required that all the DGs have a channel between them. Furthermore, this approach has better adaptability to different microgrid topologies thanks to the adjacency matrix.

2.2.3. Decentralised secondary control

In the previous secondary control structures, communications provide a channel to exchange the required data to achieve control objectives. Nevertheless, these communications may contain delays and packet losses that can affect the control's correct operation, compromising its stability and dynamics and leading to a system collapse. In microgrids formed by slow elements such as synchronous machines, communications errors are not as severe as the impact in inverted-based systems, where they can increase the oscillations or even lead to instability.

The decentralised control structure avoids communication problems since each inverter independently restores its frequency and voltage amplitude by employing its local measurements. Figure 16 shows an example of this kind of control.

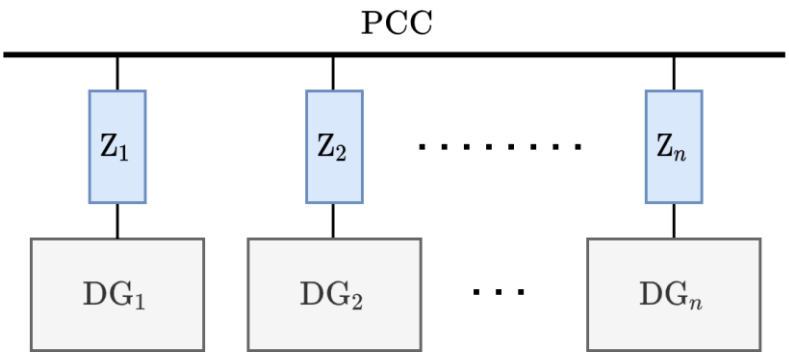

Figure 16 - Decentralized Secondary Control Structure

2.3. Principles of tertiary control

Finally, the last layer of the hierarchical control is the tertiary control. It deals with the power flow of the microgrid to optimise the energy supply considering economic issues, operation scheduling, and grid requirements [14]. This control loop can also be used to improve the power quality at the PCC [18]. Besides, the tertiary control works with a longer timescale than the first and second layers, in the range of minutes to hours.

In grid-connected mode, the power flow is controlled by adjusting the voltage frequency and amplitude of the microgrid. Therefore, to modify these references, the control laws of this layer can be expressed as follows:

$$\omega_{ref} = K_P(s)\left(P_{ref} - P\right) \tag{2.23}$$

$$E_{ref} = K_Q(s)\left(Q_{ref} - Q\right) \tag{2.24}$$

The previous equations aim to modify the frequency and amplitude reference values used in the second layer by correcting the error between the supplied powers, P and *Q*, and their references, P_{ref} and Q_{ref}, employing the controllers, $K_P(s)$ and $K_Q(s)$. Depending on the sign of these references, the power is supplied or consumed. However, when the microgrid works in island mode, the secondary control sets the references to the normalized voltage frequency and amplitude values.

The tertiary control can also be categorized depending on its architecture. In most cases, the tertiary approaches are based on centralized communication systems, as explained in the previous subsection. These types of systems depend on the MGCC to calculate the power set points, and the DGs do not deem the power supplied by the other elements. Furthermore, to avoid over-determining the system, one generator called the slack generator is not controlled and supplies the remaining power not contemplated in the control scheme.

On the other hand, the distributed and decentralized architectures do not require this slack generator since the DGs share information with each other allowing a more precise distribution of the power supplied.

3. Proposed AC microgrid hierarchical control

This section includes the main content of this thesis on developing an AC microgrid hierarchical control. First, the composition and requirements of the system studied are presented. Subsequently, the proposed control scheme is explained. Finally, the control loops of all the hierarchical control layers are analysed and tuned.

3.1. AC microgrid system description

The principal objective of the present thesis is to design a hierarchical control approach for an AC microgrid that unifies the second and third control so that the microgrid control scheme does not require to be modified regardless of the operating mode. Thus, a reference circuit can be implemented to study several control approaches.

The system under study consists of a laboratory triphasic AC microgrid that can operate in both grid-connected and island modes. The microgrid is formed by three branches connected to the PCC and contains three three-phase grid-forming generators distributed across the branches, as seen in Figure 17, two of them with a nominal power of 20 kVA and the remaining one of 40 kVA. It also includes two loads of 20 kVA and four contactors and considers the line impedances between elements.

The grid-forming generators consist of emulated batteries connected to the microgrid circuit through inverters. They are responsible for generating the phase voltage levels in the bus and supplying the power required by the loads when the microgrid is working in island mode or regulating the power injected when the microgrid is connected to the grid. On the other hand, the loads follow an RL circuit to consume both active and passive power.

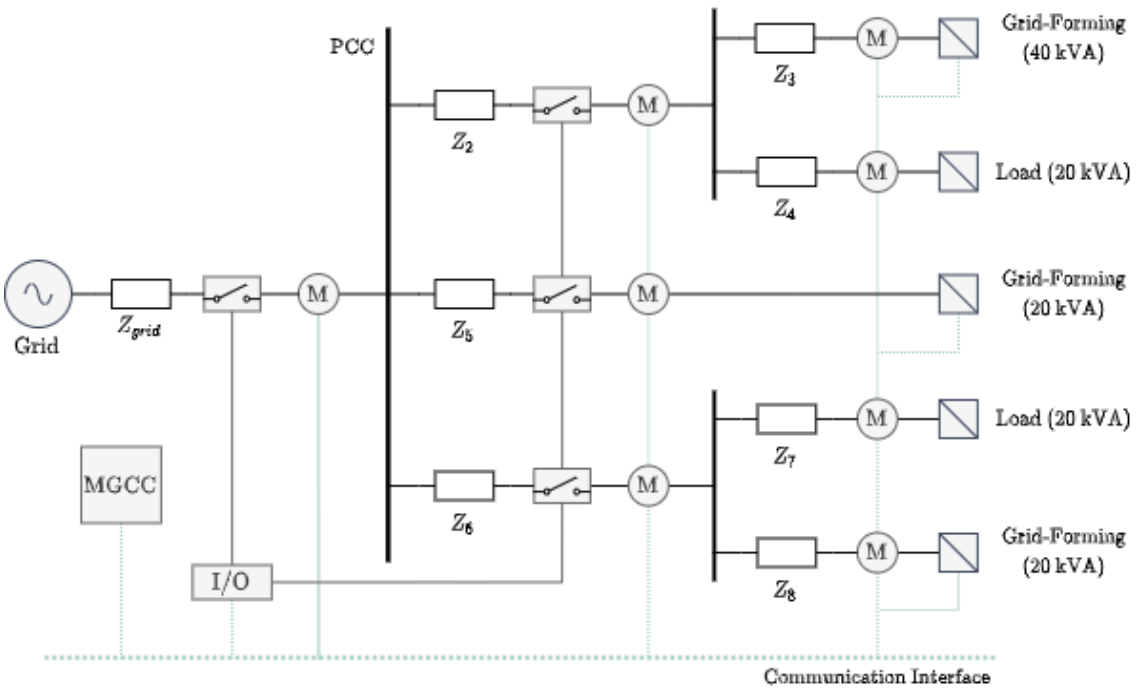

Figure 17 - Microgrid system

Besides the electrical bus, the microgrid is also constituted by a communication interface through which the elements communicate between themselves. Among the devices connected to the communication bus are the generators, the meters located at the point of coupling (PoC) of each generator and in each branch, the MGCC that includes the

microgrid control and the module of inputs and outputs responsible for controlling the contactors.

Figure 18 shows the structure of a DG. As can be observed, the electrical part is formed by the emulated battery that generates a DC voltage level which is later converted by the inverter to adapt it to the microgrid AC triphasic, and finally, the output is filtered by an LCL filter. Furthermore, a meter measures the voltage and the current of each phase to send the data via the communication interface afterwards.

In addition to the electrical part, the control algorithm is also displayed. Firstly, the active and reactive power, P_i and Q_i, is calculated from the local measurements of the voltage frequency and amplitude, ω_i and E_i, by means of a phase-locked loop (PLL). With this information, the droop control-based primary control distributes the power depending on the droop gains and creates the corresponding voltage reference followed by the inverters. Also, the embedded secondary and tertiary control proposed in this thesis computes its action, δ_i^{ω} and δ_i^{E}, accountable for the voltage frequency and amplitude restoration as well as the power flow by modifying the droop curve of the primary control.

It cannot be overlooked that the previously commented control also requires the information sent by the other generators and the MGCC. So, this data is received through the communication interface. It includes the active and reactive power supplied by neighbours Pj and Qj, the voltage frequency measured at their output, ωj, and the references and nominal powers of all the microgrids generators computed by the MGCC.

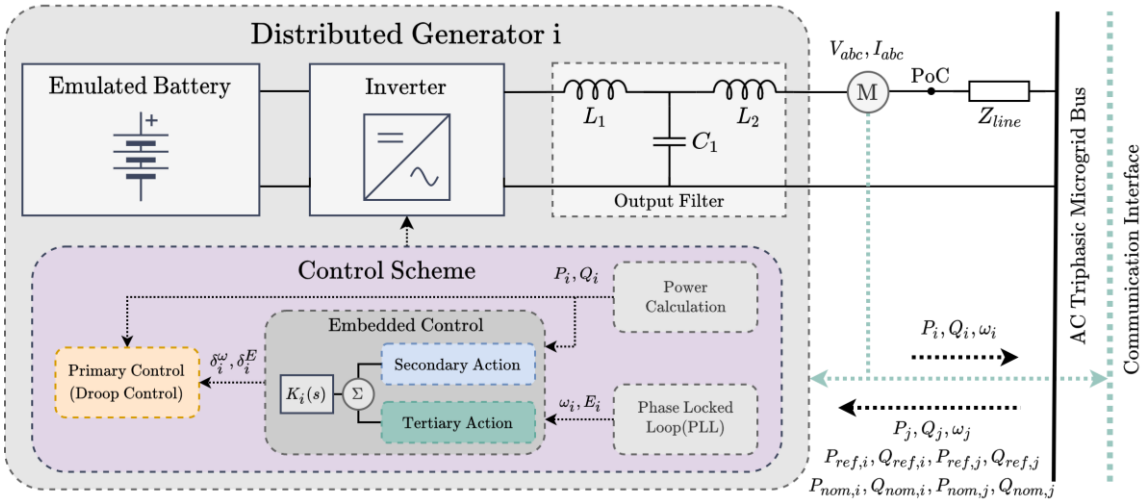

Figure 18 - Distributed Generator Structure

3.2. Proposed hierarchical control

This subsection aims to present the control law of the hierarchical control proposed in this thesis. From now, this control approach will be called *embedded control*. It consists of a microgrid distributed hierarchical structure that includes the second and the third layer in the same control law and intends to operate in grid-connected and island mode without being modified. This control is applied locally in each inverter, requiring that each neighbour and the MGCC transmit the necessary data. The distributed control actions from the embedded control are calculated as:

$$\delta_i{}^{\omega} = K_i{}^{\omega}(s)\left(\alpha\left(\omega_{ref} - \frac{1}{n}\sum_{j=1}^{n}\omega_j\right) - \beta\sum_{j=1\ j\neq i}^{n-1}\left(\frac{P_{ref,j}-P_j}{P_{nom,j}} - \frac{P_{ref,i}-P_i}{P_{nom,i}}\right)\right) \quad (3.1)$$

$$\delta_i{}^{E} = K_i{}^{E}(s)\left(\gamma\left(E_{ref} - E_i\right) - \varepsilon\sum_{j=1\ j\neq i}^{n-1}\left(\frac{Q_{ref,j}-Q_j}{Q_{nom,j}} - \frac{Q_{ref,i}-Q_i}{Q_{nom,i}}\right)\right) \quad (3.2)$$

The term corresponding to the active power secondary and tertiary control action is calculated as represented in the expression (3.1). It contemplates frequency restoration and the power distribution, with a single controller $K_i^{\omega}(s)$ as responsible. The first purpose is carried out by eliminating the deviation of frequency from a reference, ω_{ref}. To calculate this difference, the average of the frequencies read at the output of each inverter is computed. On the other hand, the active power flow control is accomplished by removing the disparity between the deviation of the actual active power supplied by converter i, P_i, from its reference, $P_{i\,ref}$, and the same deviation for the active power supplied by neighbour generators or grid, P_j. Each deviation is proportional to its nominal active power value, P_{nom}, to adjust the magnitude of the values.

Despite integrating the two layers in the same control approach, each one must have a different dynamic. Thus, the α and β constants modify the gain of the controller and, consequently, determine the dynamics of each control.

As a counterpart, the expression (3.2) considers the action of the reactive power secondary and tertiary control. The control law is equivalent to the previous one, but, in this instance, the focus is on the voltage amplitude correction and the reactive power flow. The two terms, γ and ε, weigh the controller's action.

Figure 19 displays the equations (3.1) and (3.2) more graphically.

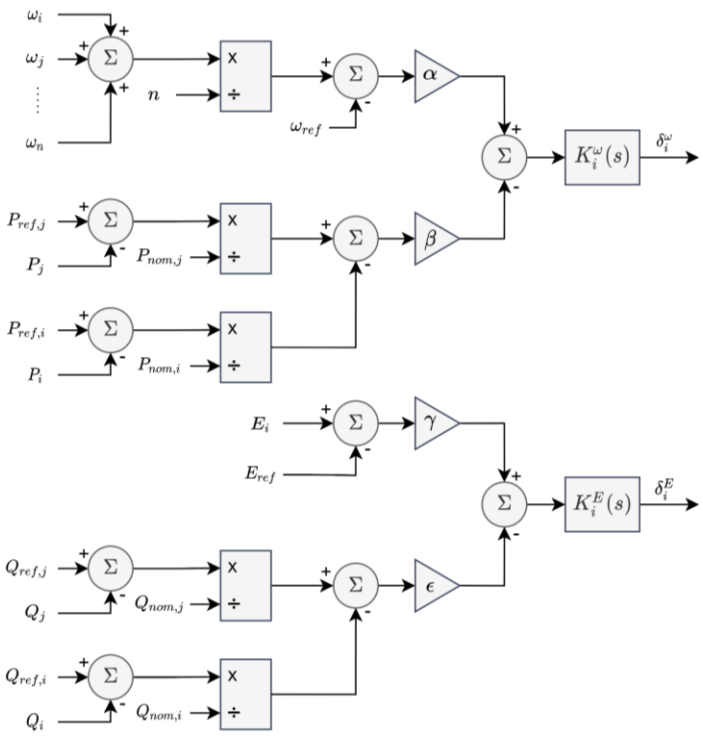

Figure 19 - Embedded control block diagram

3.3. Hierarchical control design

Once the system and the proposed control approach have been presented, the next step is to tune the control loops of each layer of the hierarchy so that the control has the desired dynamics. For this, the first stage of this subsection has been to obtain the block diagram of the control system's active and reactive power loops and explain them. The following steps have been to analyse the primary, secondary and tertiary control separately and for a single generator. In this process, several issues regarding the union of all hierarchical layers are addressed.

3.3.1. Hierarchical control

a. The active power control loop

Figure 20 shows the block diagram of the active power control loop. It consists of a multiple-input single-output (MISO) system which contemplates the three layers of the hierarchical control besides considering the embedded control.

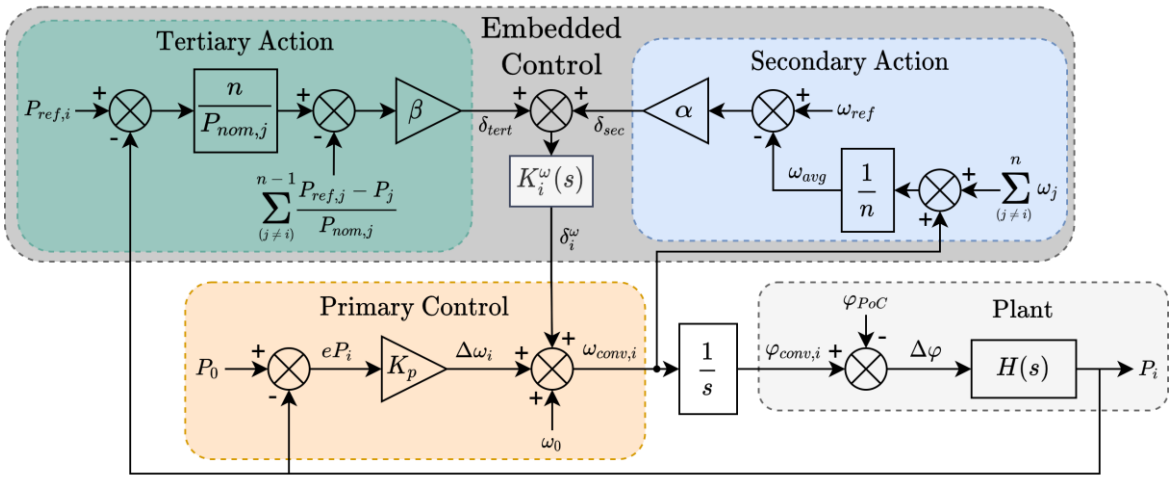

Figure 20 – Hierarchical control active power control loop block diagram

As seen in the scheme, the primary control feedbacks the system output, which is the actual supplied active power, P_i, to subtract it from the active power set point, P_0. From the difference, the frequency deviation, $\Delta\omega_i$, is calculated using the active droop gain, Kp, following the equation (2.8) of the previously presented droop control. The result is added to the nominal frequency, ω_0, in addition to the embedded control term, δ_i^{ω}, to obtain the converter frequency, $\omega_{conv,i}$.

Concerning the embedded control, the block diagram considers both actions, the secondary and tertiary control. On the one hand, the secondary control calculates the average of all the generator frequencies, including its one, and computes the deviation from the frequency reference, ω_{ref}, to eliminate it. Finally, this difference is multiplied by the factor α. On the other hand, the tertiary control feeds back again the active power supplied, already used in the primary control, and it is subtracted from the reference sent by the MGCC, $P_{ref,I}$. The outcome is multiplied by the number of neighbours, n, and the inverse of the nominal power. The last step is to compute the subtraction of the differences calculated in each neighbour and multiply it by the factor β. The action of both controls, secondary and tertiary, is lastly combined, and the term δ_i^{ω} is calculated by the integral controller $K_i^{\omega}(s)$ to correct the frequency deviation and follow the active power reference.

The converter frequency is integrated to obtain the corresponding phase, $\varphi_{conv,i}$, and the phase variation from the PoC is deemed the plant's input. The plant characterises the power flow in a line between a three-phase distributed generator char and its PoC when an ideal triphasic AC power system with a constant voltage and frequency is connected, as shown in Figure 21. That is, in the case that the microgrid works in grid-connected mode. The power line consists of the output inductor, L_2, of the LCL filter, and it is modelized by an inductor, L, and a resistor, R_L.

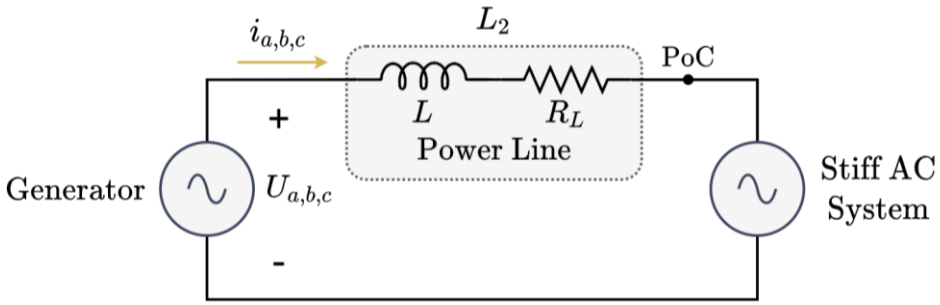

Figure 21 - Three-phase generator connected to an infinite AC system through a power line

Given that, the plant's transfer function relating phase to active power is expressed in the equation (3.3). Its development has been carried out employing the dynamic phasor models following [19].

$$H(s) = \frac{P}{\varphi} = \frac{3U_c^2\omega_0 L}{L^2s^2 + 2R_L Ls + (\omega_0 L)^2 + R_L^2} \tag{3.3}$$

The result is a second-order transfer function that considers the active power flow and the constant voltage, U_c, and frequency, ω_0, of a stiff AC system.

b. The reactive power control loop

In the case of the reactive power control loop, the system remains following the MISO structure and again contemplates the primary, secondary and tertiary controls and the embedded approach, as shown in Figure 22.

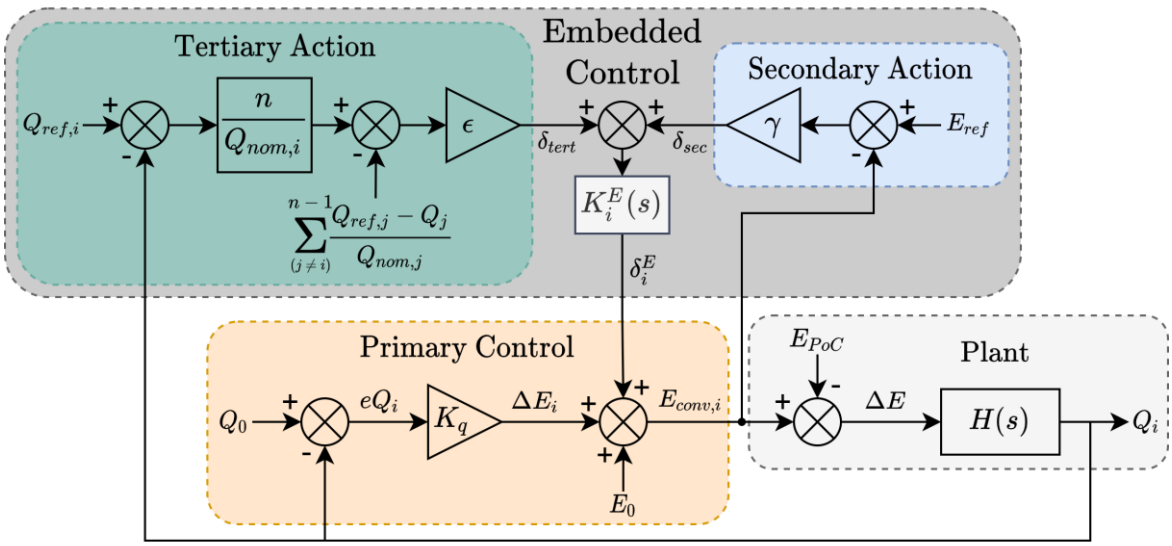

Figure 22 - Hierarchical control reactive power loop block diagram

The reactive primary control block diagram follows the droop equation (2.9), similarly to the active power control loop. The droop constant, K_q, relates the reactive power supplied and its set point to compute the corresponding voltage amplitude deviation, ΔE_i. The embedded control also follows the same structure as the active power control loop except for the secondary action, which does not compute the average of all the amplitude voltages and only considers the local amplitude measured at its PoC to correct the deviation from the reference, E_{ref}.

Finally, the action of the primary and the embedded control are accumulated with the nominal amplitude, E_0, to obtain the converter amplitude, $E_{conv,i}$. The difference in this amplitude from the one at PoC is the plant's input, shown in Figure 21. The transfer function must now relate the voltage amplitude and the reactive power resulting in the expression (3.4), obtained using the dynamic phasor models [19].

$$H(s) = \frac{Q}{E} = \frac{3U_c\omega_0 L}{L^2s^2 + 2R_L Ls + (\omega_0 L)^2 + R_L^2} \tag{3.4}$$

3.3.2. Primary control

From this subsection onwards, the analysis of the control layers shall be made separately, given the complexity of the system loops presented in the previous subsection. The first simplification has been to assume a single converter to analyse the layer's control loops to avoid the coupling between generators and reduce the number of system inputs. Moreover, the coupling between active and reactive power loops is also not deemed.

On the other hand, it is desired that the dynamics of the primary control follow a first-order response as fast as possible. For this, each loop's only degree of freedom is the droop constant, which will be tuned considering the system stability, the maximum frequency or amplitude deviation allowed, and finally, the desired dynamics.

The required variable values are shown in Table 1.

Table 1 - Grid and LCL filter parameters

Magnitude	Value
Nominal voltage (U_c)	230 V P-N
Nominal frequency (ω_0)	2π50 rad/s
LCL filter output inductor (L)	548 μF
LCL filter output resistor (R_L)	37 mΩ

a. Active power control loop

The objective of this part is to obtain an active power droop gain, K_p, with which the system is stable and meets the requirements previously mentioned. For that purpose, the block diagram of Figure 20 has been simplified by considering the embedded control action as input and just considering the primary control action and the plant. The outcome is the block diagram shown in Figure 23.

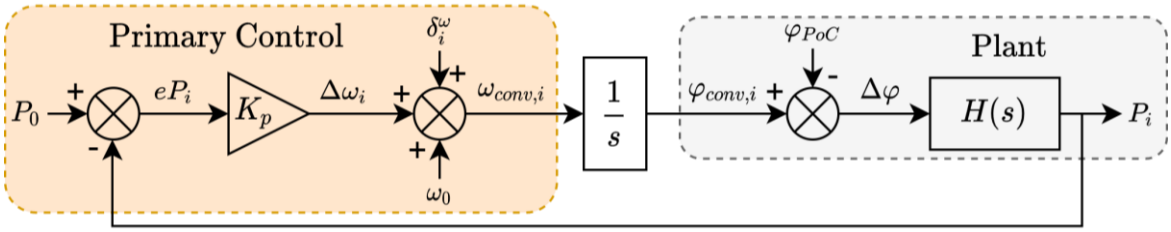

Figure 23 - Primary active power control loop block diagram

As can be seen, the system is formed by the droop constant, an integrator and the plant which follows the transfer function of the expression (3.3). Furthermore, the embedded control action, the nominal frequency, and the phase at the PoC are considered perturbations and have been neglected to turn the system into a single-input single-output (SISO) system. Knowing that, the system's open-loop and closed-loop transfer functions are represented in the expressions (3.5) and (3.6), respectively. Observing these transfer functions, the system contains three poles since it is a third-order system and shows that it does not present steady-state error in response to a step input since the open-loop expression contains a pure integrator.

$$G_{OL}(s) = \frac{3{U_c}^2 \omega_0 L K_p}{L^2 s^3 + 2R_L L s^2 + ((\omega_0 L)^2 + R_L^2)s} \tag{3.5}$$

$$G_{CL}(s) = \frac{3{U_c}^2 \omega_0 L K_p}{L^2 s^3 + 2R_L L s^2 + ((\omega_0 L)^2 + R_L^2)s + 3{U_c}^2 \omega_0 L K_p} \tag{3.6}$$

Once the transfer functions of the active power control loop have been obtained, the tuning of the droop gain can be performed. First, the K_p limits are obtained by employing stability analysis and studying the maximum frequency deviation allowed by regulations. Then, a droop constant is selected to meet the dynamic requirement.

1. Stability analysis

A root locus analysis has been accomplished to examine how the poles of the system change with variation of the droop gain. For this analysis, the system open-loop transfer function (3.5) with the variables of Table 1 substituted is required.

$$G_{OL}(s) = \frac{27.32 \cdot 10^3 \cdot K_p}{300.3 \cdot 10^{-6} s^3 + 40.55 \cdot 10^{-6} s^2 + 31 \cdot 10^{-3} s} \tag{3.7}$$

Considering the expression (3.7) and the root locus gain as K_p, the result is displayed in Figure 24. The graph shows the evolution of the three poles of the system, one real and two complex conjugates; as the droop gain increases indicates that there is a droop gain limit by which the system is unstable since the complex conjugated poles become in the right half-plane.

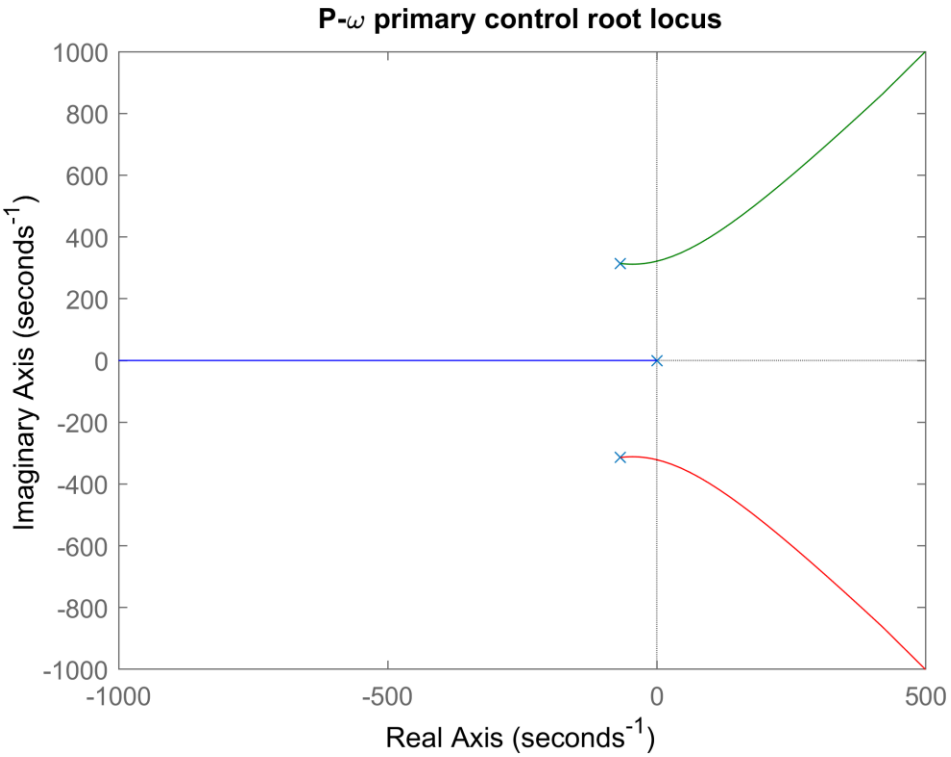

Figure 24 - Active power control loop root locus analysis

Therefore, the maximum value of droop gain considering stability must be obtained. For this purpose, the denominator of the closed-loop transfer function *D(s)* is studied in its isochronous form $D(j\omega_0)$ represented in the expressions (3.8) and (3.9), respectively.

$$D(s) = L^2 s^3 + 2R_L L s^2 + ((\omega_0 L)^2 + R_L^2)s + 3{U_c}^2 \omega_0 L K_p \tag{3.8}$$

$$D(j\omega) = j^3 L^2 \omega^3 + j^2 2R_L L \omega^2 + j((\omega_0 L)^2 + R_L^2)\omega + 3{U_c}^2 \omega_0 L K_p \tag{3.9}$$

The denominator in the Laplace domain becomes the isochronous form by substituting *s* with $j\omega$. To obtain the maximum K_p, first, the equation is arranged by substituting the variables and replacing the independent term with *K,* as shown in (3.10).

$$D(j\omega) = -j\,300 \cdot 10^{-9}\omega^3 - 40.48 \cdot 10^{-6}\omega^2 + j\,31 \cdot 10^{-3}\omega + K_{limit} \tag{3.10}$$

If the real and imaginary parts of the equation (3.10) are separated and equal to 0, then a system of two equations with two unknowns, K_{limit}, and ω, is formed.

$$Re\big(D(j\omega)\big) = K_{limit} - 40.48 \cdot 10^{-6}\omega^2 = 0 \tag{3.11}$$

$$Im\big(D(j\omega)\big) = 31 \cdot 10^{-3}\omega - 300 \cdot 10^{-9}\omega^3 = 0 \tag{3.12}$$

Solving the equation system formed by (3.11) and (3.12), a $K_{limit,}$ which makes the system critically stable, is obtained. Finally, by matching this K_{limit} to the independent term of the characteristic equation (3.8), the maximum droop gain can be calculated as seen in the equation (3.13).

$$K_{limit} = 3U_c \omega L K_{p\_max} \tag{3.13}$$

If the already known variables (Table 1) are replaced from the equation (3.13), the maximum droop gain considering the stability is obtained and shown below.

$$K_{p\_\max\_stability} = 153.25 \cdot 10^{-6} \frac{rad/s}{W}$$

2. Maximum deviation limit

On the other hand, the droop gain is also limited by the maximum frequency deviation that can occur in the whole microgrid. According to IEC 61727, the maximum deviation is 2%, which in the case of a nominal frequency of 50Hz means a maximum deviation of 1 Hz or 2π rad/s. Since K_p relates active power to frequency, the upper limit values in island mode would also depend on the generator rated active power, as shown in Figure 25.

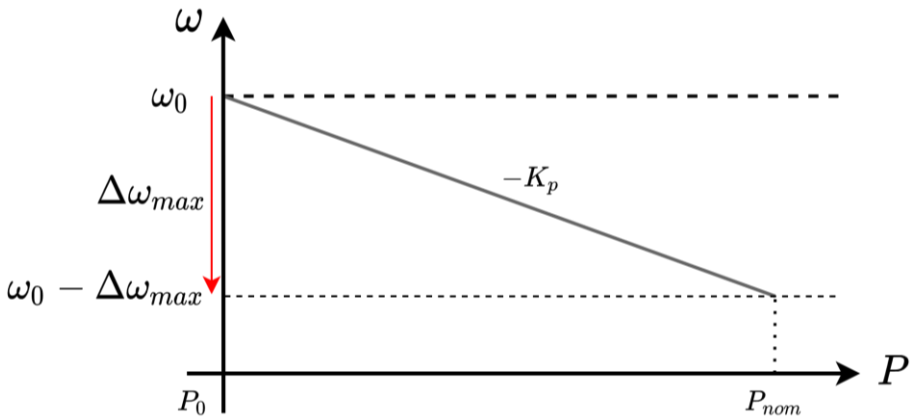

Figure 25 - P-ω droop curve limits

Considering this, the maximum droop gain is obtained by relating the maximum deviation with the nominal power,

$$K_{p\_max} = \frac{\Delta\omega_{max}}{P_{nom}} \tag{3.14}$$

Thus, the droop gain limit for a generator that has a nominal power of 20 kVA would be:

$$K_{p\_max,20} = \frac{2\pi\, rad/s}{20\ kW} = 314.16 \cdot 10^{-6} \frac{rad/s}{W}$$

While for a generator of 40 kVA would be:

$$K_{p\_\max,40} = \frac{2\pi\, rad/s}{40\ kW} = 157.08 \cdot 10^{-6} \frac{rad/s}{W}$$

Both limits are greater than the one that considers the system stability, so the limit obtained in the previous subsection is the most restrictive one. In this way, in the case of a generator with a nominal power of 20 kVA, the maximum frequency deviation would be 0.49 Hz or 3.06 rad/s. In contrast, the generator with a nominal power of 40kVA have a gain that covers a greater frequency deviation close to the maximum one, particularly 0.97 Hz or 6.13 rad/s.

3. Dynamics

Once the active droop gain limit has been established, the next step is to obtain the K_p with which the system has a first-order behaviour and is as fast as possible. For this purpose, the first step has been to plot the system's poles depending on the droop gain observed in the pole-zero map shown in Figure 26. The droop gain sweep extends to the stability limit to demonstrate that the limit has been correctly calculated.

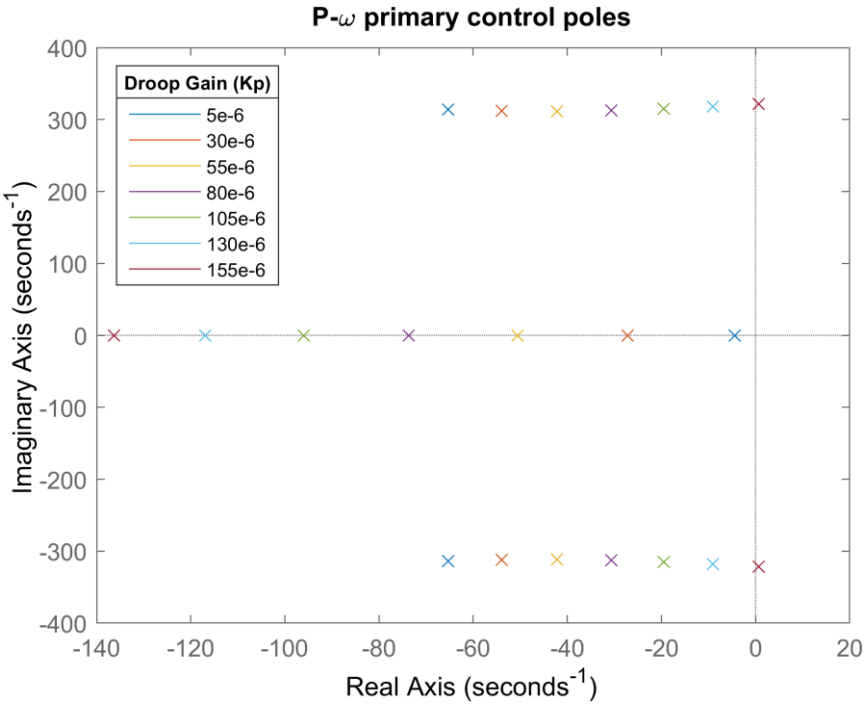

Figure 26 - Poles of the system, depending on the active power droop gain

The complex poles approach the imaginary axis, and the real one gets away from it as the gain increases following the evolution seen in Figure 24. Consequently, the droop gains that meet the response requirement are the smallest ones since the real pole tends to be dominant.

After the pole-zero map has been studied, the droop gain should be selected according to the required behaviour. In consequence, the dominance of the real pole must be applied. To make these calculations, the denominator of the closed-loop transfer function (3.8) is expressed depending on the poles in (3.15) and reorganized in (3.16). Being *A* the real pole, *B* the real part of the conjugated poles and *C* the imaginary part.

$$L^2 s^3 + 2R_L L s^2 + ((\omega_0 L)^2 + R_L^2)s + 3{U_c}^2 \omega_0 L K_p = (\mathrm{s} + \mathrm{A})(\mathrm{s} + (\mathrm{B} + \mathrm{jC}))(\mathrm{s} + (\mathrm{B} - \mathrm{jC})) \quad (3.15)$$

$$s^3 + \frac{2R_L}{L}s^2 + \frac{(\omega_0 L)^2 + R_L^2}{L^2}s + \frac{3{U_c}^2 \omega_0 L K_p}{L} = s^3 + (A + 2B)s^2 + (2AB + B^2 + C^2)s + A(B^2 + C^2) \quad (3.16)$$

Since the real pole must be dominant, A is fixed to be ten times lower than *B* fulfilling the relation (3.17).

$$B = 10A \quad (3.17)$$

Finally, an equation system is obtained relating the coefficient corresponding to s^2, s and the independent term (3.16) and assuming the relation (3.17). The results of the system are:

$$p_1 = -6.43$$

$$p_{2,3} = -64.3 \pm j313.5$$

$$K_p = 7.24 \cdot 10^{-6} \frac{rad/s}{W}$$

Figure 27 shows the unitary step response of the system with the calculated active power droop gain in addition to the responses with the values around the obtained one. As can be seen, the response follows a first-order behaviour and has a time constant of around 0.155 seconds and a settling time of 1 second, which is fast enough, also calculated by inverting the real pole calculated.

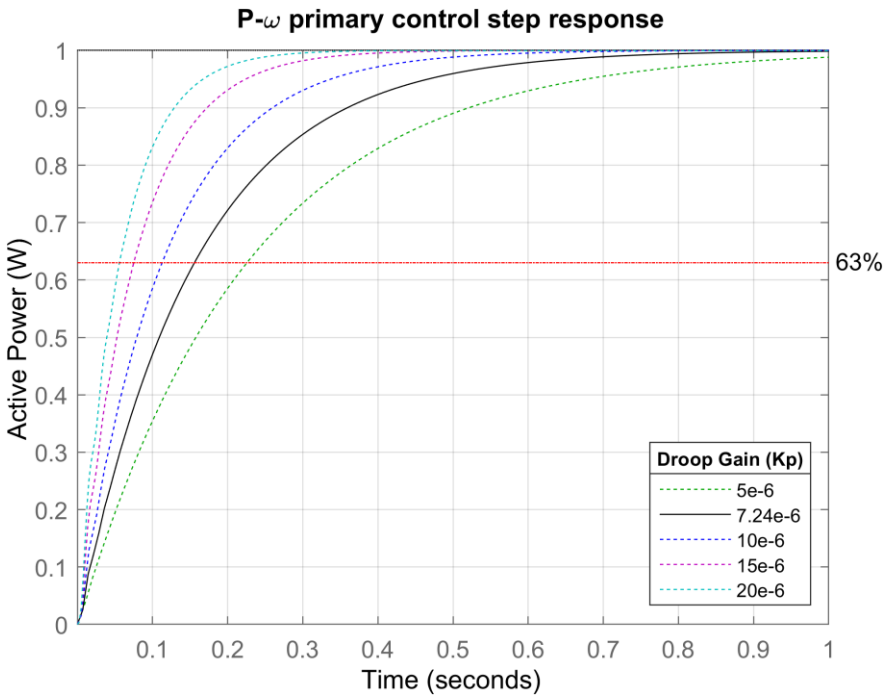

Figure 27 - Step response of the system depending on the active power droop gain

If the droop gain is applied, the maximum frequency deviation for a generator with 20 kVA of nominal power is 0.023 Hz. However, a generator with a nominal power of 40 kVA contemplates a maximum deviation of 0.046 Hz. Since the frequency is a global variable, the DG with higher nominal power is limited by the maximum deviations set by the lower nominal power generator. Due to this fact, the droop gain of the generator of 40 kVA must be half the value of the 20 kVA one to use its full power range at the expense of slowing down the control to a time constant of around 0.312 seconds. Figure 28 shows the conflict previously commented.

As a conclusion of this subsection, the active power droop gains selected are as follows:

$$K_{p,20} = 7.24 \cdot 10^{-6} \frac{rad/s}{W}$$

$$K_{p,40} = 3.62 \cdot 10^{-6} \frac{rad/s}{W}$$

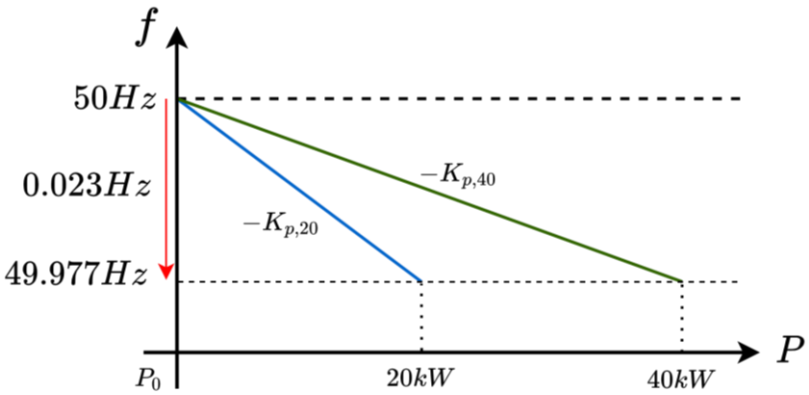

Figure 28 - P-ω droop curves for a 20kVA and 40kVA generators

b. The reactive power control loop

As has been done with the active power control loop, the objective of this subsection is to calculate the reactive power droop gain, K_q. Again, the droop constant selected must meet the requirement of the system consisting of a first-order behaviour with a response as fast as possible. The block diagram required to analyse the control loop is shown in Figure 29, and it has been obtained by simplifying the Figure 22 diagram by considering the reactive power setpoint, Q_0, as the input.

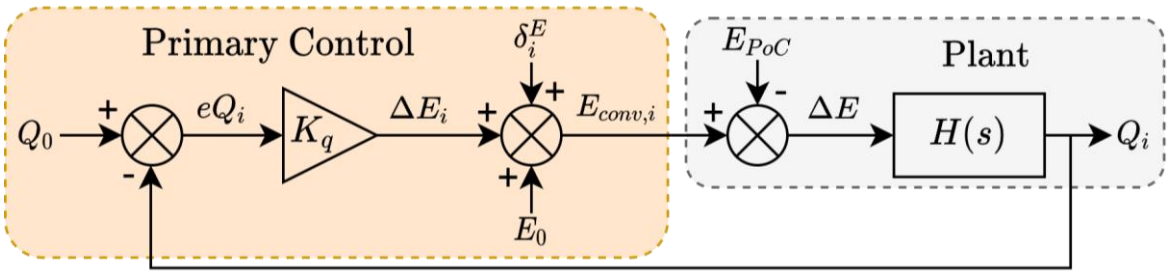

Figure 29 - Primary reactive power control loop block diagram

The system is just formed by the droop gain and the plant, which follows the transfer function of the expression (3.4). Once more, the embedded control action has been deemed an input and neglected since its dynamics are slower than the primary control one. The amplitude at the PoC and the nominal voltage are also assumed perturbations and neglected to simplify the analysis. This way, the system becomes a SISO system with an open-loop and closed-loop transfer functions shown in (3.18) and (3.19), respectively.

$$G_{OL}(s) = \frac{3U_c\omega_0 LK_q}{L^2s^2 + 2R_L Ls^2 + (\omega_0 L)^2 + R_L^2} \tag{3.18}$$

$$G_{CL}(s) = \frac{3U_c\omega_0 LK_q}{L^2s^2 + 2R_L Ls + (\omega_0 L)^2 + R_L^2 + 3U_c\omega_0 LK_q} \tag{3.19}$$

In contrast to the active power control loop, the system follows a second-order form so contains two poles and presents steady-state error in response to a step input since the system is type 0.

Before focusing on the system's stability and behaviour, a root locus analysis has been carried out to evaluate the two poles in terms of K_q. The transfer function studied (3.20) is obtained from the open-loop expression (3.18), considering K_q as the root locus gain and substituting the values of Table 1.

$$G_{OL}(s) = \frac{118.8 \cdot Kq}{300.3 \cdot 10^{-6}s^3 + 40.55 \cdot 10^{-6}s^2 + 31 \cdot 10^{-3}s} \tag{3.20}$$

The root locus analysis shows two conjugated poles, as seen in Figure 30. It can be concluded that the system follows a second-order dynamics independently of the droop control gain, but it does not present stability problems. Because of that, the system has been modified to meet the requirements.

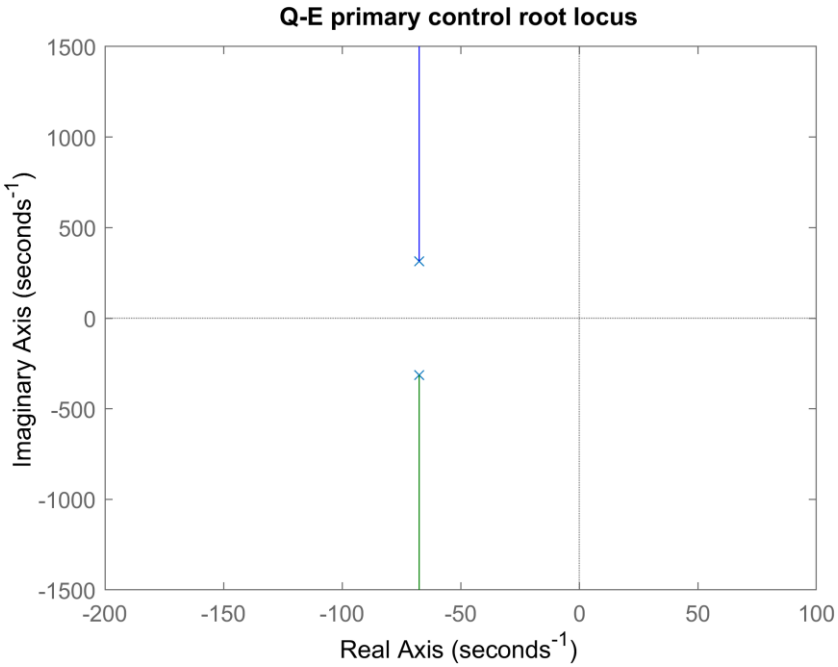

Figure 30 - Reactive power control loop root locus analysis

The proposed new control adds a low pass filter (LPF) to the system presented in Figure 29 to modify the system dynamics to obtain a response without oscillations or overshoot (first-order response). The LPF transfer function in terms of the cut-off frequency, ω_c, is expressed in (3.21).

$$LPF(s) = \frac{1}{\frac{s}{\omega_c} + 1} \tag{3.21}$$

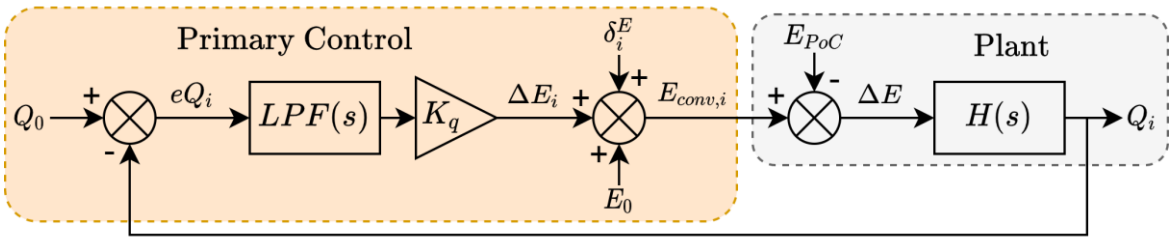

Figure 31 - Primary reactive power control loop with LPF block diagram

Now, the new block diagram consists of the reactive power droop gain, the plant and a LPF as shown in Figure 31. Its open-loop and closed-loop transfer functions are expressed in (3.22) and (3.23).

$$G_{OL}(s) = \frac{3U_c\omega_0 L K_q \omega_c}{L^2 s^3 + (2R_L L + \omega_c L^2)s^2 + (\omega_0{}^2 L^2 + 2\omega_c R_L L + R_L^2)s + \omega_c \omega_0{}^2 L^2 + \omega_c R_L^2} \tag{3.22}$$

$$G_{CL}(s) = \frac{3U_c\omega_0 L K_q \omega_c}{L^2 s^3 + (2R_L L + \omega_c L^2)s^2 + (\omega_0{}^2 L^2 + 2\omega_c R_L L + R_L^2)s + \omega_c \omega_0{}^2 L^2 + \omega_c R_L^2 + 3U_c\omega_0 L K_q \omega_c} \tag{3.23}$$

The open-loop expression does not contain any pure integrator, so the final system still has a steady-state error. However, the system is now of third order, meaning that it has an additional pole. To verify that the system can have a first-order response, a root locus analysis is performed from the expression (3.24), obtained by substituting the variables of Table 1 of the open-loop transfer function (3.23) and considering K_q as the root locus gain in addition to using a unitary cut-off frequency ω_c as reference.

$$G_{OL}(s) = \frac{118.8}{300.3 \cdot 10^{-6} s^3 + 40.08 \cdot 10^{-5} s^2 + 31.05 \cdot 10^{-3} s + 31.01 \cdot 10^{-3}} \tag{3.24}$$

In contrast to the first system (Figure 30), the root locus analysis shows a real extra pole in addition to two conjugated poles, as seen in Figure 32. Consequently, the system can have a first-order response by forcing the real pole to be dominant. Besides, the system has a limit for which the system is unstable.

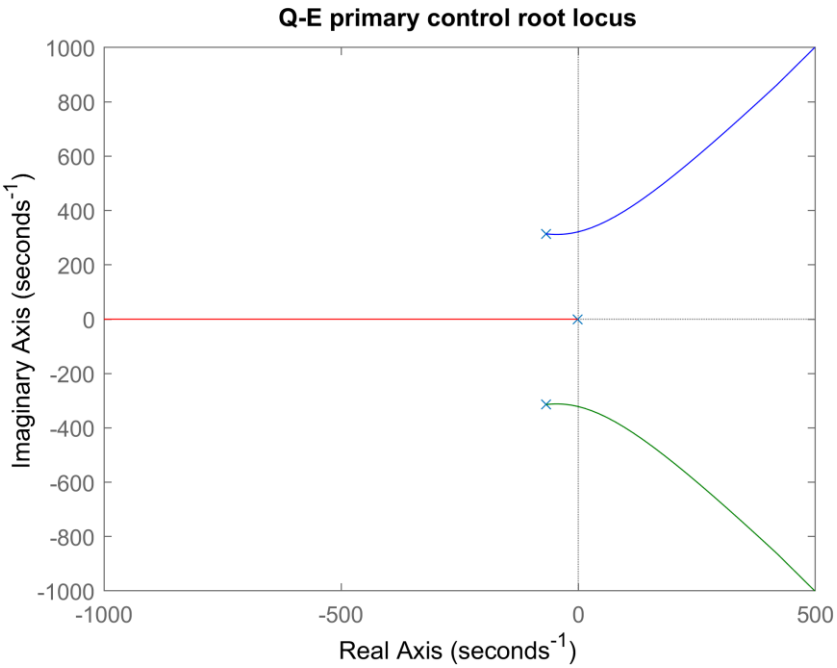

Figure 32 - Reactive power control loop with LPF root locus analysis

Once the transfer functions are obtained and a first-order response can be ensured, the droop gain tuning can be performed. Due to the new degree of freedom, ω_c, added by the LPF, the droop gain has been obtained only considering the maximum voltage amplitude deviation and the steady-state error. Then, the cut-off frequency is calculated by studying the system's stability and dynamics.

1. Maximum deviation limit

According to IEC 61727, the maximum voltage deviation is 3% which in the case of a nominal voltage amplitude of 325 V means a maximum deviation of 9.75 V. Since K_q relates reactive power to voltage amplitude, then the upper limit values in island mode would depend on the generator rated reactive power as shown in Figure 33.

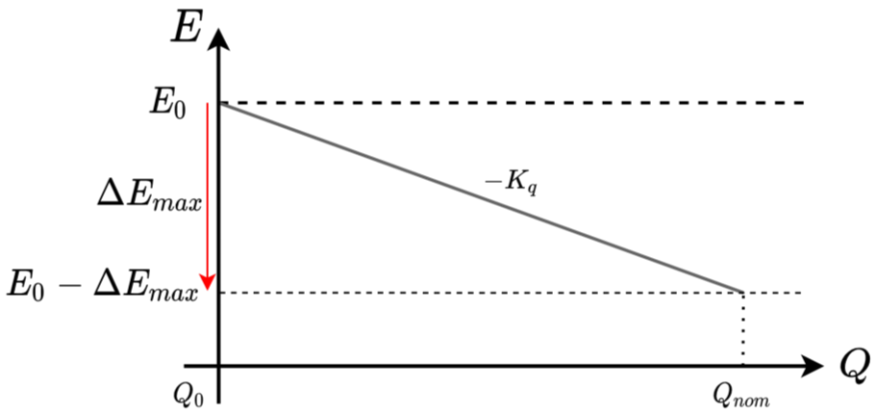

Figure 33 - Q-E droop curve limits

Considering this, the maximum droop gain is obtained by relating the maximum deviation with the nominal power as expressed in (3.25).

$$K_{q\_max} = \frac{\Delta E_{max}}{Q_{nom}} \tag{3.25}$$

The regulation IEEE Std. 1547-201 declares that equipment can supply a maximum reactive power equal to 0.44% of the nominal power. Thus, in the case of a generator that has a nominal power of 20 kVA, the droop gain limit would be:

$$K_{q\_\max,20} = \frac{9.75\ V}{0.44 \cdot 20\ kvar} = 1.107 \cdot 10^{-3}\,\frac{V}{var}$$

While for a generator of 40 kVA would be:

$$K_{q\_\max,40} = \frac{9.75\ V}{0.44 \cdot 40\ kvar} = 553.9 \cdot 10^{-6}\,\frac{V}{var}$$

2. Steady-state error

Another point of interest in tuning the reactive power control loop is the steady-state error (SSE) with respect to a step response. The relation between the permanent error, the system variables and the droop gain is expressed in (3.26). As observed, the error is independent of the LPF cut-off frequency.

$$SSE = \frac{{\omega_0}^2 L^2 + R_L^2}{3U_c\omega_0 L K_q + {\omega_0}^2 L^2 + R_L^2} \tag{3.26}$$

A droop gain sweep between 0 and the droop gain limit for a 20kVA generator with the variables of Table 1 substituted is performed. It is shown in Figure 34 that the greater the reactive power droop gain, the lower the permanent error.

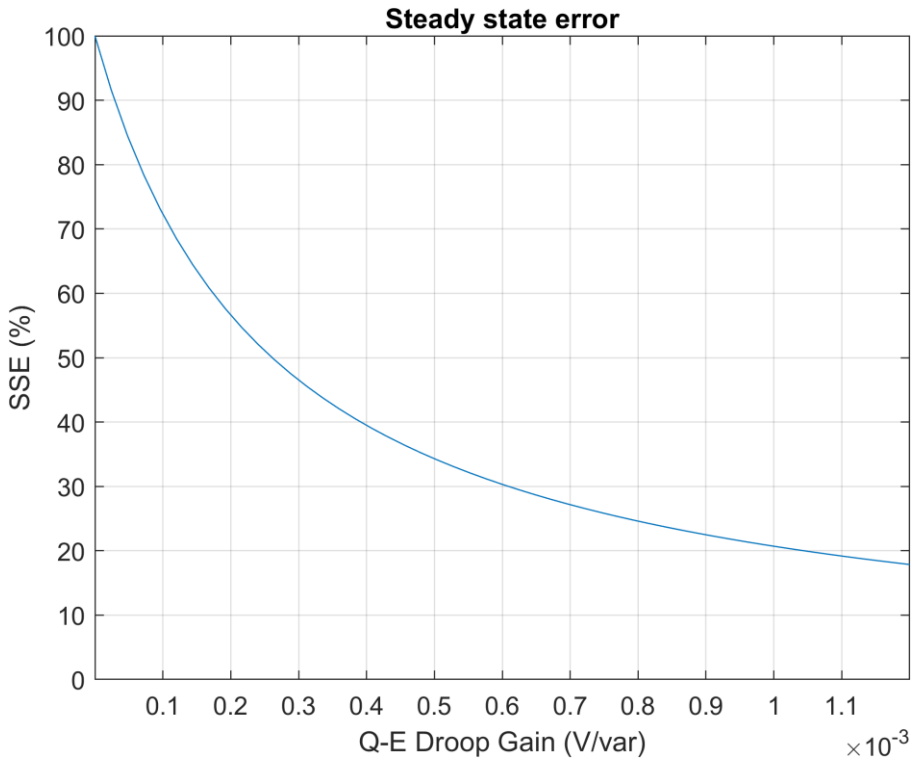

Figure 34 - Steady-state error depending on reactive power droop gain

Finally, a droop gain can be set considering the limit concerning amplitude deviation and the relation between SSE and K_q. A value with a good compromise between the voltage quality in island mode and SSE for a generator with 20 kVA would be,

$$K_{q,20} = 800 \cdot 10^{-6} \frac{V}{var}$$

which contemplates a permanent error of 24.6% and a maximum deviation of 7.04V.

As in the active power case, the generator with higher nominal power is limited by the maximum deviations set by the lower nominal power generator. Due to this fact, the droop gain of the generator of 40 kVA must be half the value of the 20 kVA one to use its full power range at the expense of slowing down the response and worsening the permanent error. Figure 35 shows the conflict previously commented. In conclusion, the droop gain of a generator with 40 kVA is:

$$K_{q,40} = 400 \cdot 10^{-6} \frac{V}{var}$$

which contemplates an SSE of around 40%.

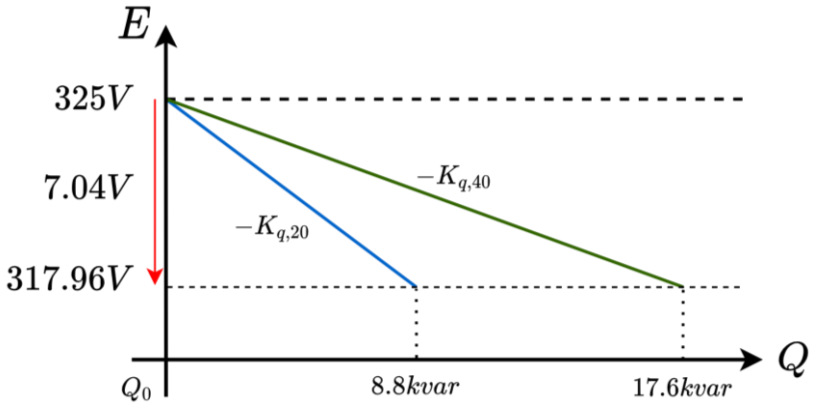

Figure 35 - Q-E droop curves for an 8.8 kvar and 17.6 kvar generators

3. Stability analysis

Once the droop gain has been set, the next step taken is to obtain the maximum cut-off frequency with which the system is deemed stable. For this purpose, the isochronous form (3.28) of the denominator (3.27) of the closed-loop transfer function (3.23) is obtained and analysed.

$$D(s) = L^2 s^3 + (2R_L L + \omega_c L^2)s^2 + ({\omega_0}^2 L^2 + 2\omega_c R_L L + R_L^2)s + \omega_c {\omega_0}^2 L^2 + \omega_c R_L^2 + 3U_c \omega_0 L K_q \omega_c \quad (3.27)$$

$$D(j\omega) = j^3 L^2 \omega^3 + j^2(2R_L L + \omega_c L^2)\omega^2 + j({\omega_0}^2 L^2 + 2\omega_c R_L L + R_L^2)\omega + \omega_c {\omega_0}^2 L^2 + \omega_c R_L^2 + 3U_c \omega_0 L K_q \omega_c \quad (3.28)$$

From the isochronous form, the cut-off frequency limit can be calculated by following the same procedure used for the active power control loop. For this purpose, the isochronous form is arranged, its variables are substituted by the values of Table 1 and the droop gain of a generator with a nominal power of 20kVA since it is the fastest option. Additionally, the independent term is replaced by K, as shown in (3.29).

$$D(j\omega) = -j\,300 \cdot 10^{-9}\omega^3 - (300 \cdot 10^{-9}\omega_c + 40.6 \cdot 10^{-6})\omega^2 + j\,(40.6 \cdot 10^{-6}\omega_c + 31 \cdot 10^{-3})\omega + K \quad (3.29)$$

If the real and imaginary parts of the equation (3.29) are separated and equal to 0, a system of two equations is formed.

$$Re\big(D(j\omega)\big) = K_{limit} - (300 \cdot 10^{-9}\omega_c + 40.6 \cdot 10^{-6})\omega^2 = 0 \quad (3.30)$$

$$Im\big(D(j\omega)\big) = (40.6 \cdot 10^{-6}\omega_c + 31 \cdot 10^{-3})\omega - 300 \cdot 10^{-9}\omega^3 = 0 \quad (3.31)$$

Solving the equation system, a K_{limit} which makes the system critically stable, is obtained. In this case, the outcome depends on ω_c, which is the desired variable. To bring it, this K_{limit} is matched with the independent term that also depends on ω_c to obtain the relation (3.32).

$$K_{limit} = \omega_{c\_max}({\omega_0}^2 L^2 + R_L^2 + 3U_c \omega_0 L K_q) \quad (3.32)$$

If the already known variables (Table 1) are replaced from the equation (3.32), the maximum cut-off frequency considering the stability of the system is obtained and shown in (3.33).

$$\omega_{c\_\max} = 47.79\,{}^{rad}/_{s} \tag{3.33}$$

4. Dynamics

The last step of the reactive power control loop tuning is to obtain the cut-off frequency with which the system has a first-order response as fast as possible. Again, the pole-zero map depending on the required variable has been plotted with a sweep that extends to the stability limit to verify the calculated value.

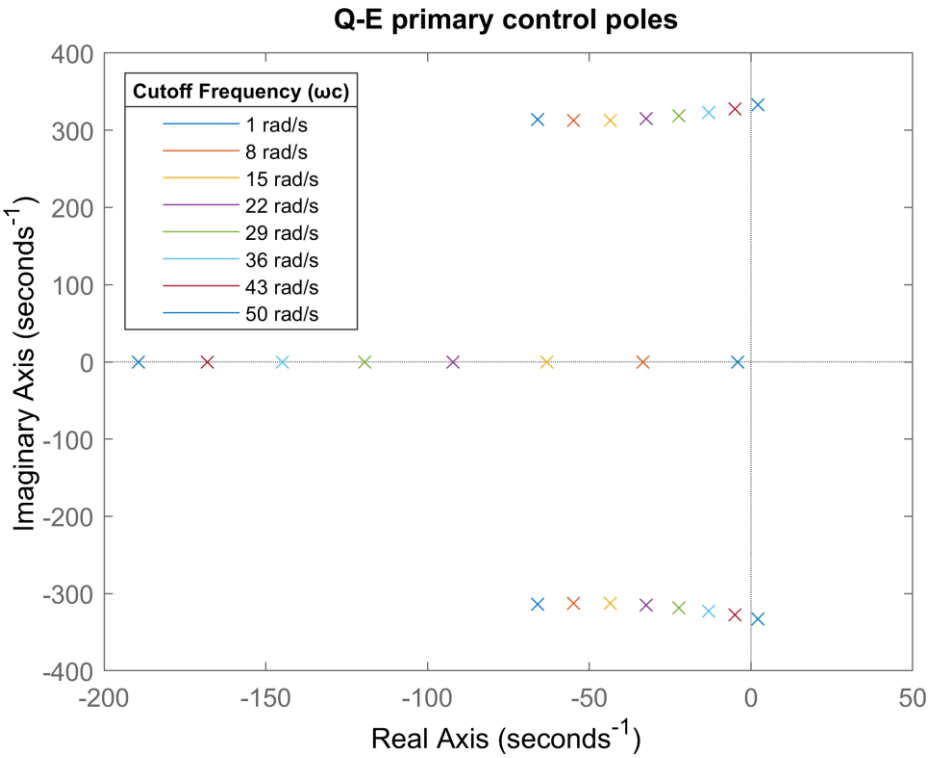

Figure 36 - Poles of the system depending on the LPF cut-off frequency

Figure 36 shows the evolution of the three poles. The complex zeros approach the imaginary axis, and the real one gets away from it as the cut-off frequency increases. Therefore, the cut-off frequency that meets the response requirements is again the smallest one which ensures the dominance of the real pole. The calculation performed to obtain the required value consists in expressing the denominator of the closed-loop transfer function (3.27) depending on the poles, as seen in (3.34).

$$\begin{aligned} s^3 + \frac{\omega_c L^2 + 2R_L}{L}s^2 + \frac{(\omega_0 L)^2 + 2\omega_c R_L L + R_L^2}{L^2}s + \frac{3U_c\omega_0 L K_q \omega_c + \omega_c \omega_0^2 L^2 + \omega_c R_L^2}{L} \\ = s^3 + (A + 2B)s^2 + (2AB + B^2 + C^2)s + A(B^2 + C^2) \end{aligned} \tag{3.34}$$

Being A the real pole, B the real part of the conjugated poles and C the imaginary part. Since the real poles must be dominant, A is required to be ten times lower than B fulfilling the relation (3.35).

$$B = 10A \tag{3.35}$$

Relating the coefficient corresponding to s^2, s and the independent term of (3.34) and considering the relation (3.35), an equation system is obtained. The system outcomes are the real pole (3.36), the conjugated poles (3.37) and the required cut-off frequency (3.38).

$$p_1 = -6.5 \tag{3.36}$$

$$p_{2,3} = -65 \pm j313.68 \tag{3.37}$$

$$\omega_c = 1.59\, {}^{rad}/_{s} \tag{3.38}$$

Figure 37 shows the unitary step response depending on the cut-off frequency in addition to the response of the values around the obtained one. As can be seen, the response follows a first-order behaviour and has a time constant around 0.153 seconds and a settling time of 1 second that are very similar to the obtained for the active power control loop.

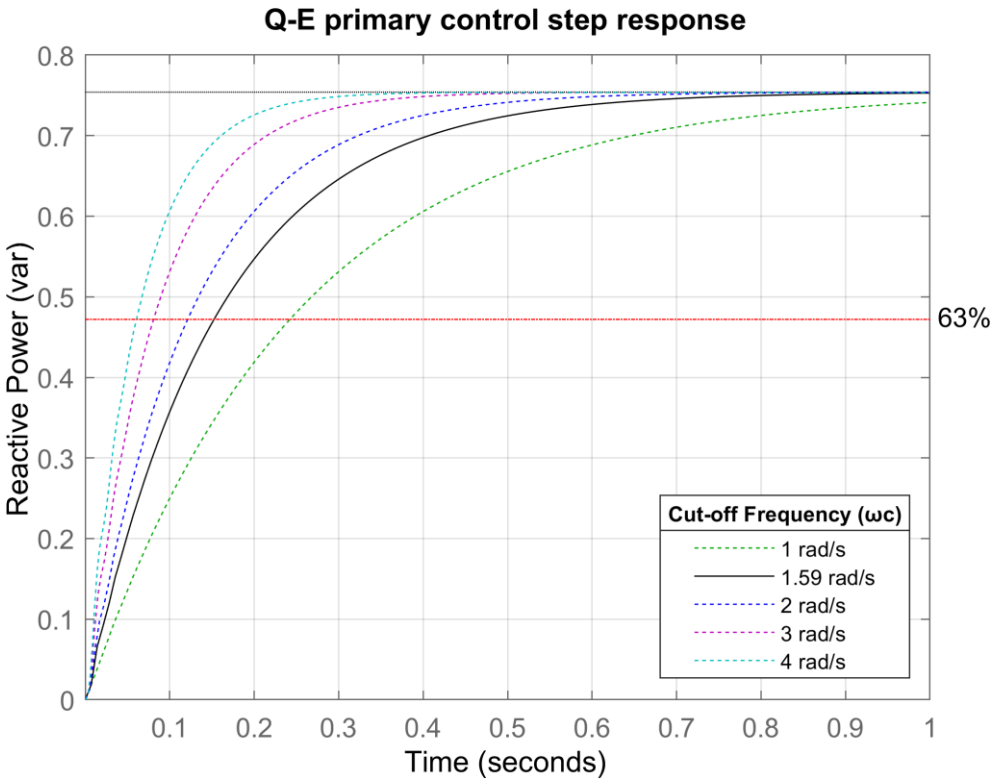

Figure 37 - Step response of the system depending on the cut-off frequency

c. Conclusions

To conclude, Table 2 shows the values of the droop gains and the LPF cut-off frequency calculated in this subsection.

Table 2 - Primary control parameters

Magnitude	*Value*	
	20 kVA	**40 kVA**
Active power droop gain (K_p)	$7.24 \cdot 10^{-6} \frac{rad/s}{W}$	$3.62 \cdot 10^{-6} \frac{rad/s}{W}$
Reactive power droop gain (K_q)	$800 \cdot 10^{-6} \frac{V}{var}$	$400 \cdot 10^{-6} \frac{V}{var}$
LPF cut-off frequency (ω_c)	$1.59\, {}^{rad}/_{s}$	$1.59\, {}^{rad}/_{s}$

3.3.3. Secondary control

This subsection aims to tune the secondary layer formed by the control loops responsible for the frequency and voltage levels restorations. Their action is included in the embedded control presented in this thesis, so it is required to decouple both actions in order to simplify the control loop analysis and avoid the conflicts between layers. However, the shared controllers, $K_i^{\omega}(s)$ and $K_i^{E}(s)$, shown in Figure 20 and Figure 22, are still considered for the tuning.

The controllers consist of integral controllers with a single constant, k_ω and k_E, that together with the weight factors, α and γ, forms the variables, $k_{sec}{}^{\omega}$ and $k_{sec}{}^{E}$, tuned in this subsection expressed in (3.39) and (3.40).

$$K_{sec}^{\omega}(s) = \alpha \cdot K_i{}^{\omega}(s) = \alpha \cdot \frac{k_\omega}{s} = \frac{k_{sec}^{\omega}}{s} \tag{3.39}$$

$$K_{sec}^{E}(s) = \gamma \cdot K_i{}^{E}(s) = \gamma \cdot \frac{k_E}{s} = \frac{k_{sec}^{E}}{s} \tag{3.40}$$

The dynamic of the secondary control is expected to be slower than the primary one, with stabilization times above the seconds. Therefore, the objective is to obtain a secondary control action with a first-order response with a time constant of around 1 second.

a. Frequency restoration control loop

This part aims to adjust the control loop responsible for the frequency restoration by calculating the variable, $k_{sec}{}^{\omega}$, that combines the weight factor, α, and the shared controller constant, ki^{ω}, as shown in (3.39). Considering this, the first idea of the block diagram of this control loop is obtained by simplifying the block diagram presented in Figure 20 and contemplating the secondary control action as the embedded control action. In this instance, the primary control is considered since its dynamics are faster than the secondary one and includes the plant dynamics of the system. The result is the block diagram shown in Figure 38.

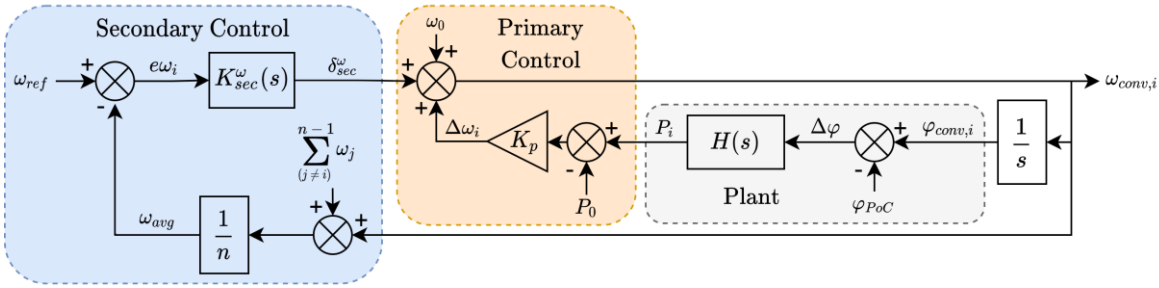

Figure 38 – Secondary frequency restoration control loop block diagram

The system is formed by the secondary control controller, the active power primary control, the plant, and the feedback, which contains the average frequency calculation since it is the variable used to obtain the offset. For simplicity, the nominal frequency, the phase at the PoC and the active power setpoint are deemed as perturbations and neglected. Furthermore, since the tuning is carried out by assuming that a unique generator forms the microgrid, the frequencies sent by the other generators are deemed null, so the offset is just computed with the own frequency. The outcome of these assumptions is a SISO system with an open-loop and closed-loop transfer functions represented in (3.41) and (3.42), respectively.

$$G_{OL}(s) = \frac{k^{\omega}_{sec}(L^2s^2 + 2R_LLs + ((\omega_0 L)^2 + R_L^2))}{L^2s^3 + 2R_LLs^2 + ((\omega_0 L)^2 + R_L^2)s + 3{U_c}^2\omega_0 LK_p} \tag{3.41}$$

$$G_{CL}(s) = \frac{k^{\omega}_{sec}(L^2s^2 + 2R_LLs + ((\omega_0 L)^2 + R_L^2))}{L^2s^3 + (k^{\omega}_{sec}L^2 + 2R_LL)s^2 + ((\omega_0 L)^2 + 2k^{\omega}_{sec}R_LL + R^2)s + k^{\omega}_{sec}((\omega_0 L)^2 + R_L^2) + 3{U_c}^2\omega_0 LK_p} \tag{3.42}$$

The system is type 0, as seen in the open-loop transfer function (3.41). Thus, it contemplates a steady-state error at its output in response to a step input. This is not desirable since the objective of this control loop is to correct the frequency deviation originated by the primary control. So, to eliminate the error, a pure integrator in the open loop is required.

However, this modification implies that the generator must supply an active power far above the nominal one to follow the frequency reference. The explanation for this assumption is based on the expression of the plant (3.3), which considers a power line connected to a strong grid, such as the general grid. This involves the generator supplying a power comparable to the grid short-circuit power to be able to modify the frequency of the system, which is technically impossible for a microgrid.

Consequently, the frequency restoration is not viable in the case the microgrid works in grid-connected mode. Furthermore, the tuning of the corresponding control loop is only considered in island mode. In this case, the generator is deemed to be connected to a weak grid with a voltage level that follows the one created by itself. To model the system in a simplified way, it has been contemplated that the generator is connected to a microgrid formed by a load, as shown in Figure 39.

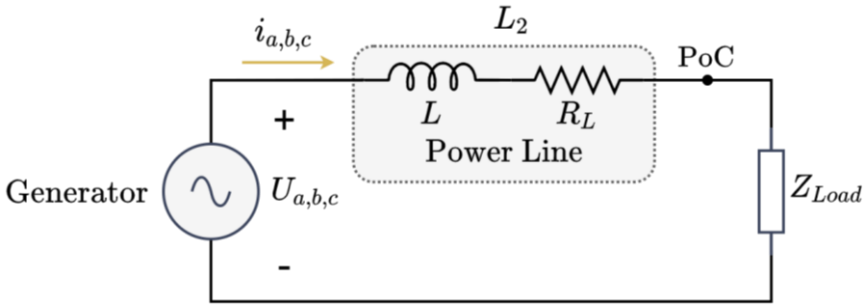

Figure 39 – Three-phase generator connected to a weak grid formed by loads

The presented circuit is formed by the generator, the load, and the power line between them that consists of the output inductor of the LCL filter. Considering this scheme and an RL load, the phase shift between the converter and the PoC in steady state is expressed in (3.43).

$$\varphi_{shift} = \arctan\left(\frac{X_{L_{load}}R_L - R_{load}X_L}{R_L R_{load} + R_{load}^2 + X_L X_{L_{load}} + X_{L_{load}}^2}\right) \tag{3.43}$$

The equation (3.43) can be simplified to equation (3.44), assuming that the load impedance is much greater than the power line, $Z_{Load} \gg X_L, R_L$.

$$\varphi_{shift} \cong \arctan\left(\frac{X_{L_{load}}R_L - R_{load}X_L}{R_{load}^2 + X_{L_{load}}^2}\right) \tag{3.44}$$

Based on this reasoning, it can be concluded that the phase drift is almost null, and consequently, the system frequency follows the generator one. Besides, considering (3.44), the phase drift depends on the system load. If the system load variation is also considered a perturbation, the block diagram dismisses the primary control, and the system is simplified, as shown in Figure 40.

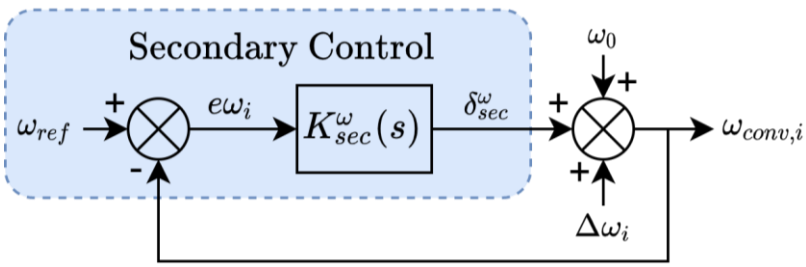

Figure 40 – Simplified secondary frequency restoration control loop block diagram

Now, the scheme is only formed by the secondary controller. So, the expressions of the open-loop transfer function and closed-loop transfer function are as shown in (3.45) and (3.46), respectively.

$$G_{OL}(s) = \frac{k_{sec}^{\omega}}{s} \tag{3.45}$$

$$G_{CL}(s) = \frac{k_{sec}^{\omega}}{s + k_{sec}^{\omega}} \tag{3.46}$$

The transfer functions of the system show no stability problems or permanent error. Also, the system has only one pole equal to the controller constant, $k_{sec}{}^{\omega}$. Knowing that, if the frequency restoration control time constant is set to 1 second, then the required controller constant must be equal to:

$$k_{sec}^{\omega} = \frac{1}{\tau} = \frac{1}{1s} = 1$$

b. Voltage restoration control loop

This subsection follows the same approach as the frequency restoration control loop to tune the voltage restoration one. So, the variable $k_{sec}{}^{E}$, which combines the weight factor, γ, and the shared controller constant, ki^{E}, as shown in (3.40), is adjusted to obtain a first-order response with a time constant of 1 second. In this instance, the block diagram is obtained by simplifying the block diagram of Figure 22, considering the embedded control action as the secondary control action and again, for the first thought, the primary control action is deemed. The outcome is the block diagram shown in Figure 41.

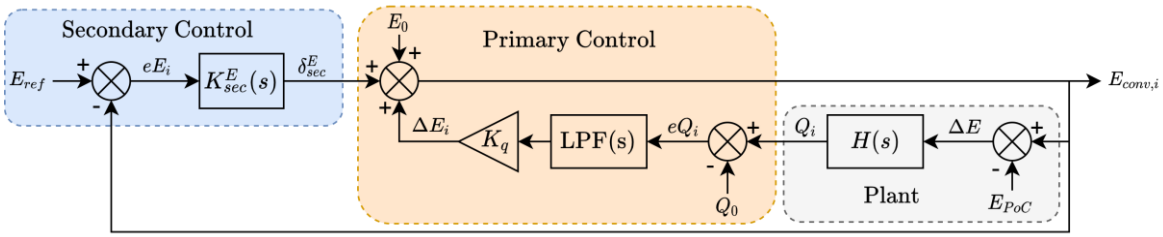

Figure 41 – Secondary voltage restoration control loop block diagram

The system is formed by the secondary control controller, the reactive power primary control and the plant. The nominal voltage, the amplitude at the PoC and the reactive power setpoints are considered perturbations and neglected. The result is a SISO system with an open-loop and closed-loop transfer functions as follows:

$$G_{OL}(s) = \frac{k_{sec}^{E}(L^2s^3 + (\omega_c L^2 + 2R_L L)s^2 + ((\omega_0 L)^2 + 2\omega_c R_L L + R_L^2)s + \omega_c((\omega_0 L)^2 + R_L^2))}{L^2s^4 + (\omega_c L^2 + 2R_L L)s^3 + ((\omega_0 L)^2 + 2\omega_c R_L L + R_L^2)s^2 + \left(3U_c\omega_0 L K_q \omega_c + \omega_c\omega_0^2 L^2 + \omega_c R_L^2\right)s} \quad (3.47)$$

$$G_{CL}(s) = \frac{as^3 + bs^2 + cs + d}{es^4 + fs^3 + gs^2 + hs + i} \quad (3.48)$$

Being:

$$a = k_{sec}^{E} L^2$$

$$b = k_{sec}^{E}(\omega_c L^2 + 2R_L L)$$

$$c = k_{sec}^{E}\left((\omega_0 L)^2 + 2\omega_c R_L L + R_L^2\right)$$

$$d = k_{sec}^{E}(\omega_c(\omega_0 L)^2 + \omega_c R_L^2)$$

$$e = L^2$$

$$f = k_{sec}^{E} L^2 + \omega_c L^2 + 2R_L L$$

$$g = k_{sec}^{E}(\omega_c L^2 + 2R_L L) + (\omega_0 L)^2 + 2\omega_c R_L L + R_L^2$$

$$h = k_{sec}^{E}(((\omega_0 L)^2 + 2\omega_c R_L L + R_L^2) + 3U_c\omega_0 L K_q \omega_c + \omega_c \omega_0^2 L^2 + \omega_c R_L^2$$

$$i = k_{sec}^{E}\omega_c((\omega_0 L)^2 + R_L^2)$$

The open-loop transfer function (3.41) shows that the system is type 1. Thus, it does not contemplate a permanent error at its output in response to a step input. In contrast to the frequency restoration, the voltage recovery can be obtained when the system works in grid-connection mode by injecting a reasonable amount of reactive power. However, to maintain the same tuning approach as the frequency restoration control loop, the system has been considered to work in island mode, which is when the voltage amplitude deviation is more notorious.

As has been done in the previous subsection, the generator is deemed to be connected to a weak grid modelled as a load, as seen in Figure 39, with a voltage amplitude that follows the one created by itself. Considering this scheme, the voltage difference between the converter and the PoC in steady state is expressed in the following expression:

$$\frac{E_{PoC}}{E_{generator}} = \frac{R_{load}R_L + R_{load}^2 + X_{load}X_L + X_{load}^2}{R_L^2 + 2R_L R_{load} + R_{load}^2 + X_L^2 + 2X_L X_{L_{load}} + X_{L_{load}}^2} \tag{3.49}$$

Once again, if the load impedance is assumed to be much greater than the power line, $Z_{Load} \gg X_L, R_L$, the expression (3.49) is simplified to (3.50).

$$\frac{E_{PoC}}{E_{generator}} \cong \frac{R_{load}^2 + X_{L_{load}}^2}{R_{load}^2 + X_{L_{load}}^2} \tag{3.50}$$

Based on this reasoning, it can be concluded that the voltage drop in the power line is almost null, and consequently, the system voltage follows the generator one and depends on the system load. If the system load variation is again considered a perturbation, the block diagram can be simplified as in Figure 42.

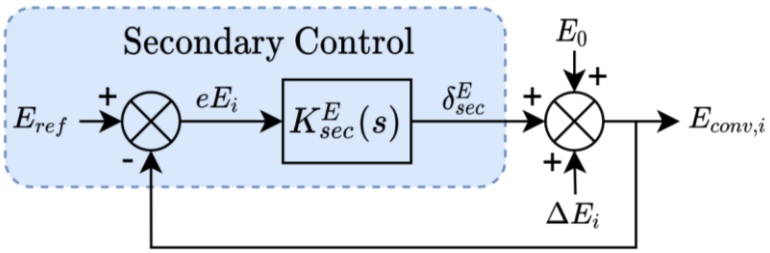

Figure 42 – Simplified secondary voltage restoration control loop block diagram

Now, the scheme is only formed by the secondary controller. So, the expressions of the open-loop transfer function and closed-loop transfer function are as follows:

$$G_{OL}(s) = \frac{k_{sec}^{E}}{s} \tag{3.51}$$

$$G_{CL}(s) = \frac{k_{sec}^{E}}{s + k_{sec}^{E}} \tag{3.52}$$

The transfer functions of the system show no stability problems or permanent error. Also, the system has only one pole equal to the controller constant, k_{sec}^{E}. Knowing that, if the voltage restoration control time constant is set to 1 second, then the required controller constant must be equal to:

$$k_{sec}^{E} = \frac{1}{\tau} = \frac{1}{1s} = 1$$

c. Conclusions

To conclude, Table 3 shows the values of the secondary control parameters calculated in this subsection.

Table 3 – Secondary control parameters

Magnitude	Value
Secondary frequency controller (k_{sec}^{ω})	1
Secondary voltage controller (k_{sec}^{E})	1

3.3.4. Tertiary control

The objective of this subsection is to tune the last layer of the hierarchical control, which is responsible for the power flow control. The tertiary control action is unified with the secondary control one, sharing the same controller. Furthermore, to simplify the analysis, both actions have been decoupled once again. This way, the controllers deemed for the control loops analysis consist of the integral shared controllers that, combined with the tertiary weight factors, β and ε, forms the variables, k_{tert}^{ω} and k_{tert}^{E}, tuned in this subsection:

$$K_{tert}^{\omega}(s) = \beta \cdot K_i{}^{\omega}(s) = \beta \cdot \frac{k_{\omega}}{s} = \frac{k_{tert}^{\omega}}{s} \tag{3.53}$$

$$K_{tert}^{E}(s) = \varepsilon \cdot K_i{}^{E}(s) = \varepsilon \cdot \frac{k_E}{s} = \frac{k_{tert}^{E}}{s} \tag{3.54}$$

The dynamic of the tertiary control is expected to be slower than the primary and secondary one, with stabilization times that can exceed the minute. However, this subsection aims to obtain a first-order response with a time constant of around 10 seconds considering the simulation time of the results shown in the next section.

a. Active power flow control loop

This subsection plans to calculate the tertiary control constant, k_{tert}^{ω}, accountable for the active power flow, that combines the weight factor, β, and the shared controller constant, k_i^{ω}, which makes the system stable and that meets the requirements. As done in the previous subsections, the general block diagram of Figure 20 is modified to obtain the required diagram. Now, the embedded control action is deemed only as of the action of the

tertiary control. Besides, the primary control is considered since its dynamic is faster than the tertiary one. Finally, the outcome is the block diagram shown in Figure 43

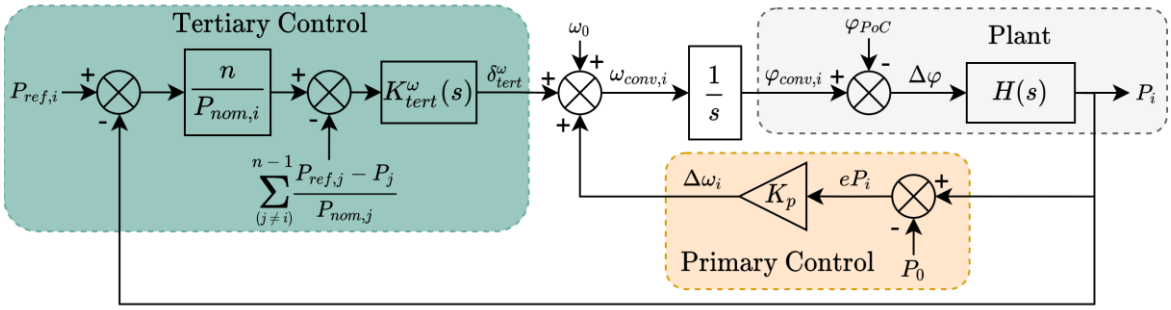

Figure 43 – Tertiary active power flow control loop block diagram

The primary and tertiary controls, the plant and an integrator constitute the scheme previously presented. In more detail, the tertiary control part is formed by its controller, that follows the expression (3.53), and the calculation of the difference of the disparities between the reference and the supplied active power of the neighbour generators and the own one has been explained in the subsection 3.2. However, as has been done with the second layer, the tuning is carried out by assuming that a single generator forms the microgrid to simplify the analysis. This way, the disparities of the neighbour generators are considered null. In addition, the nominal frequency of the PoC and the active power setpoint are also deemed as perturbations and neglected again. The result of these assumptions is a SISO system with transfer functions as follows:

$$G_{OL}(s) = \frac{3U_c^2\omega_0 L k^{\omega}_{tert}}{P_{nom}\left(L^2s^4 + 2R_L L s^3 + ((\omega_0 L)^2 + R_L^2)s^2 + 3U_c^2\omega_0 L K_p s\right)} \tag{3.55}$$

$$G_{CL}(s) = \frac{3U_c^2\omega_0 L k^{\omega}_{tert}}{P_{nom}L^2s^4 + 2R_L L P_{nom}s^3 + P_{nom}((\omega_0 L)^2 + R_L^2)s^2 + 3U_c^2\omega_0 L K_p P_{nom}s + 3U_c^2\omega_0 L k^{\omega}_{tert}} \tag{3.56}$$

The open-loop transfer function (3.55) exhibits a pure integrator, so the system does not present a permanent error to a step input. On the other hand, the closed-loop transfer function (3.56) shows a fourth-order system that contains four poles. With all this information, the active power flow control loop tuning can be performed. First, the controller constant limits are obtained considering the system stability and then, the constant that meets the dynamics requirement is calculated.

1. Stability analysis

The stability analysis examines how the system's poles evolve depending on the controller constant. For this, a root locus analysis is carried out from the system open-loop transfer function (3.55) with the variables of Table 1 and Table 2 substituted and the variable, P_{nom}, being the nominal power of the generators of 20kVA (20kW) as shown in the following expression:

$$G_{OL}(s) = \frac{27.32 \cdot 10^3 \cdot k^{\omega}_{tert}}{6 \cdot 10^{-3}s^4 + 811 \cdot 10^{-3}s^3 + 620.1s^2 + 3.95 \cdot 10^3 s} \tag{3.57}$$

Considering the expression (3.57) and the root locus gain as k_{tert}^{ω}, the analysis outcome is displayed in Figure 44. The graph shows the evolution of the four poles of the system, two

complex conjugates and another two that, as the controller constant increases, change from real to complex conjugates. Furthermore, these two last poles become in the right half-plane, evidence that a constant controller limit makes the system unstable.

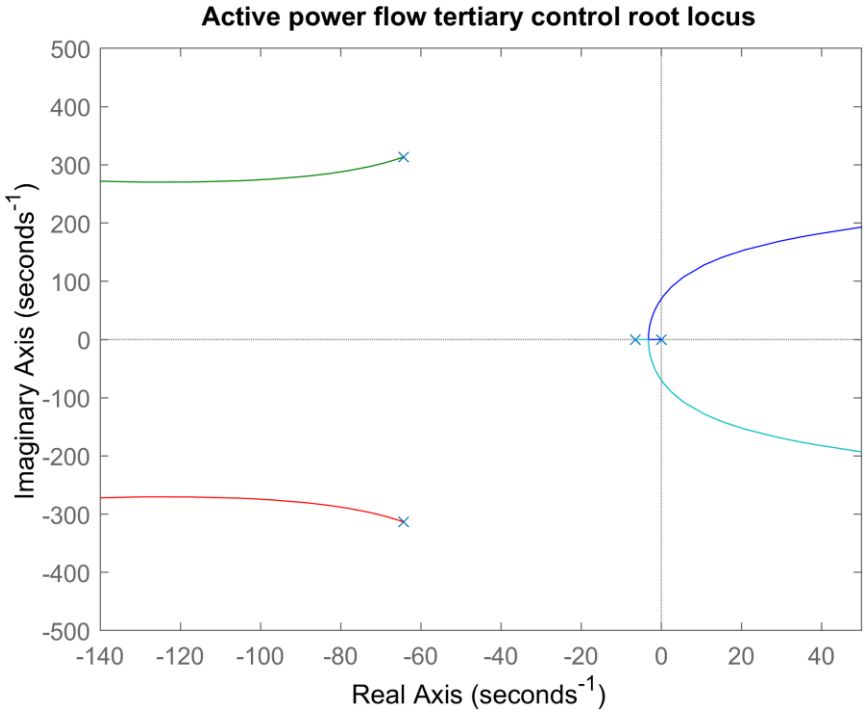

Figure 44 – Active power flow control loop root locus analysis

The denominator of the closed-loop transfer function (3.56) is studied in its isochronous form to obtain the maximum value of the tertiary controller constant considering stability.

$$D(s) = P_{nom}L^2s^4 + 2R_LLP_{nom}s^3 + P_{nom}\left((\omega_0 L)^2 + R_L^2\right)s^2 + 3U_c^2\omega_0 LK_pP_{nom}s + 3U_c^2\omega_0 Lk_{tert}^{\omega} \quad (3.58)$$

$$D(j\omega) = j^4P_{nom}L^2\omega^4 + j^32R_LLP_{nom}\omega^3 + j^2P_{nom}((\omega_0 L)^2 + R_L^2)\omega^2 + j3U_c^2\omega_0 LK_pP_{nom}\omega + 3U_c^2\omega_0 Lk_{tert}^{\omega} \quad (3.59)$$

The variables of the isochronous form (3.59) are substituted by the values of Table 1 and Table 2, and considering the generator of 20kVA, obtaining the following expression:

$$D(j\omega) = 6.006 \cdot 10^{-3}\omega^4 - j811 \cdot 10^{-3}\omega^3 - 620.1\omega^2 + j3.95 \cdot 10^3\omega + K_{limit} \quad (3.60)$$

Following the same procedure used for the primary control, the independent term is replaced by K_{limit}. Then the real and imaginary parts of the equation (3.60) are separated and equal to 0 to obtain a system of two equations as follows:

$$Re\left(D(j\omega)\right) = K_{limit} + 6.006 \cdot 10^{-3}\omega^4 - 620.1\omega^2 = 0 \quad (3.61)$$

$$Im\left(D(j\omega)\right) = 3.95 \cdot 10^3\omega - 811 \cdot 10^{-3}\omega^3 = 0 \quad (3.62)$$

Solving the equation system, a K_{limit} which makes the system critically stable is obtained. Finally, by matching it to the independent term of the characteristic equation (3.58), the maximum tertiary control controller can be calculated by means of the following equation:

$$K_{limit} = 3U_c^2\omega_0 Lk_{tert}^{\omega} \quad (3.63)$$

Again, if the already known variables (Table 1) are replaced from the equation (3.63), the maximum controller constant considering stability is obtained and shown below.

$$k^{\omega}_{tert\_max} = 105.5$$

If the nominal active power of the generator of 40kVA had been considered, the limit obtained would have been double, so the most restrictive case is the calculated one.

2. Dynamics

Once the stability analysis has been carried out, the final step is to obtain the k_{tert}^{ω} with which the system has a first-order response with a time constant of 10 seconds. According to the primary control tuning procedure, the system's poles depending on the controller constant have been first plotted with a sweep that extends to the stability limit to verify the calculated value, as shown in the pole-zero map shown in Figure 45.

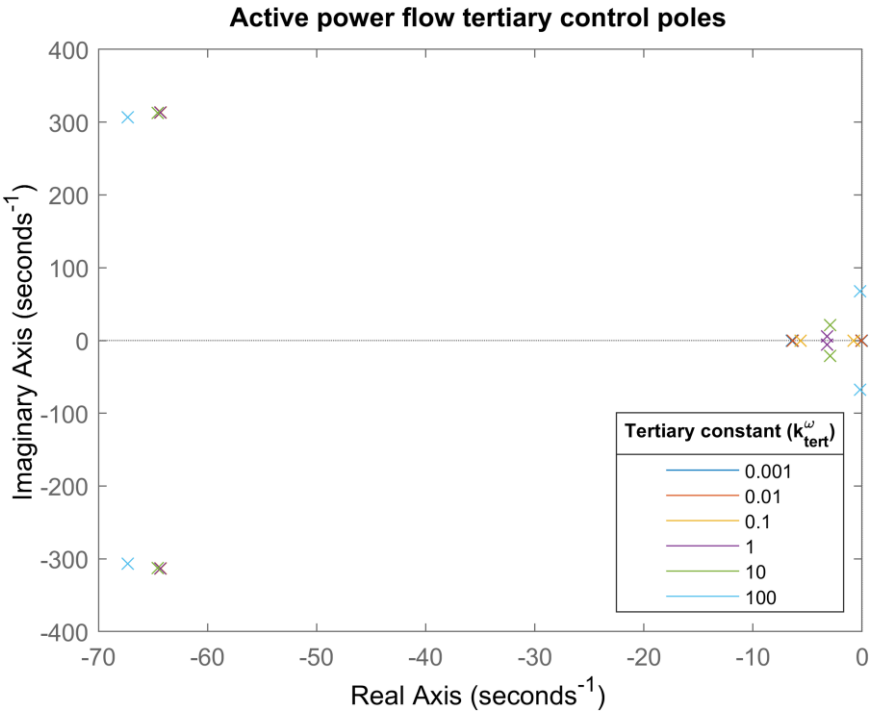

Figure 45 – Poles of the system depending on the tertiary controller constant

The pole-zero map shows that as the controller constant increases, two of the poles change from real to complex conjugate poles and approach the imaginary axis. Furthermore, the controller constants that meet the requirements are the smallest ones since the commented poles are real.

After studying the pole-zero map, the next step is to calculate the constant controller. For that purpose, the denominator of the closed-loop transfer function (3.56) is expressed depending on the poles and reorganized as follows:

$$P_{nom}L^2s^4 + 2R_LLP_{nom}s^3 + P_{nom}((\omega_0 L)^2 + R_L^2)s^2 + 3U_c^2\omega_0 LK_pP_{nom}s + 3U_c^2\omega_0 Lk^{\omega}_{tert} = (\mathrm{s} + \mathrm{A})(\mathrm{s} + \mathrm{B})(\mathrm{s} + (\mathrm{C} + \mathrm{jD}))(\mathrm{s} + (\mathrm{C} - \mathrm{jD})) \quad (3.64)$$

$$s^3 + \frac{2R_L}{L}s^3 + \frac{\omega L^2 + R_L^2}{L^2}s^2 + \frac{3{U_c}^2\omega_0 K_p}{L}s + \frac{3U_c^2\omega_0 k^{\omega}_{tert}}{P_{nom}L} = s^4 + (A + B + 2C)s^3 + (AB + 2AC + 2BC + C^2 + D^2)s^2 + (2ABC + AC^2 + AD^2 + BC^2 + BD^2)s + ABC^2 + \mathrm{ABD}^2 \quad (3.65)$$

Being A and B the real poles, C the real part and D the imaginary part of the conjugated poles. Since the time constant (τ) is fixed to be 10 seconds, the real pole A is set considering it by fulfilling the following relation:

$$A = \frac{1}{\tau} \tag{3.66}$$

Finally, an equation system is obtained relating the coefficient corresponding to s^4, s^3, s^2, s and the independent term of (3.65) and assuming the relation (3.66). The results of the system are:

$$p_1 = -0.1$$

$$p_2 = -6.32$$

$$p_{3,4} = -64.3 \pm j313.5$$

$$k^{\omega}_{tert,20} = 14.25 \cdot 10^{-3}$$

It should be noted that the real pole p_1 obtained meets the time constant requirement and is dominant, which meets the first-order response requirement.

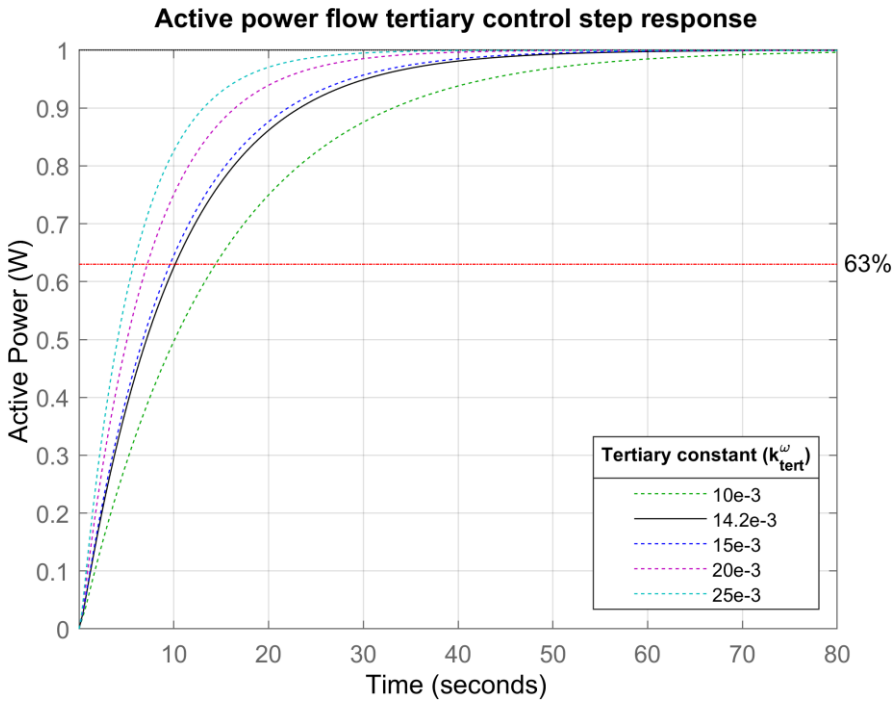

Figure 46 – Step response of the system depending on the tertiary controller constant

Figure 46 shows the unitary step response of the system with the calculated controller constant in addition to the responses with the values around the obtained one. As can be seen, the response follows a first-order behaviour and have a time constant of 10 seconds and a settling time of 60 seconds.

Following the same procedure carried out in this subsection, the controller constant for a generator of 40kVA of nominal power can be calculated. In this instance, the controller

constant that obtains a first-order response with a time constant of around 10 seconds is the double of the calculated for a generator of 20kVA, which means:

$$k^{\omega}_{tert,40} = 28.5 \cdot 10^{-3}$$

b. Reactive power flow control loop

This subsection aims to calculate the tertiary controller constant, k_{tert}^{E}, for the reactive power flow control loop. This constant combines the weight factor, ε, and the shared controller constant, k_i^E, following the expression (3.54). The block diagram required to analyse the control loop is shown in Figure 47, and it has been obtained by simplifying the Figure 22 diagram by considering the reactive power reference, $Q_{ref,I}$ as the input.

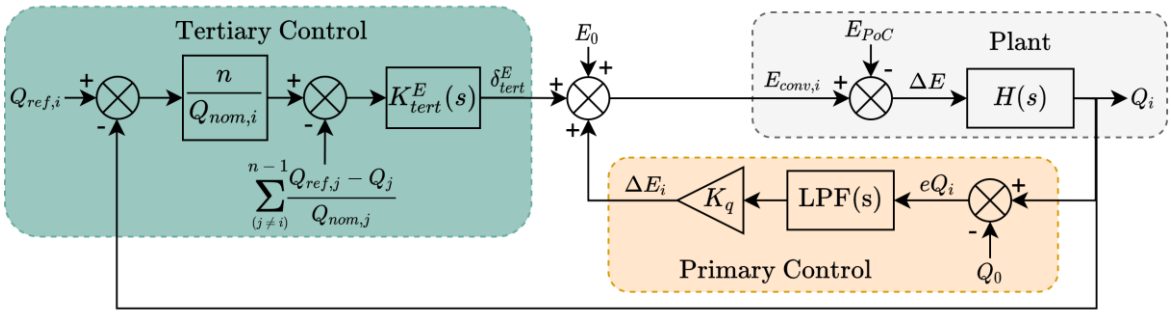

Figure 47 – Tertiary reactive power flow control loop block diagram

Now, the system is formed by the tertiary control, constituted by the tertiary controller and the calculation of the disparities of each generator as explained in subsection 3.2, the plant and the primary control, composed of the reactive droop gain and an LPF. For simplicity, the nominal voltage, the amplitude at the PoC, the reactive power setpoint, and the neighbour generators' disparities are considered perturbations and neglected. This way, the system becomes a SISO system with an open-loop and closed-loop transfer functions shown below:

$$G_{OL}(s) = \frac{3U_c\omega_0 Lk^E_{tert}s + 3U_c\omega_0 Lk^E_{tert}\omega_c}{Q_{nom}\left(L^2s^4 + (\omega_c L^2 + 2R_L L)s^3 + ((\omega_0 L)^2 + 2\omega_c R_L L + R_L^2)s^2 + (3U_c\omega_0 LK_q\omega_c + \omega_c\omega_0^2 L^2 + \omega_c R^2)s\right)} \quad (3.67)$$

$$G_{CL}(s) = \frac{as + b}{cs^4 + ds^3 + es^2 + fs + g} \quad (3.68)$$

Being:

$$a = 3U_c\omega_0 Lk^E_{tert}$$

$$b = 3U_c\omega_0 Lk^E_{tert}\omega_c$$

$$c = Q_{nom}L^2$$

$$d = Q_{nom}(\omega_c L^2 + 2R_L L)$$

$$e = Q_{nom}((\omega_0 L)^2 + 2\omega_c R_L L + R_L^2)$$

$$f = 3U_c\omega_0 LK_q\omega_c Q_{nom} + \omega_c Q_{nom}(\omega_0 L)^2 + 3U_c\omega_0 Lk^E_{tert} + \omega_c Q_{nom}R_L^2$$

$$g = 3U_c\omega_0 L k_{tert}^E \omega_c$$

The system is type 1, as seen in the open-loop transfer function (3.67), so it does not show permanent error in response to a step input. Besides, the system contains four poles since it is a four-order system and a zero. Once the transfer functions are obtained, the reactive power flow control loop tuning can be performed. First, the controller constant limits are obtained considering the system stability and then, the constant that meets the dynamics requirements is calculated.

1. Stability analysis

A root locus analysis has been accomplished to examine how the poles of the system change with variation of the controller constant. For this analysis, the system open-loop transfer function (3.67) with the variables of Table 1 and Table 2 substituted and the variable *Qnom* being the nominal reactive power of the generator is obtained.

$$G_{OL}(s) = \frac{(118.8s + 188.9) \cdot k_{tert}^{\omega}}{2.64 \cdot 10^{-3}s^4 + 361 \cdot 10^{-3}s^3 + 273.4s^2 + 1.76 \cdot 10^3 s} \quad (3.69)$$

Considering the expression (3.69) and the root locus gain as k_{tert}^{ω}, the analysis result is shown in Figure 48. The graph shows the evolutions of the four poles of the system in addition to the zero. Two of the poles are real, one of them is almost invariable, and near the imaginary axis, so the dominant pole is tuned to obtain a first-order response, and the other real pole moves away from the imaginary axis as the controller constant increases. The remaining poles are two complex-conjugated poles that evolve to the right half-plane, making the system unstable at a certain controller constant.

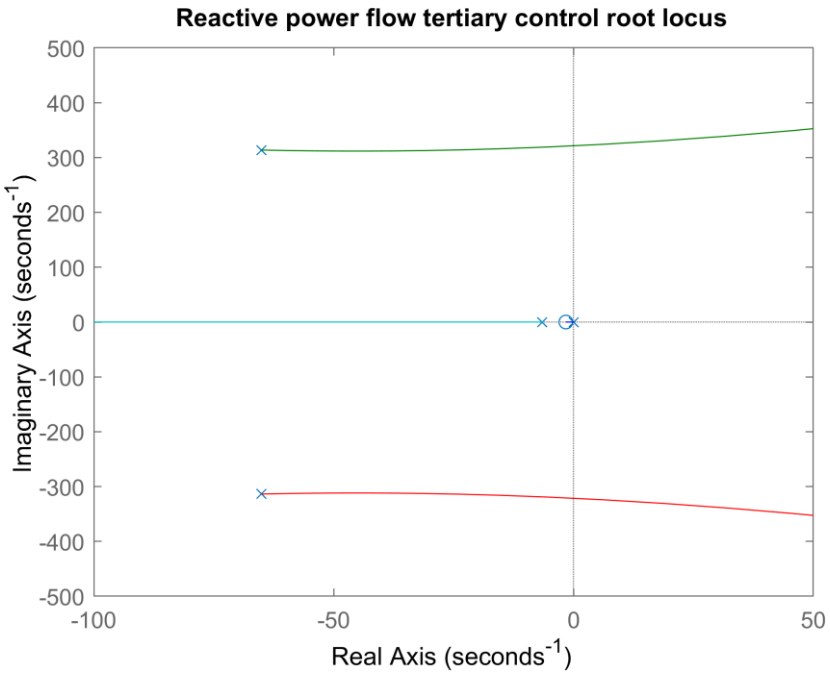

Figure 48 – Reactive power flow control loop root locus analysis

The denominator of the closed-loop transfer function (3.68) is studied in its isochronous form to obtain the maximum value of the tertiary controller constant considering stability.

$$D(s) = a^2s^4 + bs^3 + cs^2 + ds + e \tag{3.70}$$

$$D(j\omega) = j^4a\omega^4 + j^3b\omega^3 + j^2c\omega^2 + d\omega + e \tag{3.71}$$

Being:

$$a = Q_{nom}L^2$$

$$b = Q_{nom}(\omega_c L^2 + 2R_L L)$$

$$c = Q_{nom}((\omega_0 L)^2 + 2\omega_c R_L L + R_L^2)$$

$$d = 3U_c\omega_0 L K_q \omega_c Q_{nom} + \omega_c Q_{nom}(\omega_0 L)^2 + 3U_c\omega_0 L k_{tert}^E + \omega_c Q_{nom} R_L^2$$

$$e = 3U_c\omega_0 L k_{tert}^E \omega_c$$

The variables of the isochronous form (3.71) are substituted by the values of Table 1 and Table 2, and considering the generator of 20 kVA, obtaining the following equation:

$$D(j\omega) = 2.64 \cdot 10^{-3}\omega^4 - j361 \cdot 10^{-3}\omega^3 - 273.4\omega^2 + j(1.76 \cdot 10^3 + 118.8k_{tert}^E)\omega + K_{limit} \tag{3.72}$$

K_{limit} replaces the independent term, and the real and imaginary parts of the equation (3.72) are separated and equal to 0 to obtain an equation system as follows:

$$Re\big(D(j\omega)\big) = K_{limit} + 2.64 \cdot 10^{-3}\omega^4 - 273.4\omega^2 = 0 \tag{3.73}$$

$$Im\big(D(j\omega)\big) = (1.76 \cdot 10^3 + 118.8k_{tert}^E)\omega - 361 \cdot 10^{-3}\omega^3 = 0 \tag{3.74}$$

Solving the system, a K_{limit} that critically stabilises the system is obtained. Finally, by matching it to the independent term of the denominator (3.70), the maximum tertiary controller constant can be calculated with the following expression:

$$K_{limit} = 3U_c\omega L k_{tert}^E \omega_c \tag{3.75}$$

Once more, the variables of Table 1 and Table 2 are replaced from the equation (3.75), and the maximum controller constant considering stability is obtained and shown below.

$$k_{tert\_max}^E = 292.7$$

In this instance, the generator of 20 kVA is also the most restrictive case.

2. Dynamics

The last step is to obtain the controller constant with which the system has a first-order response with a time constant of 10 seconds. Depending on the controller constant, the pole-zero map has been plotted with a sweep extending up to the stability limit to verify the previously calculated limit.

Figure 49 displays that as the controller constant increases, the real poles move away from each other, and the conjugated poles approach the imaginary axis. Furthermore, the controller constants that meet the requirements are the smallest ones.

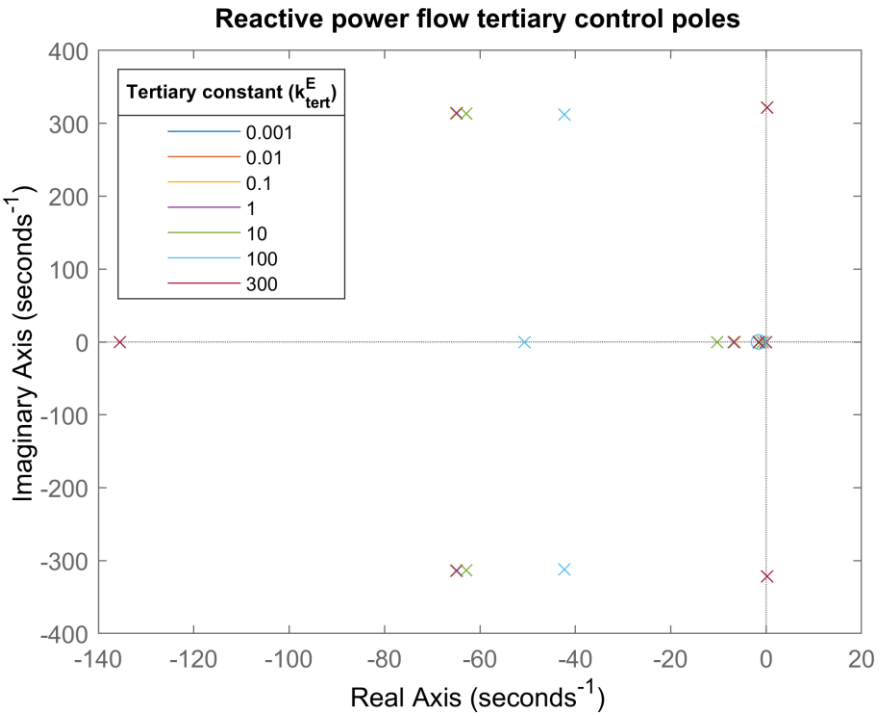

Figure 49 – Poles of the system depending on the tertiary controller constant

Once the pole-zero map is studied, the next step is to calculate the required constant controller according to the behaviour required. Thus, the denominator of the closed-loop transfer function (3.70) is expressed depending on the poles and reorganized as follows:

$$s^4 + \left(\frac{\omega_c L^2 + 2LR_L}{L^2}\right)s^3 + \left(\frac{(\omega_0 L)^2 + 2LR_L + R_L^2}{L^2}\right)s^2 + \left(\frac{3U_c\omega LK_q\omega_c Q_{nom} + \omega_c Q_{nom}(\omega_0 L)^2 + 3U_c\omega_0 Lk^E_{tert} + \omega_c Q_{nom}R_L^2}{Q_{nom}L^2}\right) + \left(\frac{3U_c\omega_0 k^E_{tert}\omega_c}{Q_{nom}L^2}\right) \quad (3.76)$$

$$s^4 + (A+B+2C)s^3 + (AB+2AC+2BC+C^2+D^2)s^2 + (2ABC+AC^2+AD^2+BC^2+BD^2)s + (ABC^2+\mathrm{ABD}^2)$$

Being A and Be the real poles, and C the real part and D the imaginary part of the conjugated poles. Since the time constant is fixed to be 10 seconds, the real pole A is set considering it by fulfilling the following relation:

$$A = \frac{1}{\tau} \quad (3.77)$$

An equation system is obtained by comparing the coefficients and the independent term of (3.77) and considering the relation (3.78). The system outcome is:

$$p_1 = -0.1$$

$$p_2 = -6.84$$

$$p_{3,4} = -64.84 \pm j313.7$$

$$k^E_{tert,20} = 0.981$$

The real pole p_1 obtained meets the time constant and first-order response requirements since it is dominant.

Figure 50 displays the unitary step response of the system with the calculated controller constant in addition to the responses with the values around the obtained one. As can be seen, the response follows a first-order behaviour and have a time constant of around 10 seconds and a settling time of 60 seconds.

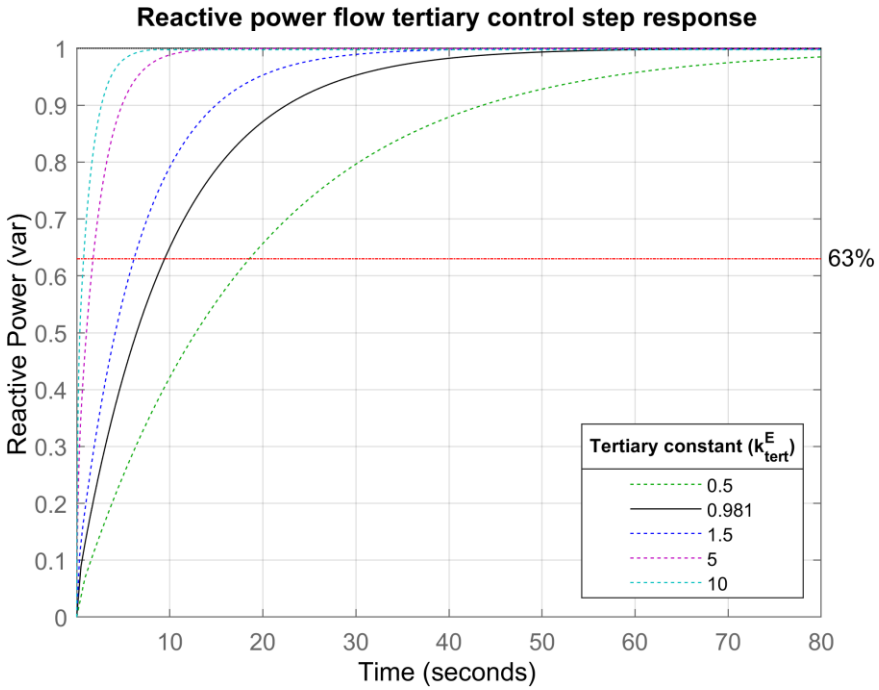

Figure 50 – Step response of the system depending on the tertiary controller constant

The controller constant for a generator with a nominal power of 40 kVA is calculated following the same procedure followed in this subsection. As in the active power flow control loop case, the constant obtained is the double the calculated for a generator of 20 kVA, which means:

$$k_{tert,40}^{E} = 1.962$$

c. Conclusions

To conclude, Table 4 resumes the values of the tertiary controller parameters calculated in this subsection.

Table 4 – Tertiary control parameters

Magnitude	***Value***	
	20 kVA	**40 kVA**
Tertiary active power controller (k_{tert}^{ω})	$14.25 \cdot 10^{-3}$	$28.5 \cdot 10^{-3}$
Tertiary reactive power controller (k_{tert}^{E})	0.981	1.962

3.3.5. Embedded control

Finally, this last subsection pretends to calculate the controller constants and the weight factors for which the previously studied control loops follow the required dynamics. Besides, this part addresses the conflicts when the secondary and tertiary control are unified. If both are activated simultaneously, the frequency and voltage restoration are performed as well as the active and reactive power flow, which can lead to steady-state errors. The embedded control follows the previously presented equations (3.1) and (3.2), in which the action of each control is weighted by employing an α, β, γ and ε factors. Thus, to analyse the dynamics of both controls, these factors must be studied.

a. The p-ω embedded control loop

First, the unification of frequency secondary control and active power tertiary control is studied. The equations (3.39) and (3.53) show the relations between the weight factors α and γ with the constant of the controller responsible for the frequency restoration and the active power flow, k_ω, and the control constants obtained in the previous subsections and displayed in Table 3 and Table 4. These relations form an equation system:

$$k_{sec}^{\omega} = \alpha k_{\omega} \tag{3.78}$$

$$k_{tert}^{\omega} = \beta k_{\omega} \tag{3.79}$$

The previous system contains two equations and three unknown variables, so to solve it, a relation between the weight factors is fixed in (3.80). The secondary and tertiary control layers' weights are assigned between 0 and 1.

$$\alpha + \beta = 1 \tag{3.80}$$

With all the relations defined, the control variables for each generator can be calculated. Considering the generator with a nominal power of 20 kVA, the results are as follows:

$$k_{\omega,20} = 1.014$$

$$\alpha_{20} = 0.986$$

$$\beta_{20} = 0.014$$

On the other hand, considering the 40 kVA generator, the constants are:

$$k_{\omega,40} = 1.028$$

$$\alpha_{40} = 0.972$$

$$\beta_{40} = 0.028$$

Once the control constants have been calculated, the next step is to study the dynamics of the unification of both controls. With this in mind, the control loops deeming the secondary control's action and the tertiary layer's action have been developed. The first one is shown in Figure 51.

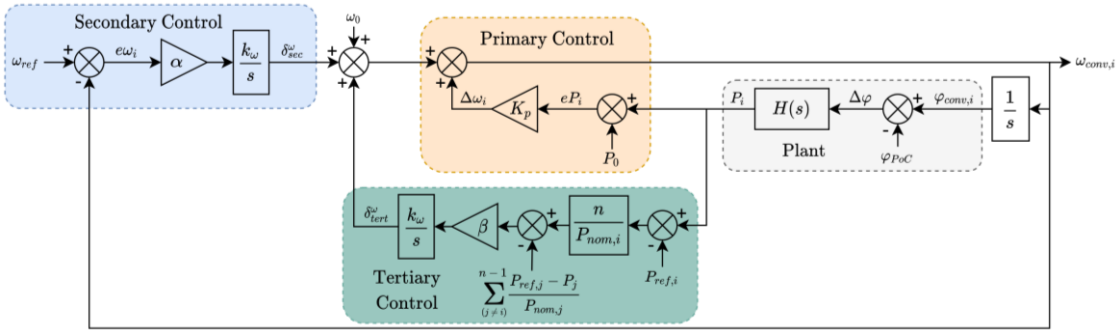

Figure 51 - P-ω embedded secondary control loop block diagram

Figure 51 is a modification of the control loop displayed in Figure 38, but in this case, it considers the action of the tertiary control. However, as explained in the corresponding subsection, when the microgrid is connected to the electrical grid, the generator cannot modify the system frequency. Thus, the analysis is performed when the microgrid is in island mode, resulting in the simplified block diagram of Figure 40, and consequently, the dynamics are deemed equal. Nevertheless, this simplification cannot be applied in the case of the tertiary control action.

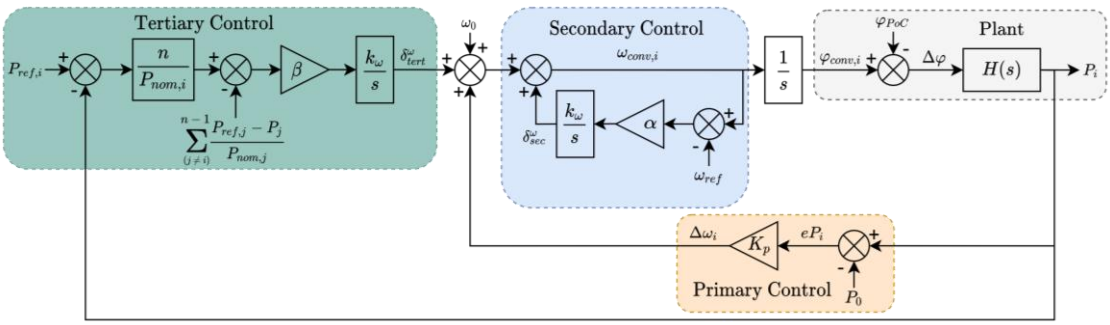

Figure 52 - P-ω embedded tertiary control loop block diagram

Figure 52 shows the modification of the block diagram of Figure 43, adding the secondary control action to the loop. Assuming the same simplifications as the previous subsections, the system turns into a SISO system with a the following open-loop and close-loop transfer functions:

$$G_{OL}(s) = \frac{a}{bs^4 + cs^3 + ds^2 + +es} \tag{3.81}$$

$$G_{CL}(s) = \frac{a}{bs^4 + cs^3 + ds^2 + es + a} \tag{3.82}$$

Being

$$a = 3k_\omega \beta U_c^2 \omega L$$

$$b = P_{nom} L^2$$

$$c = P_{nom}(k_\omega \alpha L^2 + 2LR_L)$$

$$d = P_{nom}((\omega_0 L)^2 + 2k_\omega \alpha R_L L + R_L^2)$$

$$e = P_{nom}(k_\omega \alpha(\omega_0 L)^2 + 3U_c^2 \omega_0 L K_p + k_\omega \alpha {R_L}^2)$$

The open-loop transfer function (3.81) exhibits a pure integrator, so the system does not present a steady-state error to a step input. The system dynamics maintain the first-order response but with a time constant of around 3 seconds slower, as seen in Figure 53.

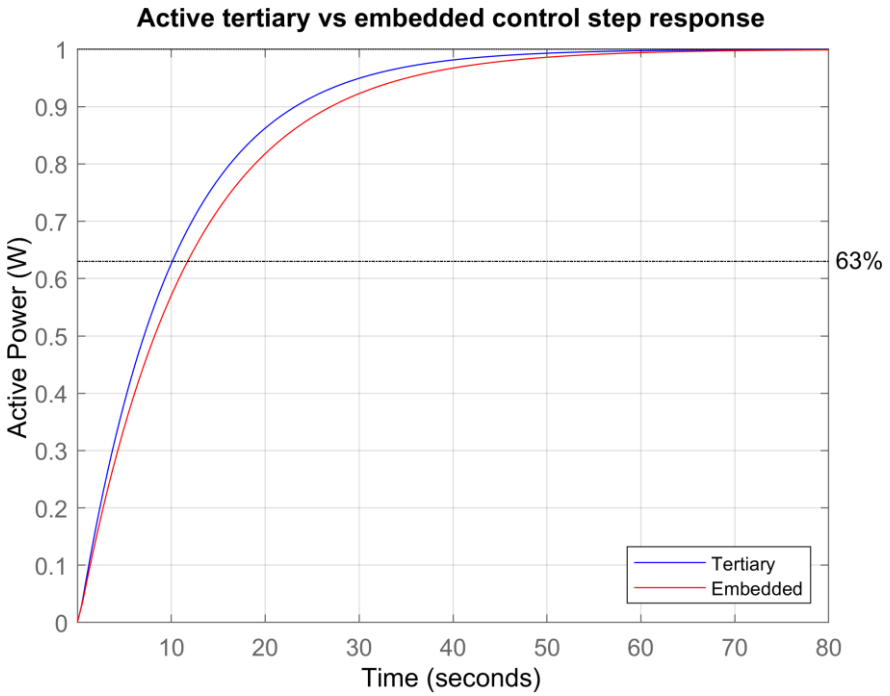

Figure 53 - Active tertiary vs embedded control step response

This means that the unification of both the frequency restoration control and the active power flow controller hardly affects the system dynamics for a single generator.

b. Q-E embedded control loop

Concerning the unification of the secondary voltage control and reactive power tertiary control, the approach to obtaining the controller gain has been maintained. The equations (3.40) and (3.54) present the relations between the weight factors β and ε, the controller constant, k_E, and the control constants previously calculated and displayed in Table 3 and Table 4. These relations establish the equation system below:

$$k_{sec}^E = \gamma k_E \tag{3.83}$$

$$k_{tert}^E = \varepsilon k_E \tag{3.84}$$

$$\gamma + \varepsilon = 1 \tag{3.85}$$

In this instance, the weights are also assigned between 0 and 1 as seen in (3.85). Solving the equation system, the results for a 20 kVA generator are:

$$k_{E,20} = 1.981$$

$$\gamma_{20} = 0.505$$

$$\varepsilon_{20} = 0.495$$

Conversely, considering a generator with a nominal power of 40 kVA, the results are as follows:

$$k_{E,40} = 2.962$$

$$\gamma_{40} = 0.338$$

$$\varepsilon_{40} = 0.662$$

Again, the next step is to study the dynamics with both controls embedded and consider the control constants obtained. For this purpose, the block diagram deeming the action of each control has been developed.

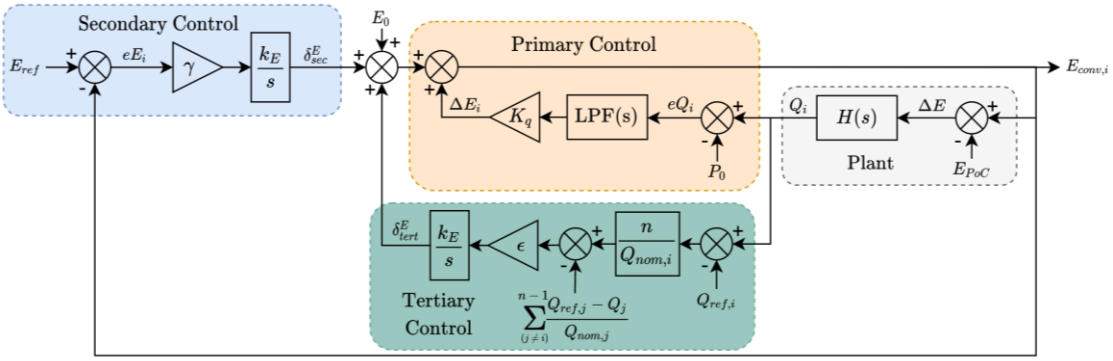

Figure 54 - Q-E embedded secondary control loop block diagram

Figure 54 shows the block diagram corresponding to the secondary control action with the following open-loop and closed-loop transfer functions:

$$G_{OL}(s) = \frac{as^3 + bs^2 + cs + d}{es^4 + fs^3 + gs^2 + hs + i} \tag{3.86}$$

$$G_{OL}(s) = \frac{as^3 + bs^2 + cs + d}{es^4 + js^3 + ks^2 + ls + m} \tag{3.87}$$

Being:

$$a = Q_{nom} k_E \gamma L^2$$

$$b = Q_{nom} k_E \gamma (L^2 \omega_c + 2LR_L)$$

$$c = Q_{nom} k_E \gamma ((\omega_0 L)^2 + 2LR_L \omega_c + R_L^2)$$

$$b = Q_{nom} k_E \gamma (L^2 \omega_c + 2LR_L)$$

$$e = Q_{nom} L^2$$

$$f = Q_{nom} (\omega_c L^2 + 2LR_L)$$

$$g = Q_{nom} ((\omega_0 L)^2 + 2\omega_c R_L L + R_L^2)$$

$$h = 3Q_{nom} \omega_c U_c \omega_0 L K_q + Q_{nom} \omega_c (\omega_0 L)^2 + 3k_E \varepsilon U_c \omega_0 L + Q_{nom} \omega_c {R_L}^2$$

$$i = 3\omega_c U_c k_E \varepsilon \omega_0 L$$

$$j = Q_{nom}(k_E \gamma L^2 + \omega_c L^2 + 2LR_L)$$

$$k = Q_{nom}(L^2 \omega_c \gamma k_E + (\omega_0 L)^2 + 2k_E \gamma L R_L + 2\omega_c R_L L + R_L^2)$$

$$l = L^2 Q_{nom} \gamma k_E {\omega_0}^2 + 3K_q Q_{nom} \omega_c U_c \omega_0 L + \omega_c Q_{nom} (\omega_0 L)^2 + 2LQ_{nom} R_L \omega_c k_E \gamma + 3k_E \varepsilon U_c \omega_0 L + Q_{nom} k_E \gamma {R_L}^2 + Q_{nom} \omega_c {R_L}^2$$

$$m = L^2 Q_{nom} \omega_c \gamma k_E {\omega_0}^2 + 3LU_c \omega_c k_E \omega_0 \varepsilon + {R_L}^2 Q_{nom} \omega_c \gamma k_E)$$

The open-loop transfer function (3.86) does not contain a pure integrator, so the system has a steady-state error. Apart from that, the system exhibits a first-order response slower, as seen in Figure 55.

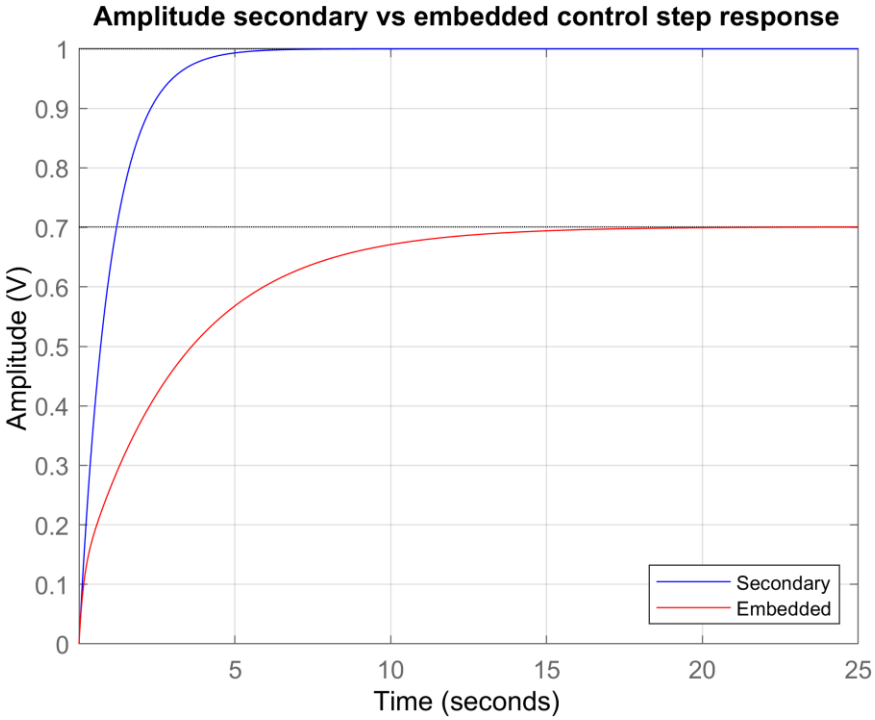

Figure 55 - Amplitude secondary vs embedded control step response

On the other hand, Figure 56 displays the modification of the block diagram of Figure 47, adding the secondary control action.

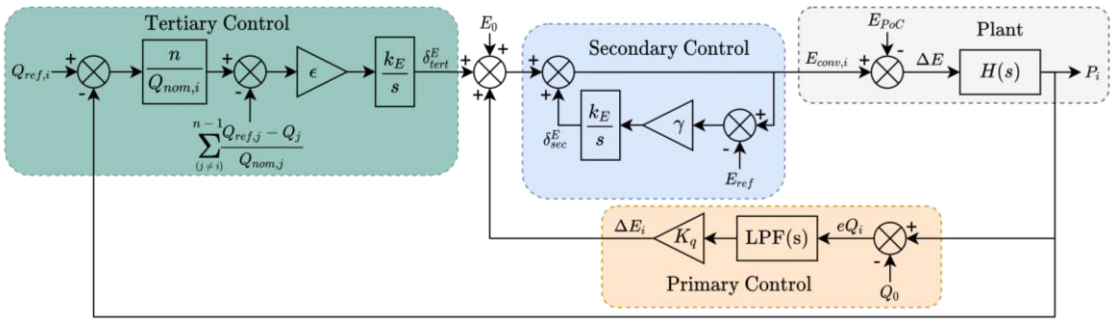

Figure 56 - Q-E embedded tertiary control loop block diagram

Simplifying the analysis, the result is a SISO system with the following transfer functions:

$$G_{OL}(s) = \frac{as + b}{cs^4 + ds^3 + es^2 + fs + g} \tag{3.88}$$

$$G_{OL}(s) = \frac{as + b}{cs^4 + ds^3 + es^2 + hs + i} \tag{3.89}$$

Being:

$$a = 3U_c\omega_0 L k_E \varepsilon$$

$$b = 3U_c\omega_0 L\omega_c k_E \varepsilon$$

$$c = Q_{nom}L^2$$

$$d = Q_{nom}(k_E\gamma L^2 + \omega_c L^2 + 2LR_L)$$

$$e = Q_{nom}(L^2\omega_c\gamma k_E + (\omega_0 L)^2 + 2k_E\gamma LR_L + 2\omega_c R_L L + R_L^2)$$

$$f = Q_{nom}\left(3K_q\omega_c U_c\omega_0 L + (\omega_c + k_E\gamma)(\omega_0 L)^2 + 2LR_L\omega_c\gamma k_E + k_E\gamma {R_L}^2 + \omega_c {R_L}^2\right)$$

$$g = Q_{nom}\left(L^2\omega_c\gamma k_E {\omega_0}^2 + {R_L}^2\omega_c\gamma k_E\right)$$

$$h = Q_{nom}\left(3K_q\omega_c U_c\omega_0 L + (\omega_c + k_E\gamma)(\omega_0 L)^2 + 2LR_L\omega_c\gamma k_E + k_E\gamma {R_L}^2 + \omega_c {R_L}^2\right) + 3k_E\varepsilon U_c L\omega_0$$

$$i = Q_{nom}\left(L^2\omega_c\gamma k_E {\omega_0}^2 + {R_L}^2\omega_c\gamma k_E\right) + 3k_E\varepsilon U_c\omega_0 L\omega_c$$

In this instance, the open-loop transfer function shows a steady-state error to a step input. Besides, the system's dynamics consist of a first-order response faster than the one obtained in the tertiary control subsection, as seen in Figure 57.

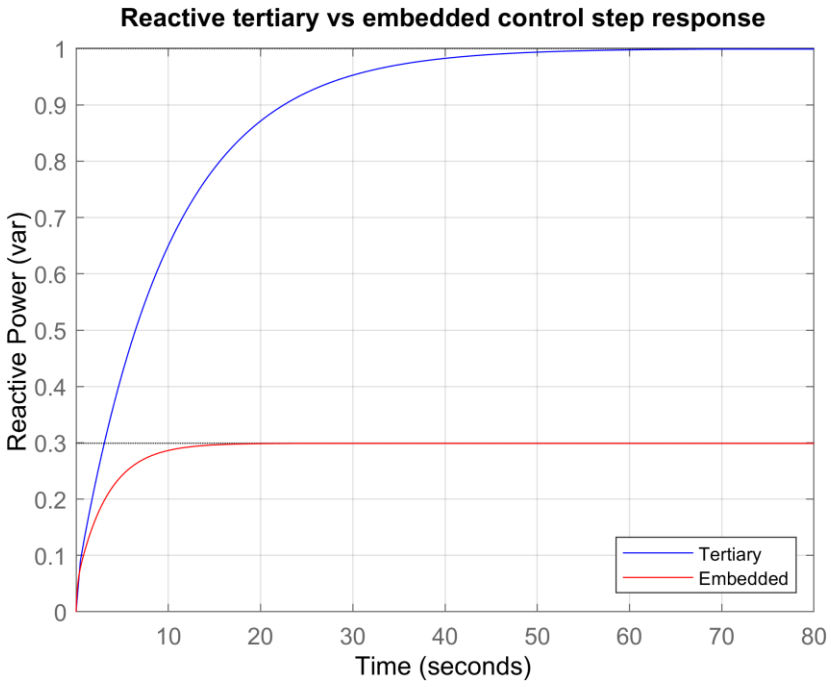

Figure 57 - Reactive tertiary vs embedded control step response

In conclusion, the unification of the amplitude restoration control and the reactive power flow control significantly affects their dynamics and effectiveness. This is due to the line impedance effect, as explained in the state of art section.

To obtain a relation between the effectiveness of the secondary and tertiary layers and the weight factors, the steady-state error expressions have been calculated:

$$SSE_{sec}{}^{E} = \frac{3U_c\omega_0 L\varepsilon}{Q_{nom}\gamma(\omega_0{}^2L^2 + R_L^2) + 3U_c\omega_0 L\varepsilon} \tag{3.90}$$

$$SSE_{tert}{}^{E} = \frac{Q_{nom}\gamma(\omega_0{}^2L^2 + R_L^2)}{Q_{nom}\gamma(\omega_0{}^2L^2 + R_L^2) + 3U_c\omega_0 L\varepsilon} \tag{3.91}$$

From these equations, it can be determined that as the weight of the tertiary control is significant, the permanent error exhibited by the secondary control regulation and the tertiary is inversely proportional. Figure 58 displays the steady-state error of each control depending on the weight factor *γ*. As can be seen, when *γ* is around 0.3, both controls contemplate the same error at their output. Thus, when the weight factor is reduced, the secondary control has a permanent error higher than the tertiary control and the opposite when the factor is increased.

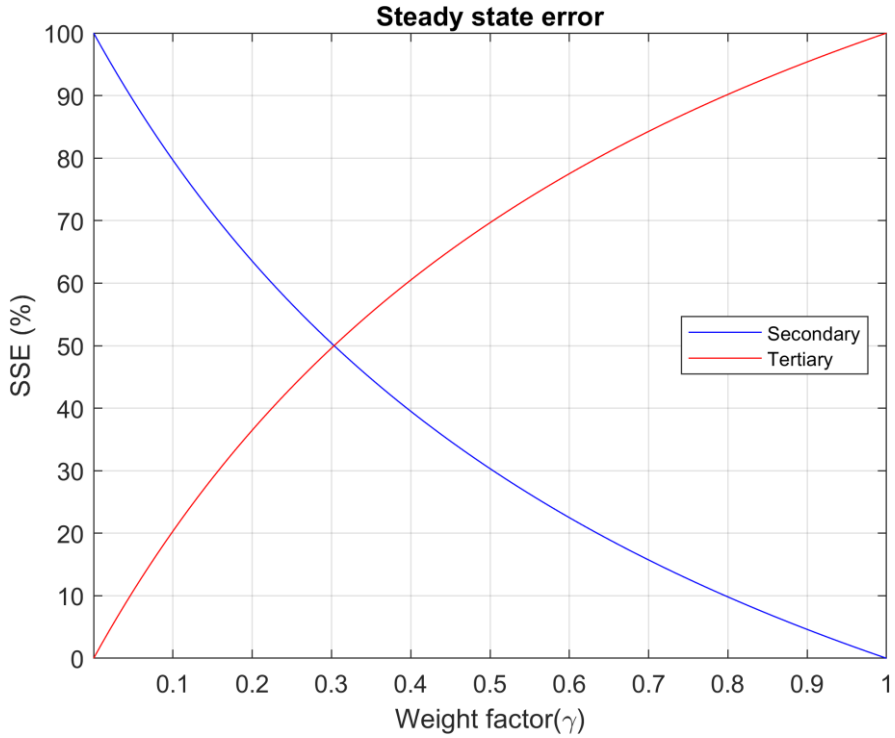

Figure 58 - Q-E embedded control steady-state error depending on the weight factors

c. Conclusions

To conclude, Table 5 shows the values of the weight factors and controller constants calculated in this subsection and the steady-state error contemplated by the Q-E control system considering the weight factors obtained.

Table 5 – Embedded control parameters

Magnitude	*Value*	
	20 kVA	**40 kVA**
Frequency secondary weight factor (α)	0.986	0.972
Amplitude secondary weight factor (β)	0.014	0.028
Active tertiary weight factor (γ)	0.505	0.338
Reactive tertiary weight factor (ε)	0.495	0.662
P-ω controller constant (k_ω)	1.014	1.028
Q-E controller constant (k_E)	1.981	2.962
Amplitude secondary control steady-state error	30%	47%
Reactive tertiary control steady-state error	70%	53%

4. Results

This section aims to validate the tuning results performed. These verifications are carried out through simulations and using the PLECS simulation software. The simulations are split into two configurations. The first set verifies the dynamics for a single generator, whereas the second set aims to check the behaviour of the control applied to the microgrid presented in Figure 17.

4.1. Single generator simulations

This subsection provides the results of simulating the single generator setup to validate the calculations done in Section 3. For this purpose, each layer of the proposed hierarchical control has been independently implemented and simulated. Besides, the control parameters deemed are the ones for a generator of 20 kVA to reduce the number of simulations.

4.1.1. Single generator setup

The distributed generator model developed (Figure 59) is divided into two parts. The electrical part consists of three controlled voltage sources emulating the inverter and connected through an RL line impedance to a triphasic load and an AC triphasic voltage source that characterises the electrical grid. The grid frequency and amplitude values and the line impedance are the ones given in Table 1. On the other hand, the signal part involves the three layers of the hierarchical control, the measurement of the active and reactive power, the generation of the voltage references and a phase-locked loop (PLL). The control parameters used are the ones given in Table 2 and Table 5 for a generator of 20 kVA of nominal power.

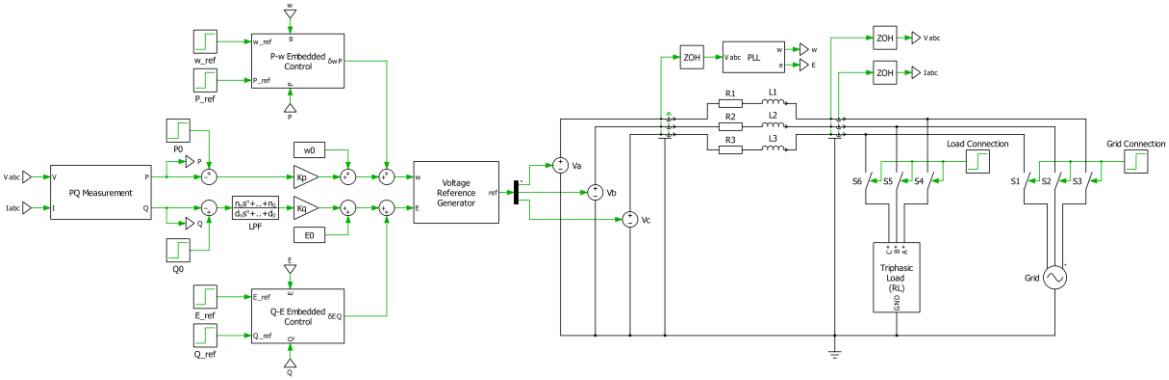

Figure 59 - PLECS model to simulate a distributed generator

The structure of the signal part is based on the hierarchical control diagram block shown in Figure 20 and Figure 22. The control inputs are obtained via the PQ Measurement block, which calculates the active and reactive power supplied by the generator with the measured voltages and currents of each phase, while the frequency and amplitude inputs are obtained by employing a PLL.

The primary control is implemented with blocks, while both embedded controls consist of C scripts that apply an algorithm that follows the equations (3.1) and (3.2) but for a single generator and are separated into two blocks called P-ω Embedded Control and Q-E Embedded Control. Their outputs are the frequency and amplitude of the voltage that the

converter must generate. The block called Voltage Reference Generator creates these references.

Once the model is explained, the primary, secondary and tertiary dynamics obtained in Section 3 are validated.

4.1.2. Primary control

To independently validate the primary control, the outputs of the embedded control block are not utilized. This way, the tests performed consisted in applying a variation in the active and reactive power setpoint controlled by the steps *P0* and *Q0* of the model.

In the first test, a variation of 1 pu in the active power setpoint is applied to validate the primary active power control dynamics. As shown in Figure 60, the dynamics match the expected behaviour, shown in Figure 27, of the control loop of Figure 23 used to tune the control loop. However, in the case of the reactive power, the dynamics do not follow the expected response, as seen in Figure 61. The simulation behaviour is slower and contemplates a steady-state error more significant than the predicted one, shown in Figure 37. Despite this, the results remain of first order and fast enough. This deviation is caused by the considerations taken to linearize the plant's transfer function (3.4) used to tune the control loop of Figure 31. The line is assumed to be inductive, but it also has a resistive component eliminated during the linearization that, if not considered, leads to certain errors when tuning the system.

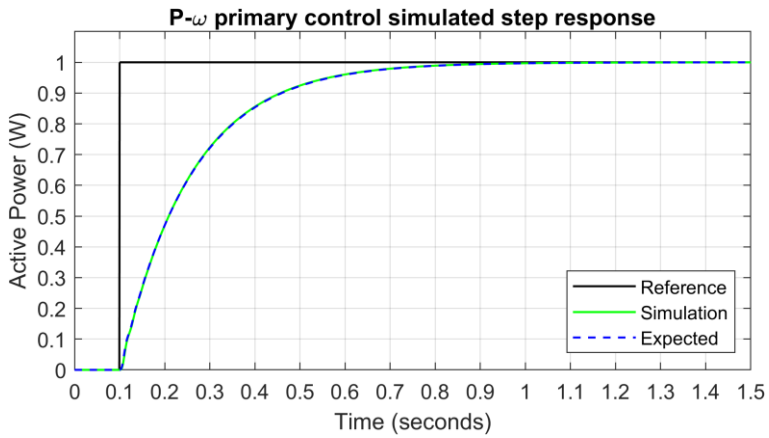

Figure 60 - Results of the simulation of the active power primary control with a single generator

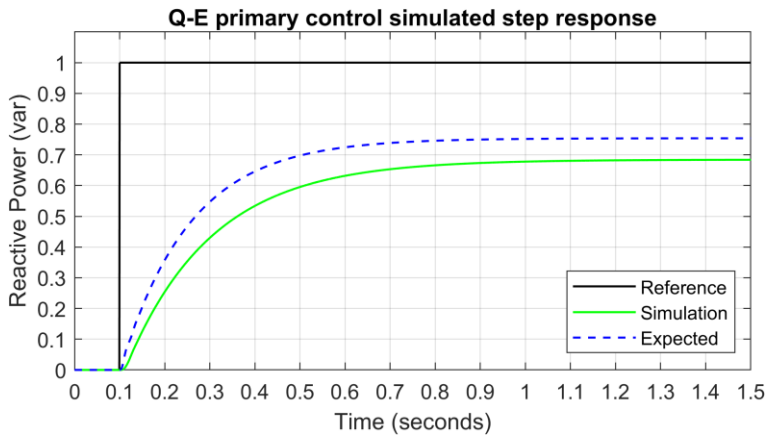

Figure 61 - Results of the simulation of the reactive power primary control with a single generator

4.1.3. Secondary control

The validation of the secondary control has been carried out by disconnecting the three-phase voltage source and replacing it with a triphasic load since the modification of the frequency and amplitude is technically impossible when the grid is connected, as explained in the subsection 3.3.3.

Besides, the action of the tertiary control has been neglected by setting the weight factors β and ε to 0 in the algorithms. Figure 62 and Figure 63 show that the model's dynamics match with the expected behaviour of the control loops of Figure 40 and Figure 42, respectively, when the frequency and amplitude reference steps, *w_ref* and *E_ref*, impose a variation of 1 unit.

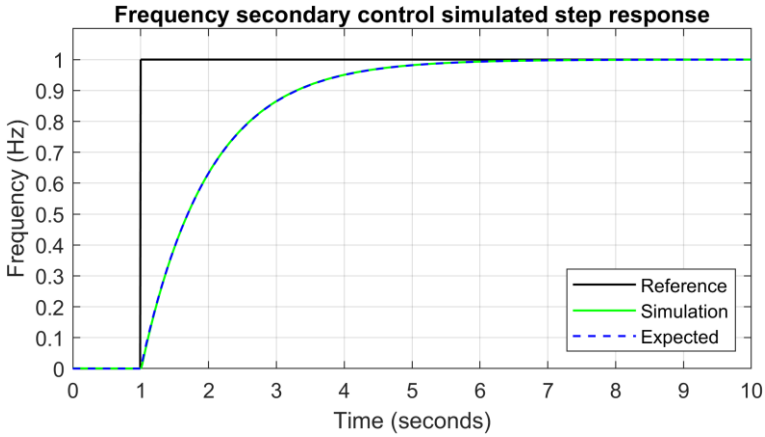

Figure 62 - Results of the simulation of the frequency secondary control with a single generator

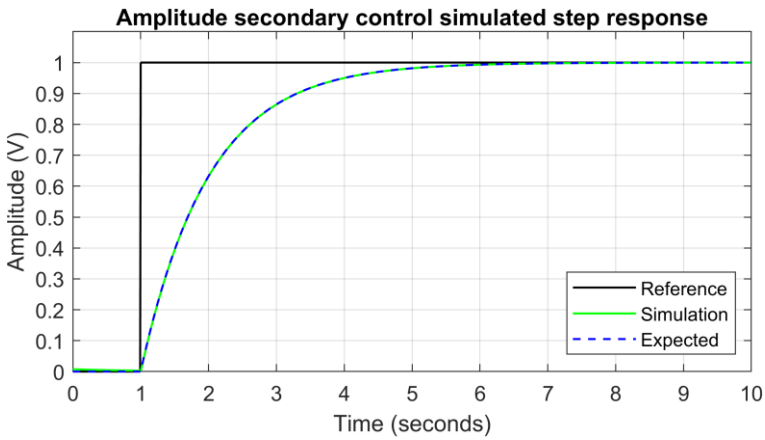

Figure 63 - Results of the simulation of the amplitude secondary control with a single generator

4.1.4. Tertiary control

For the validation of the tertiary control, the action of the secondary control has been decoupled from the model by setting the weight factors α and γ to 0 in the algorithms. In this instance, the active and reactive power reference steps, *P_ref* and *Q_ref*, apply a variation of 1 to test the model. Figure 64 and Figure 65 present the results of the simulations. The active power flow tertiary control response follows the expected behaviour, displayed in Figure 46, but the reactive power one is slower than the predicted one, shown in Figure 50, but remains of first order and is fast enough. This deviation could be attributed to the same reasons as the primary control.

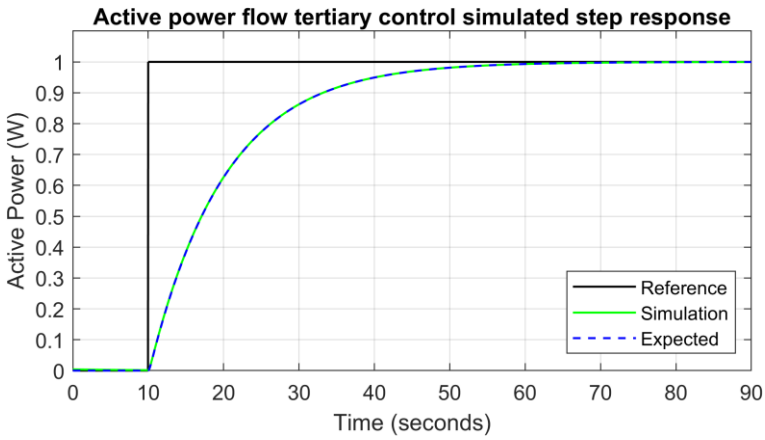

Figure 64 - Results of the simulation of the active power flow tertiary control with a single generator

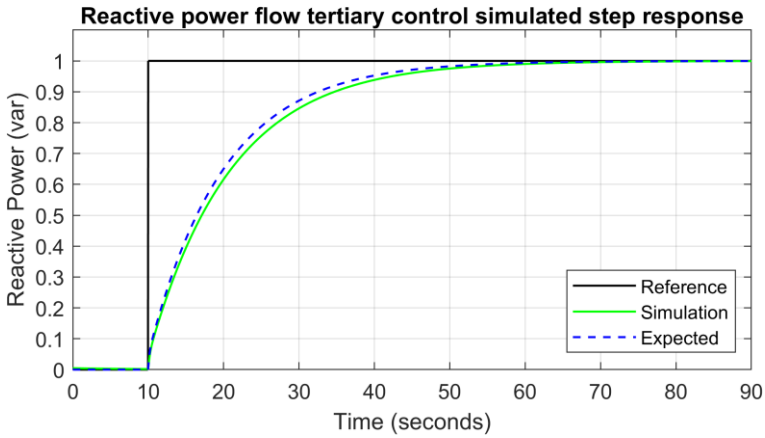

Figure 65 - Results of the simulation of the reactive power flow tertiary control with a single generator

4.1.5. Embedded control

Finally, the embedded control is validated without modifying the base model of Figure 59.

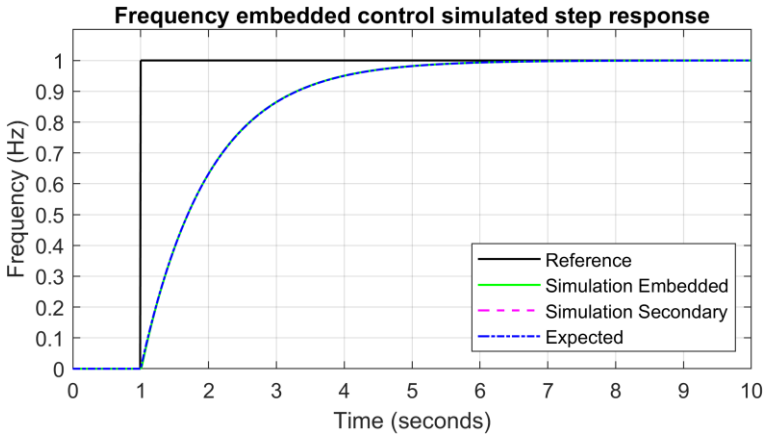

Figure 66 - Results of the simulation of the frequency embedded control with a single generator

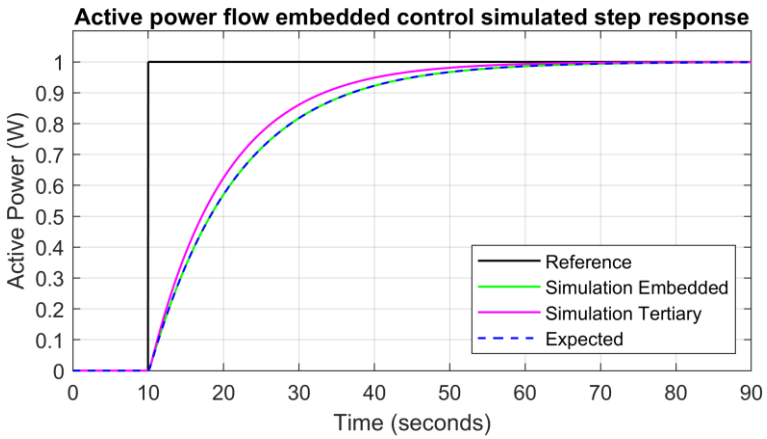

Figure 67 - Results of the simulation of the active power flow embedded control with a single generator

In Figure 66 and Figure 67, the simulations perfectly match the expected behaviours, but there are differences in Figure 66 and Figure 67. In the case of the amplitude embedded control, the response is better than expected since the steady-state error goes from 30% to a value of around 23%. On the other hand, the reactive power flow embedded control presents a permanent error more significant than the predicted one. In this instance, the error goes from 70% to 77%. These deviations could be attributed to the same reasons as the primary control.

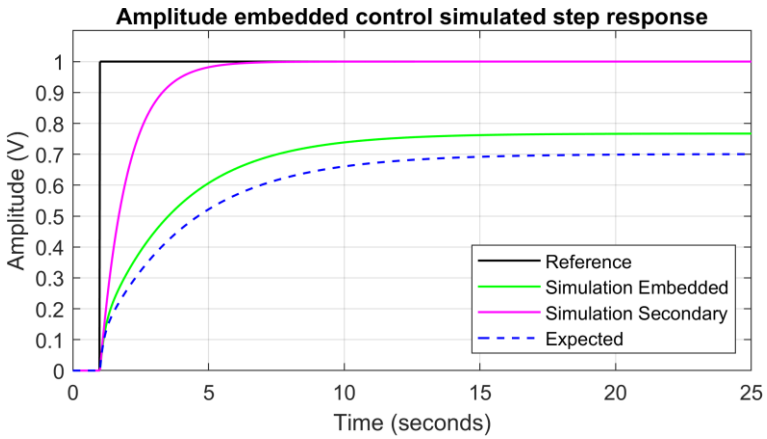

Figure 68 - Results of the simulation of the amplitude embedded control with a single generator

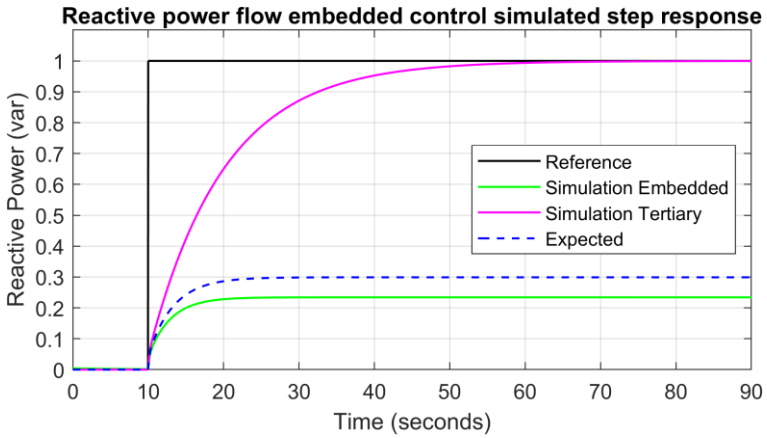

Figure 69 - Results of the simulation of the reactive power flow embedded control with a single generator

4.2. Microgrid simulations

This subsection provides the results of simulating the microgrid setup to study the dynamics when the proposed control is applied in a more complex system.

4.2.1. Microgrid setup

The microgrid model developed is shown in the following figure:

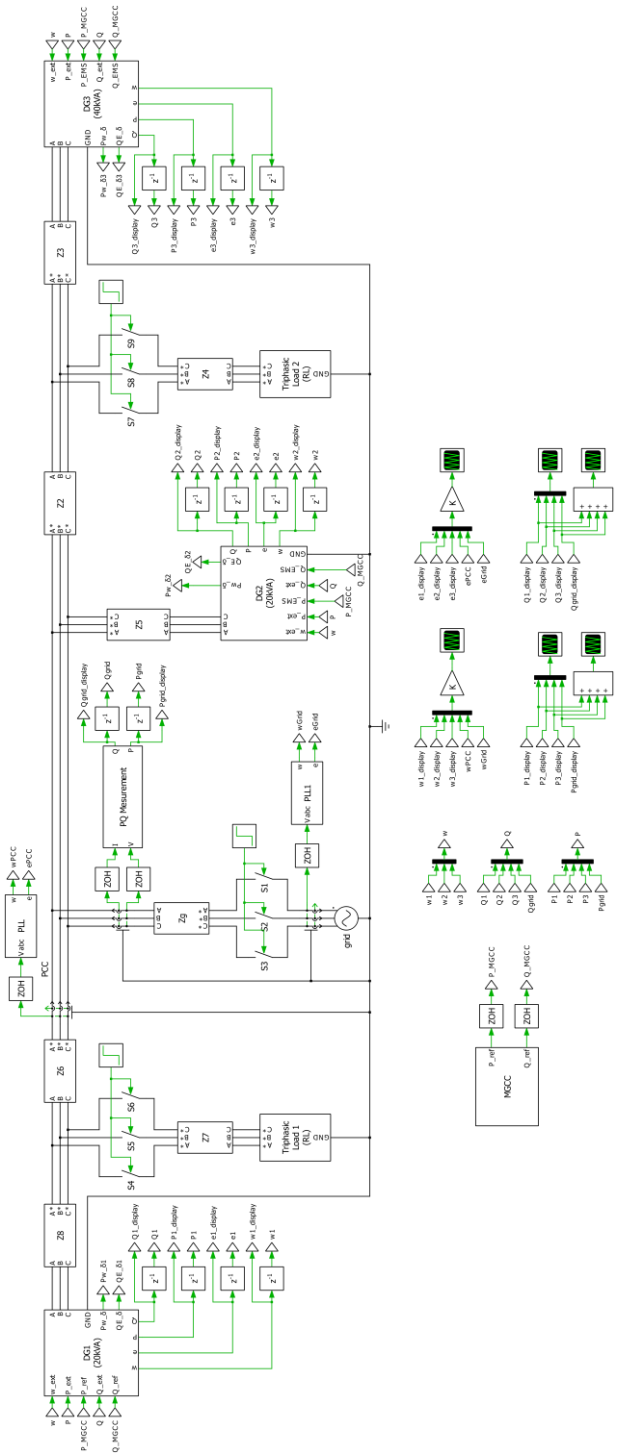

Figure 70 - PLECS model to simulate the proposed microgrid

As can be seen, the microgrid follows the same scheme as the one presented in Figure 17. It is formed by three generators based on the model of Figure 59, the generators DG1 and DG2 have a nominal power of 20 kVA, and the generator DG3 has a nominal power of 40 kVA.

The control parameters applied in each generator are given in Table 2 and Table 5, depending on their nominal power. Moreover, two RL triphasic loads of 20 kVA, Load 1 and Load 2, can be connected to the system by employing controlled switches. The parameters of these loads are presented in the following table:

Table 6 - Triphasic load parameters

Magnitude	Value
Nominal power (S)	$20\ kVA$
Active power (P)	$\approx 18\ kW$
Reactive power (Q)	$\approx 2\ kvar$
Resistance (R_{load})	8.72Ω
Inductance (L_{load})	$280.6mH$

Another essential element is the grid, characterised by a three-phase voltage source and connected to the system through an impedance (Z_g) and a controlled switch. A PQ Measurement block obtains the power supplied or received by the grid. The table below shows its parameters:

Table 7 - Grid parameters

Magnitude	Value
Nominal voltage amplitude (E_{grid})	$230\sqrt{2}\ V$
Nominal frequency (f_{grid})	$50\ Hz$
Nominal power (S_{grid})	$86\ kVA$
Resistance (R_{grid})	$1.7\ m\Omega$
Inductance (L_{grid})	$25.69\ \mu H$

For the purpose of simulating the tertiary and embedded control for more than one generator, the active and reactive power references must be modified during the simulation. This way, a block called MGCC has been added and consists of a C script that changes the power reference when requested. Finally, all these elements are interconnected through several line impedances with the following parameters:

Table 8 - Line impedances parameters

Magnitude	*Value*						
	Z_2	Z_3	Z_4	Z_5	Z_6	Z_7	Z_8
Resistance (mΩ)	15.288	36.134	69.824	116	23.201	72.268	72.268
Inductance (μH)	35.53	67.95	131.31	269.6	53.91	135.9	135.9

Once the model is explained, the hierarchical control layers are simulated in island and grid-connected mode. In this case, the control is studied by observing the behaviour in relation to a change in the system load or the power references. The magnitudes observed in each case are the frequency and voltage at each generator PoC and microgrid PCC and the active and reactive power supplied by each generator and the grid.

4.2.2. Primary control

The primary control is independently simulated by deactivating the action of the secondary and tertiary control. Furthermore, the tests performed consist of connecting the Load 1 at second 2 and the Load 2 two seconds later. This way, the virtual inertia and the system's power distribution applied by the primary control can be checked.

a. Island mode

In island mode, the primary control generates a steady-state error in the frequency and amplitude whenever there is a discrepancy between the power supplied and consumed due to the virtual inertia. This can be observed in Figure 71 and Figure 72.

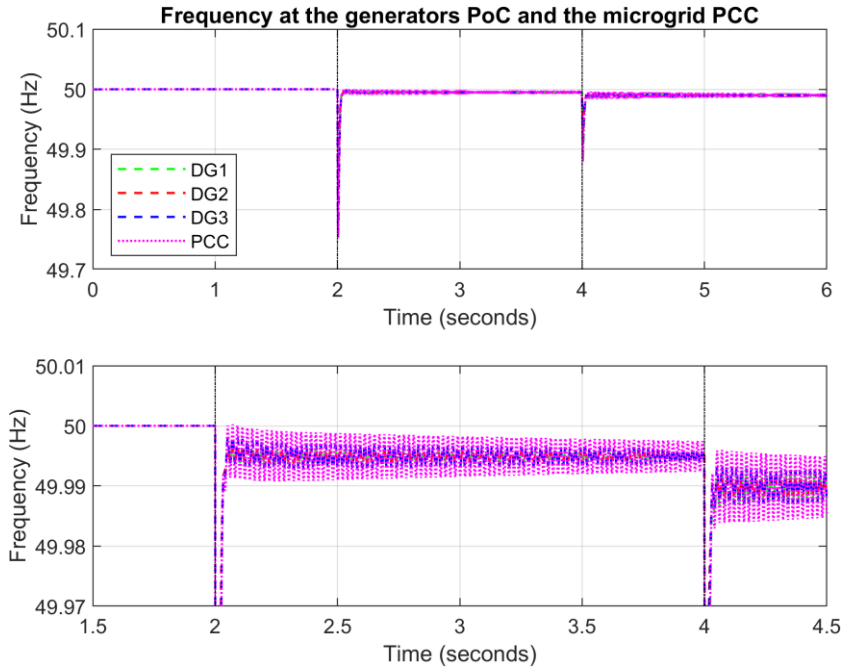

Figure 71 - Results of the simulation of the frequency at the generators PoC and the microgrid PCC in island mode with primary control

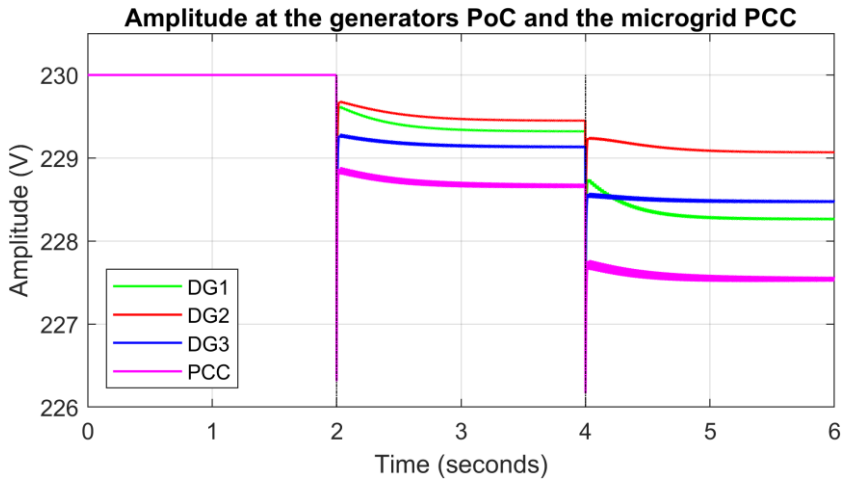

Figure 72 - Results of the simulation of the amplitude at the generators PoC and the microgrid PCC in island mode with primary control

Figure 71 shows the active power distribution by the generators. When a load is connected, the power supplied is shared depending on the droop gain applied to the generator, generally following a first-order behaviour with a settling time of around 1 second. The distribution is correctly achieved since the generator with a nominal power of 40 kVA supplies twice the 20 kVA generators.

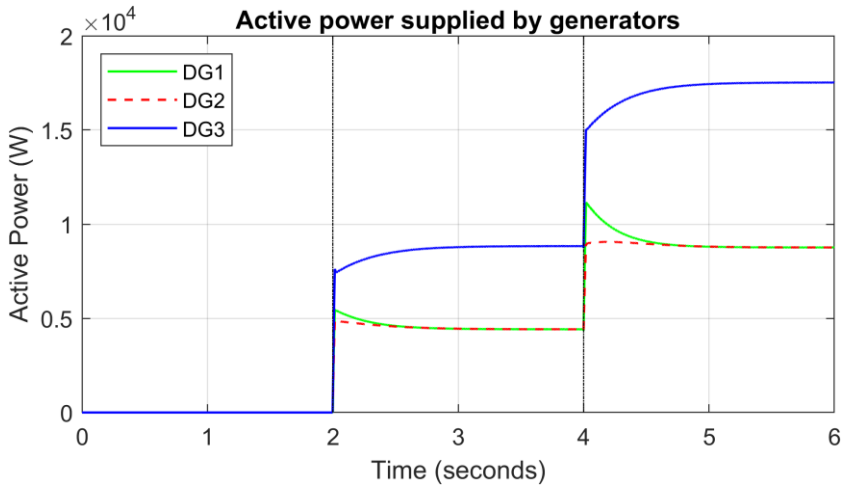

Figure 73 - Results of the simulation of the active power supplied by generators in island mode with primary control

However, the reactive power distribution shown in Figure 74 is not accurate due to the line impedance effect explained in subsection 2.2 but follows the first-order dynamics with the expected settling time of 1 second.

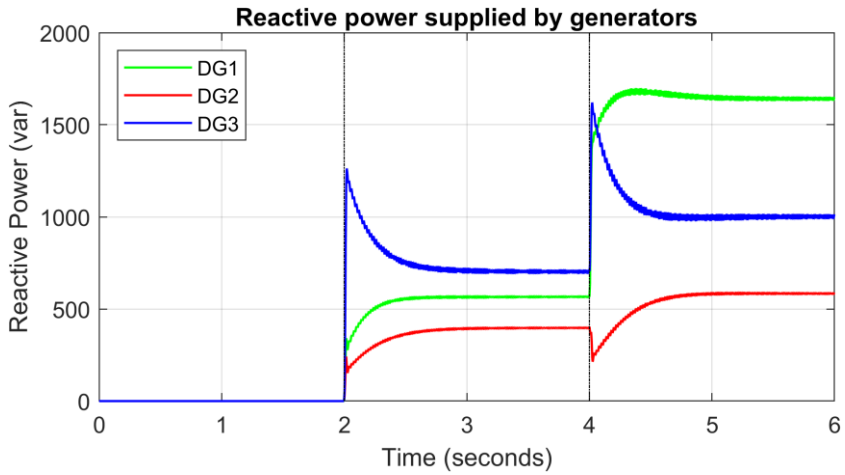

Figure 74 - Results of the simulation of the reactive power supplied by generators in island mode with primary control

b. Grid-connected mode

In grid-connected mode, the frequency is not modified since the frequency is a global variable and is fixed by the electrical grid, as shown in Figure 75. Nevertheless, the system contemplates transitory frequency deviations when the loads are connected. On the other hand, the amplitude displayed in Figure 76 shows more minor deviations than when the microgrid is in island mode. At the DG1, the amplitude deviation is greater than the other ones due to the microgrid distribution and the line impedance effect.

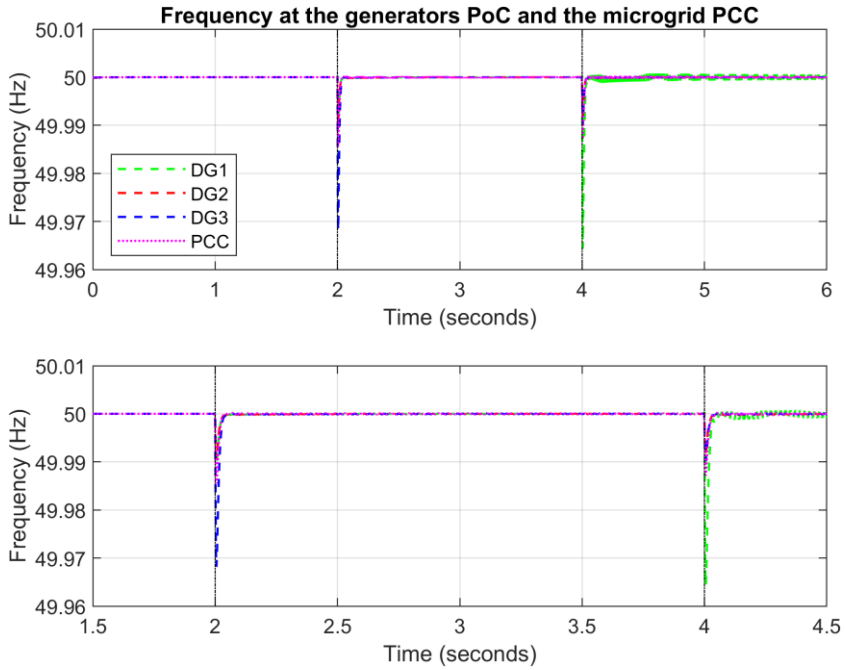

Figure 75 - Results of the simulation of the frequency at the generators PoC and the microgrid PCC in grid-connected mode with primary control

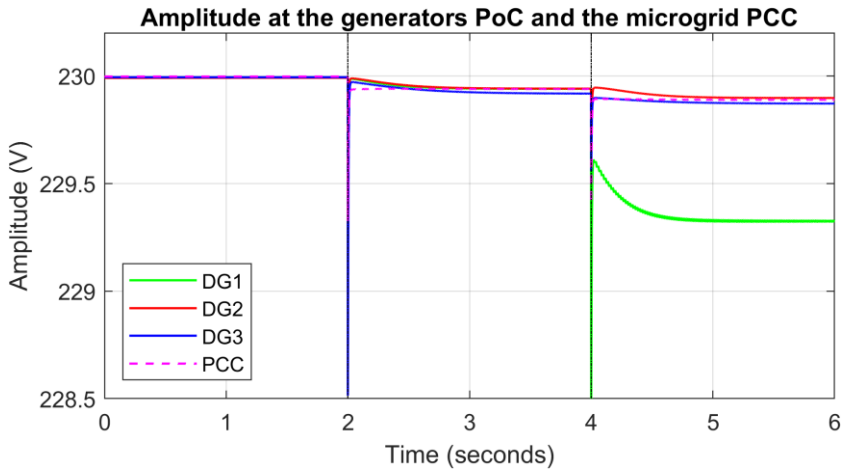

Figure 76 – Results of the simulation of the amplitude at the generators PoC and the microgrid PCC in grid-connected mode with primary control

In this instance, active power consumed by the loads is entirely supplied by the grid in steady state, as seen in Figure 77, and almost the same happens with the reactive power, as Figure 78 shows. The DG1 has a transient behaviour different to the others when the second load is connected due to the microgrid distribution line impedance.

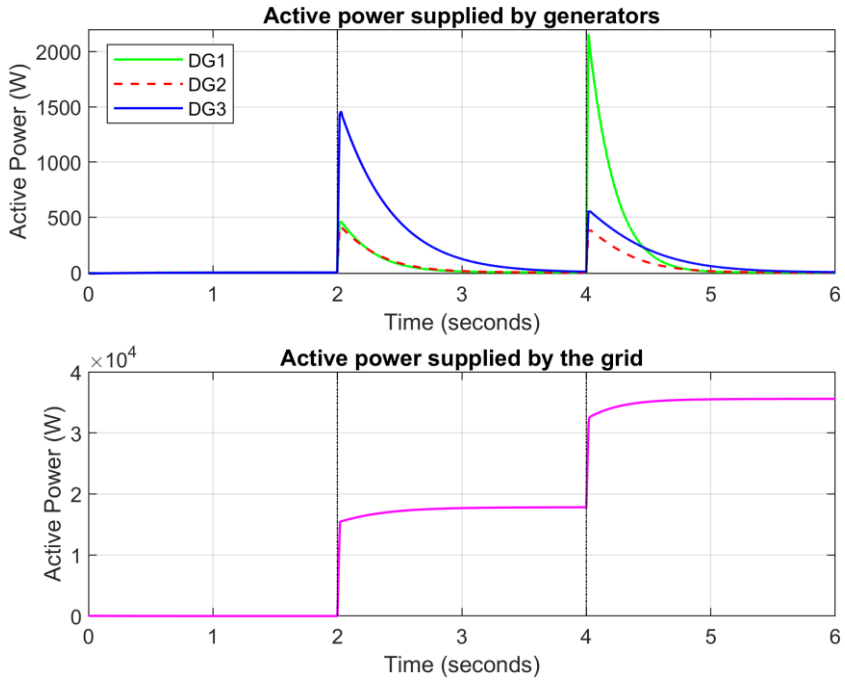

Figure 77 - Results of the simulation of the active power supplied by generators and grid in grid-connected mode with primary control

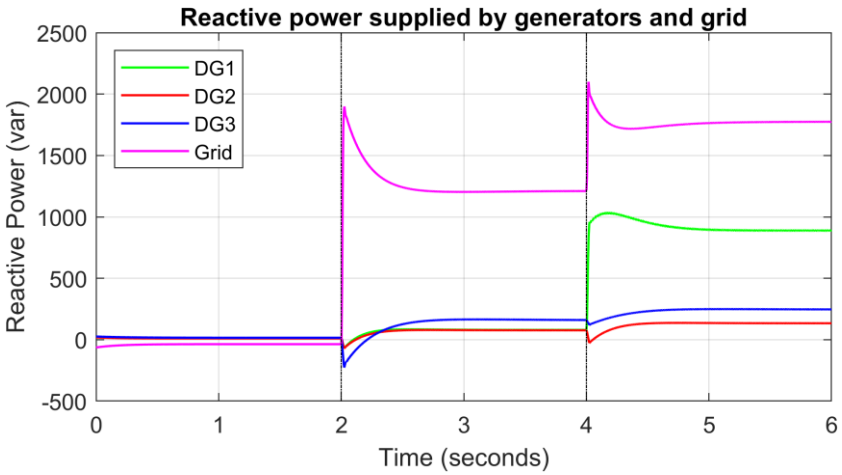

Figure 78 - Results of the simulation of the reactive power supplied by generators and grid in grid-connected mode with primary control

4.2.3. Secondary control

This subsection aims to study the microgrid voltage frequency and amplitude restoration. As done in the one generator setup, the secondary control is simulated by deactivating the tertiary control action. Both loads are connected in the second 0.5, and the secondary action is applied from the second 2.

a. Island mode

As shown in Figure 79, a frequency deviation is generated when the load is connected to the microgrid at second 0.5. Once the secondary control is activated, the frequency is restored after 8 seconds with a first-order behaviour as expected. The amplitude restoration is also achieved, as seen in Figure 80. Due to the impedance effect and the secondary control action applied in each DG, the behaviour is slower than expected, with a settling time of around 30 seconds.

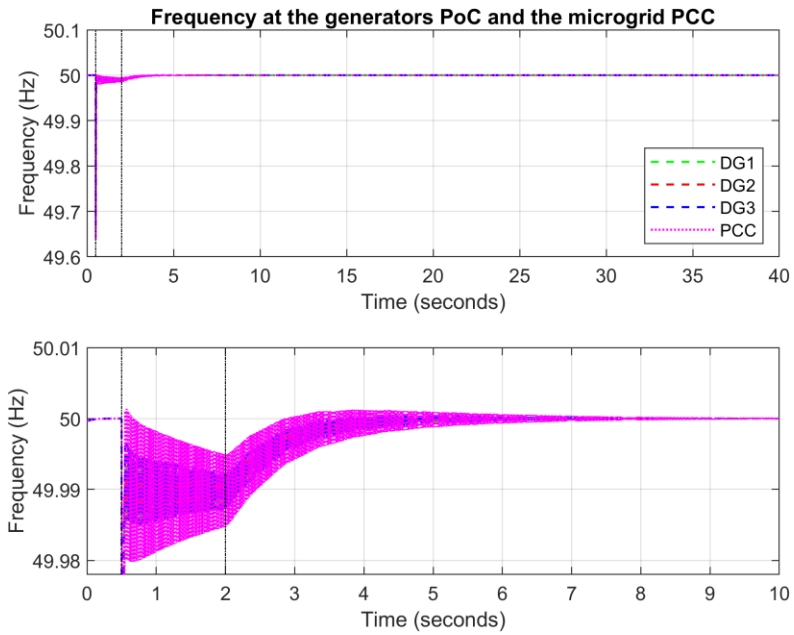

Figure 79 - Results of the simulation of the frequency at the generators PoC and the microgrid PCC in island mode with primary and secondary control

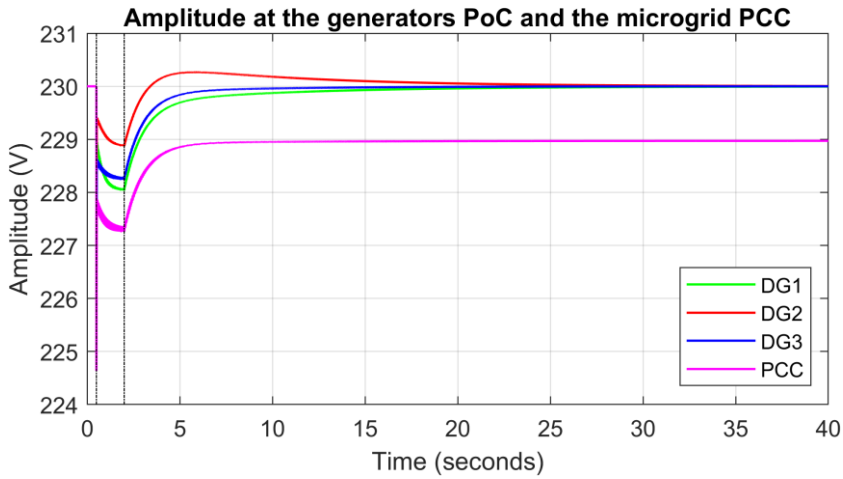

Figure 80 - Results of the simulation of the amplitude at the generators PoC and the microgrid PCC in island mode with primary and secondary control

The active power distribution is carried out correctly, following the same dynamics of the primary control as seen in Figure 81. Nevertheless, the amplitude restoration action worsens and delays the reactive power-sharing, as seen in Figure 82.

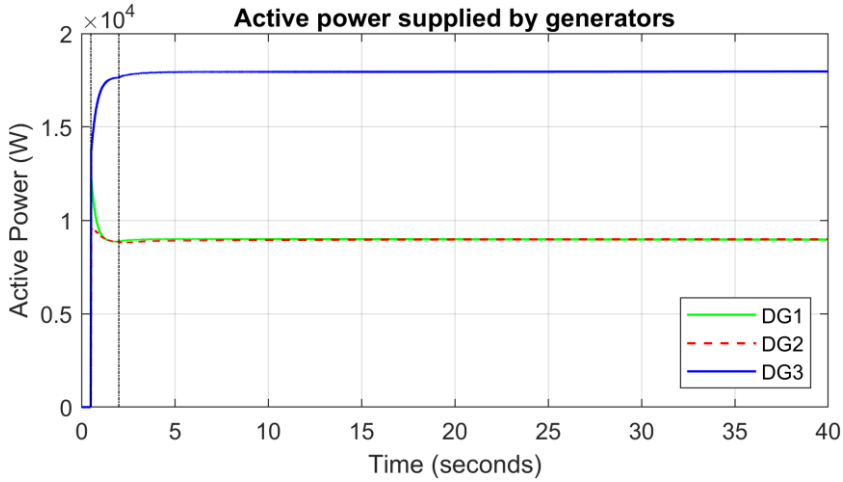

Figure 81 - Results of the simulation of the active power supplied by generators in island mode with primary and secondary control

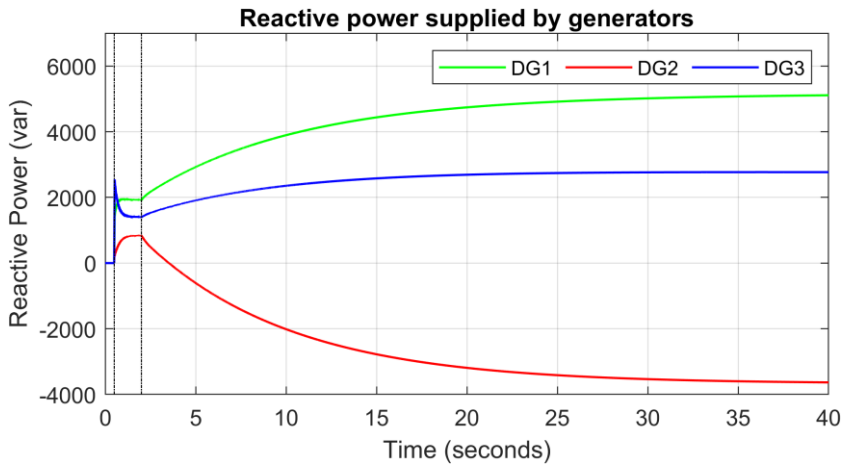

Figure 82 - Results of the simulation of the reactive power supplied by generators in island mode with primary and secondary control

b. Grid-connected mode

The system does not require the frequency restoration action in grid-connected mode since the frequency is fixed by the electrical grid and just contemplates transitory deviations when a load is connected, as seen in Figure 83. Besides that, the amplitude restoration action, shown in Figure 84, is achieved with a settling time of around 30 seconds as in the island mode.

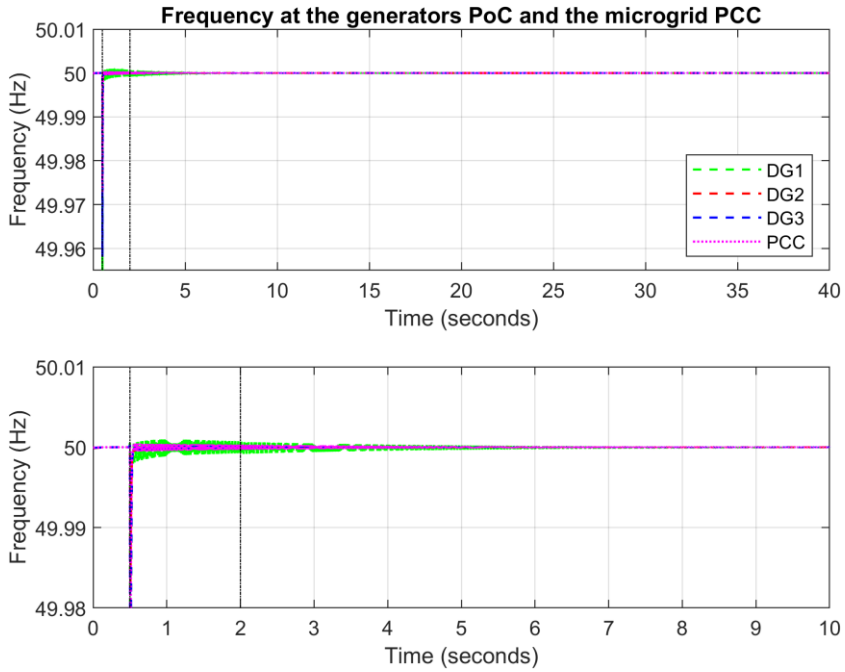

Figure 83 - Results of the simulation of the frequency at the generators PoC and the microgrid PCC in grid-connected mode with primary and secondary control

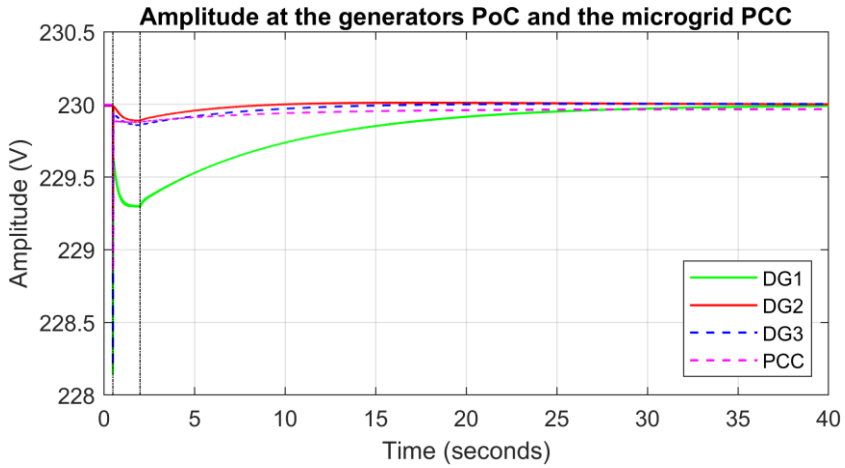

Figure 84 - Results of the simulation of the amplitude at the generators PoC and the microgrid PCC in grid-connected mode with primary and secondary control

If the grid is connected, most of the active power is supplied by it, as seen in Figure 85. Also, the amplitude restoration action worsens and delays the reactive power-sharing as seen in Figure 86.

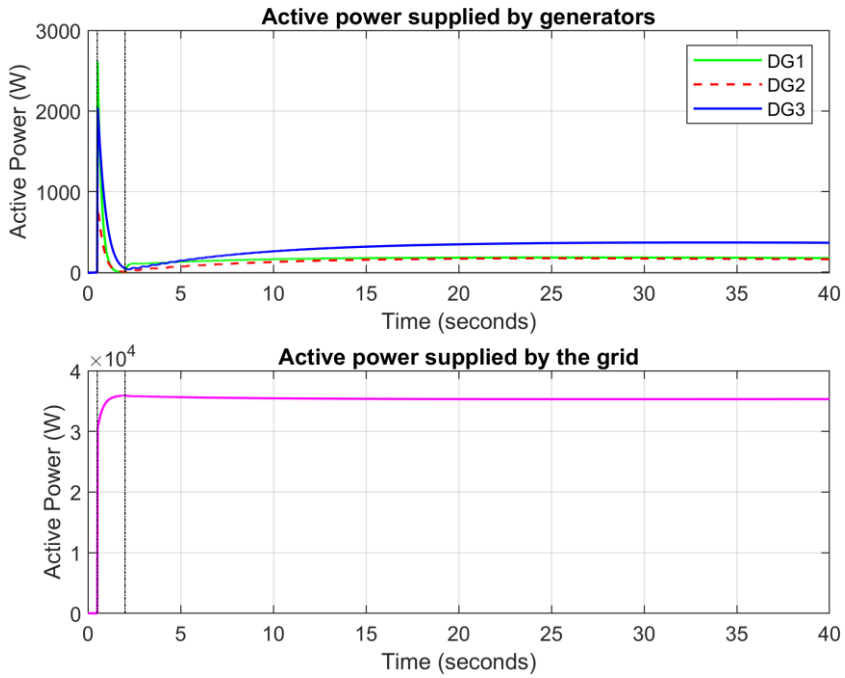

Figure 85 - Results of the simulation of the active power supplied by generators and grid in grid-connected mode with primary and secondary control

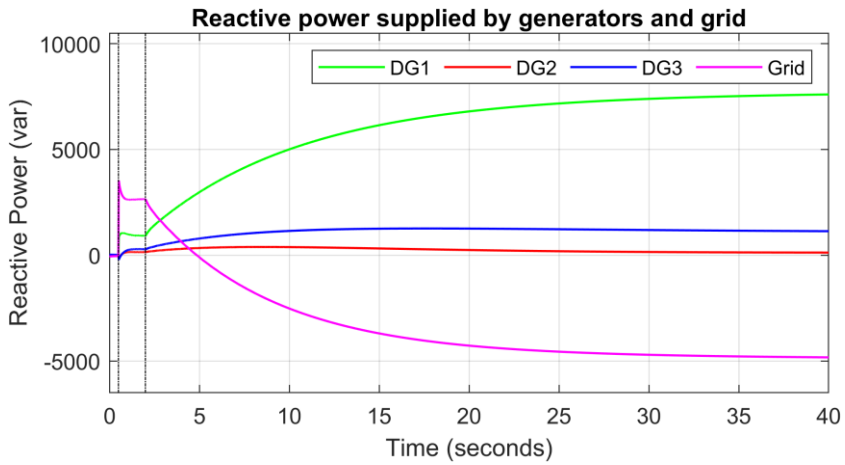

Figure 86 - Results of the simulation of the reactive power supplied by generators and grid in grid-connected mode with primary and secondary control

4.2.4. Tertiary control

The objective of this subsection is to study the tertiary control action with the microgrid setup. To do that, the secondary control is deactivated. Again, both loads are connected in the second 0.5, and the tertiary action is applied from the second 2. Besides, the simulations have been divided into two parts in which the power references are changed in the second 45 or second 120 depending on the operational mode, island mode and grid-connected mode, respectively.

a. Island mode

The following table shows the references applied in each part of this simulation:

Table 9 - Power references for the simulation of the tertiary control in island mode

Magnitude	*Value*	
	t = 0s	t = 45s
DG1 active power reference ($P1_{ref}$)	6000	10000
DG2 active power reference ($P2_{ref}$)	10000	10000
DG3 active power reference ($P3_{ref}$)	20000	16000
Grid active power reference ($Pgrid_{ref}$)	0	0
DG1 reactive power reference ($Q1_{ref}$)	1000	500
DG2 reactive power reference ($Q2_{ref}$)	1000	2000
DG3 reactive power reference ($Q3_{ref}$)	2000	1500
Grid reactive power reference ($Qgrid_{ref}$)	0	0

Figure 87 and Figure 88 show that the voltage frequency and amplitude contemplate a deviation from the nominal value due to the primary and tertiary control action.

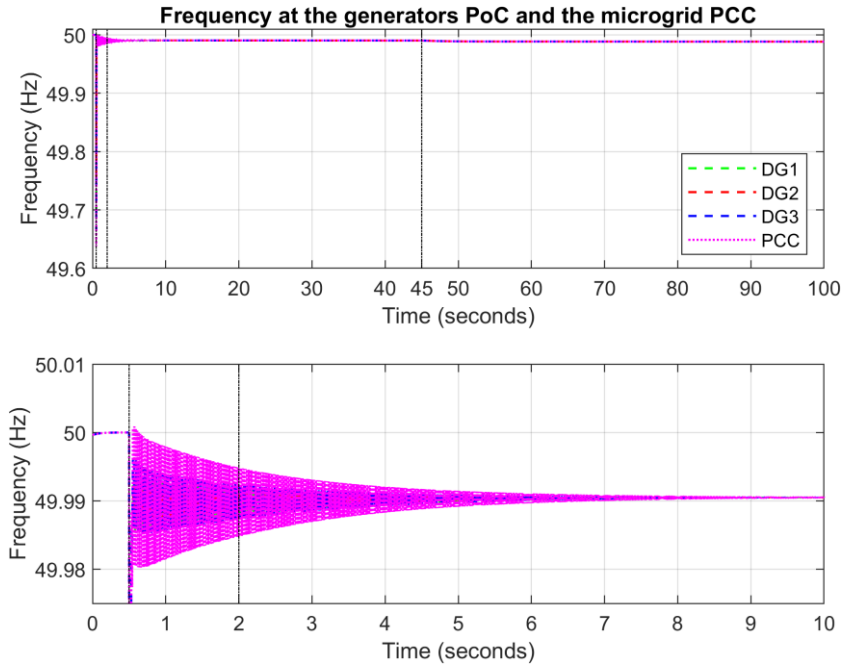

Figure 87 - Results of the simulation of the frequency at the generators PoC and the microgrid PCC in island mode with primary and tertiary control

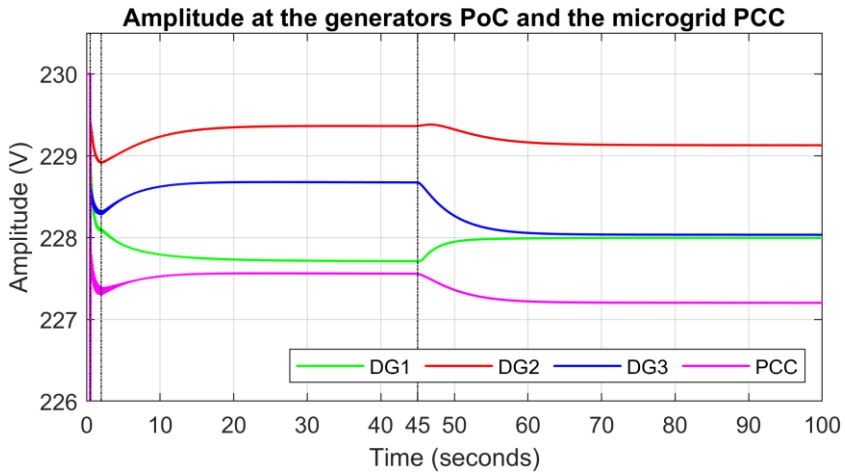

Figure 88 - Results of the simulation of the amplitude at the generators PoC and the microgrid PCC in island mode with primary and tertiary control

Regarding the active and reactive power, the system follows the references presented in Table 9. Figure 89 shows that in most cases, the response of the active power supplied by the generators follows a first-order behaviour with a settling time of 20 seconds which is faster than expected due to the joint action of the three generators. The same occurs with the reactive power, as seen in Figure 90.

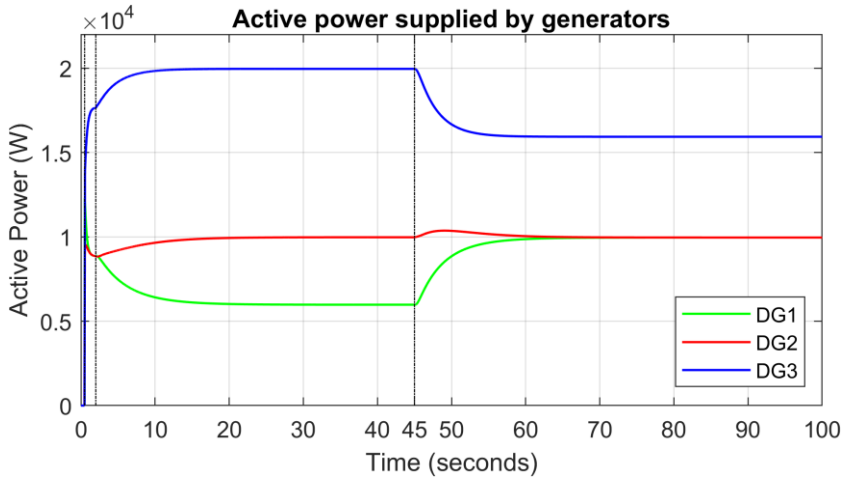

Figure 89 - Results of the simulation of the active power supplied by generators in island mode with primary and tertiary control

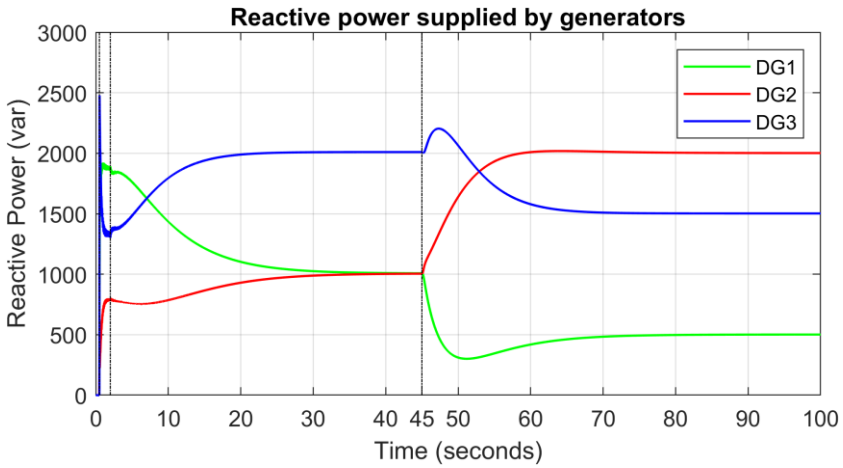

Figure 90 - Results of the simulation of the reactive power supplied by generators in island mode with primary and tertiary control

b. Grid-connected mode

The following table shows the references applied in each part of the simulation:

Table 10 - Power references for the simulation of the tertiary control in grid-connected mode

Magnitude	***Value***	
	t = 0s	**t = 120s**
DG1 active power reference ($P1_{ref}$)	2000	6000
DG2 active power reference ($P2_{ref}$)	4000	−10000
DG3 active power reference ($P3_{ref}$)	10000	15000
Grid active power reference ($Pgrid_{ref}$)	20000	25000
DG1 reactive power reference ($Q1_{ref}$)	300	1000
DG2 reactive power reference ($Q2_{ref}$)	700	500
DG3 reactive power reference ($Q3_{ref}$)	1000	1500
Grid reactive power reference ($Qgrid_{ref}$)	2000	1000

In this case, the frequency does not contemplate a deviation from the nominal value since the microgrid works in grid-connected mode, as displayed in Figure 91. However, the amplitude continues to perceive an error from the nominal value, as seen in Figure 92.

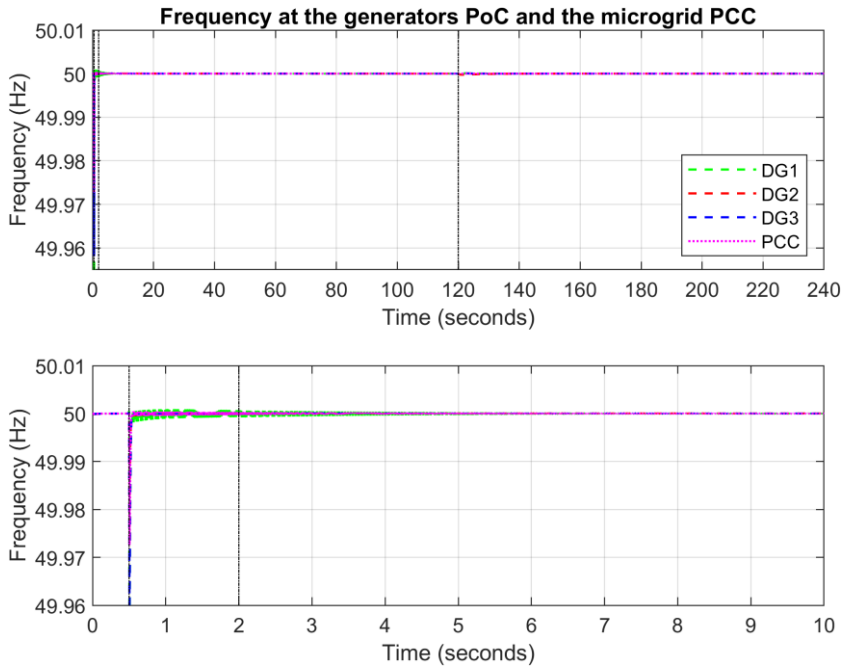

Figure 91 - Results of the simulation of the frequency at the generators PoC and the microgrid PCC in grid-connected mode with primary and tertiary control

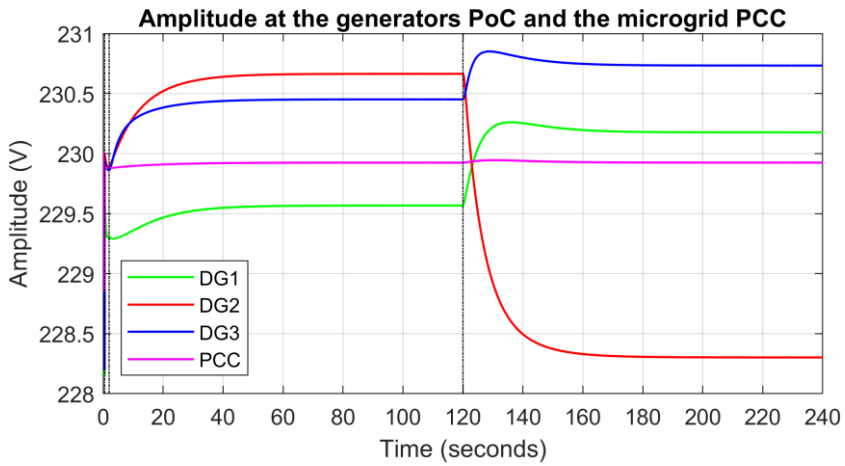

Figure 92 – Results of the simulation of the amplitude at the generators PoC and the microgrid PCC in grid-connected mode with primary and tertiary control

In grid-connected mode, the power flow is also achieved considering the references of Table 10. The behaviour of the active power flow of the system, displayed in Figure 93, have a settling time of around 60 seconds as expected, but in most cases, the response does not correspond to the expected behaviour.

The reactive power flow control is also achieved but does not have the expected behaviour with a settling time of around 100 seconds, as seen in Figure 94. These mismatches are caused by adding the grid power flow control and the coupling of both power controls.

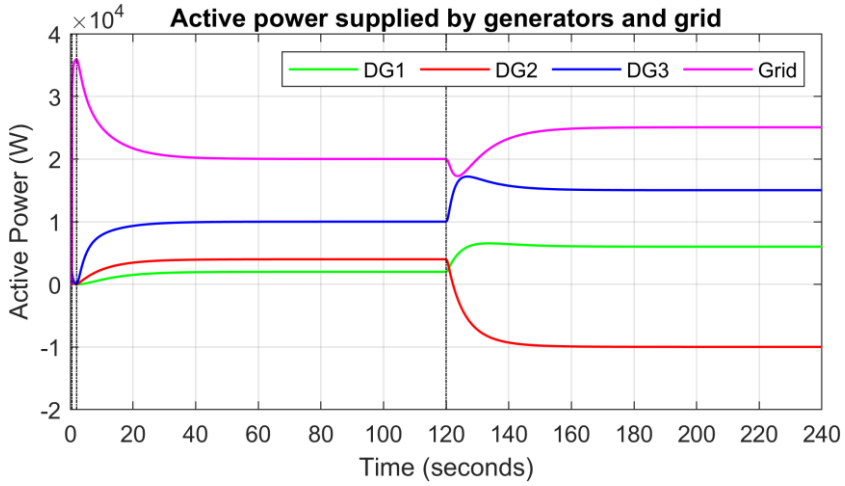

Figure 93 - Results of the simulation of the active power supplied by generators and grid in grid-connected mode with primary and tertiary control

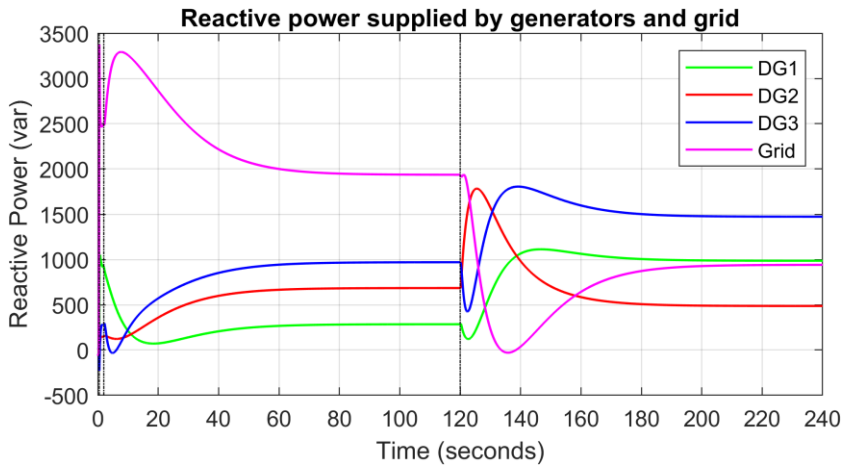

Figure 94 - Results of the simulation of the reactive power supplied by generators and grid in grid-connected mode with primary and tertiary control

4.2.5. Embedded control

Finally, the embedded control is studied in this subsection. In order to compare the results of the secondary and tertiary control with the results of the embedded control, the same tests are carried out. Thus, both loads are connected in the second 0.5, and the embedded control is applied from the second 2. Also, the references in Table 9 are considered for the island mode and the references in Table 10 for the grid-connected mode.

a. Island mode

In island mode, the frequency restoration is achieved with the expected behaviour and a settling time of around 8 seconds, as seen in Figure 95. This result is equal to the one observed in Figure 79. On the contrary, Figure 96 shows that the amplitude restoration is not accomplished when the secondary and tertiary control action are applied simultaneously. This permanent error is due to the already mentioned line impedance effect, and the analysis carried out in subsection 3.3.5 contemplates it. This error varies depending on the microgrid distribution.

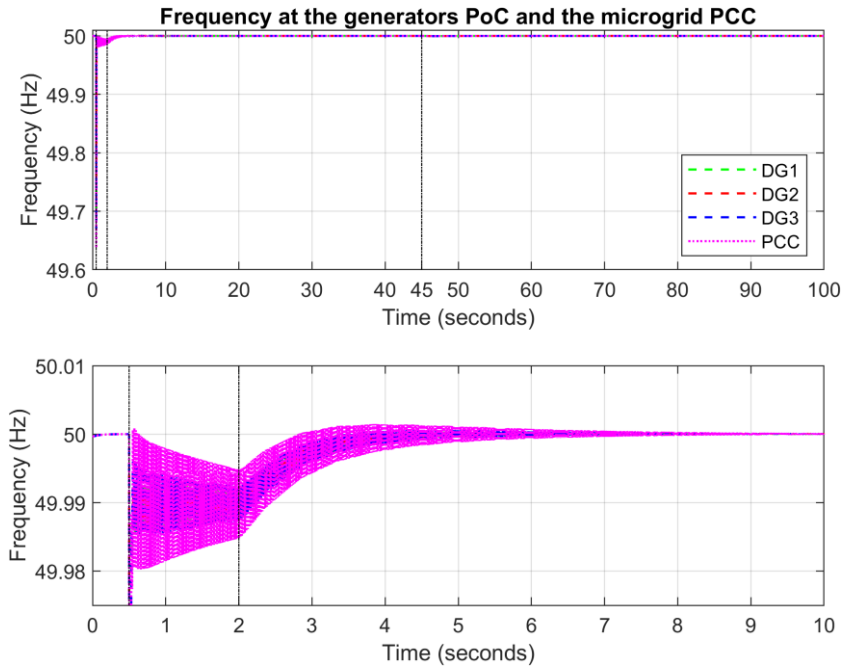

Figure 95 - Results of the simulation of the frequency at the generators PoC and the microgrid PCC in island mode with primary and embedded control

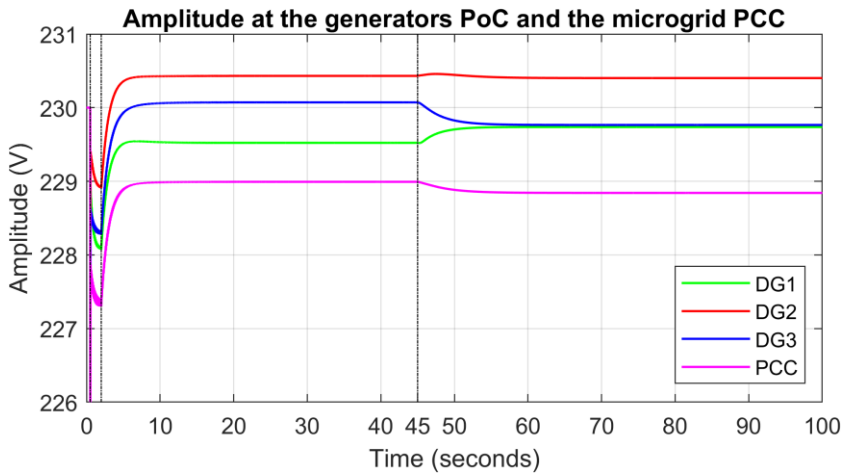

Figure 96 - Results of the simulation of the amplitude at the generators PoC and the microgrid PCC in island mode with primary and embedded control

Figure 97 shows that the active power flow is achieved considering the references in Table 9 and that in most cases, the response follows a first-order behaviour with a settling time of 20 seconds which is equal to the response obtained in Figure 89. However, the reactive power flow is not accomplished, as seen in Figure 98. This mismatch is caused by the same reason as the amplitude restoration.

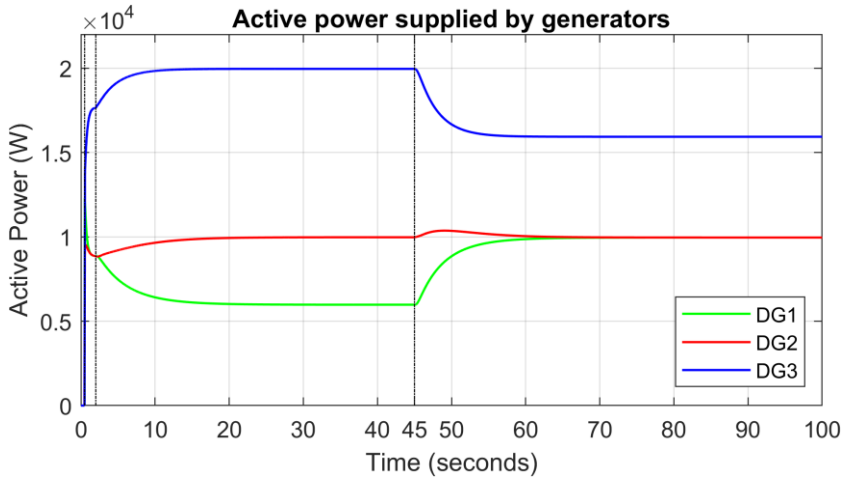

Figure 97 - Results of the simulation of the active power supplied by generators in island mode with primary and embedded control

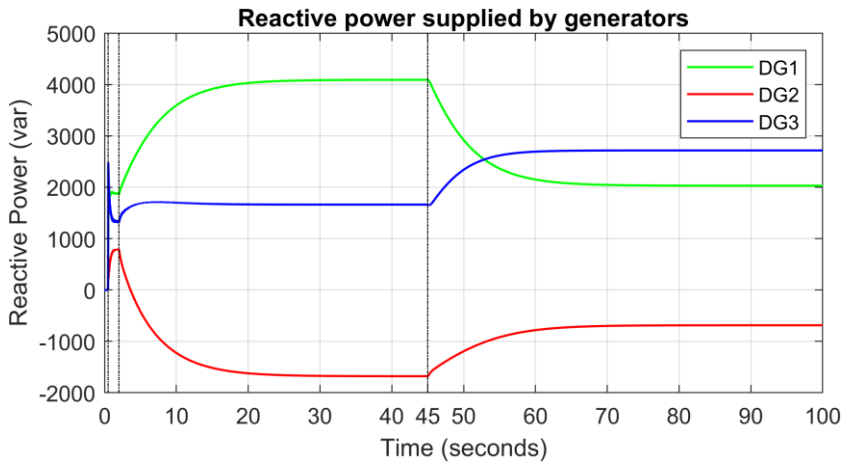

Figure 98 - Results of the simulation of the reactive power supplied by generators in island mode with primary and embedded control

b. Grid-connected mode

As mentioned, the system does not contemplate frequency deviations when the microgrid works in grid-connected mode, as Figure 99 shows. On the other hand, the amplitude deviation is contemplated, as seen in Figure 100. As in the island mode and considering the results of the analysis of subsection 3.3.5, the amplitude restoration is also not achieved. The error of each DG depends on the microgrid distribution.

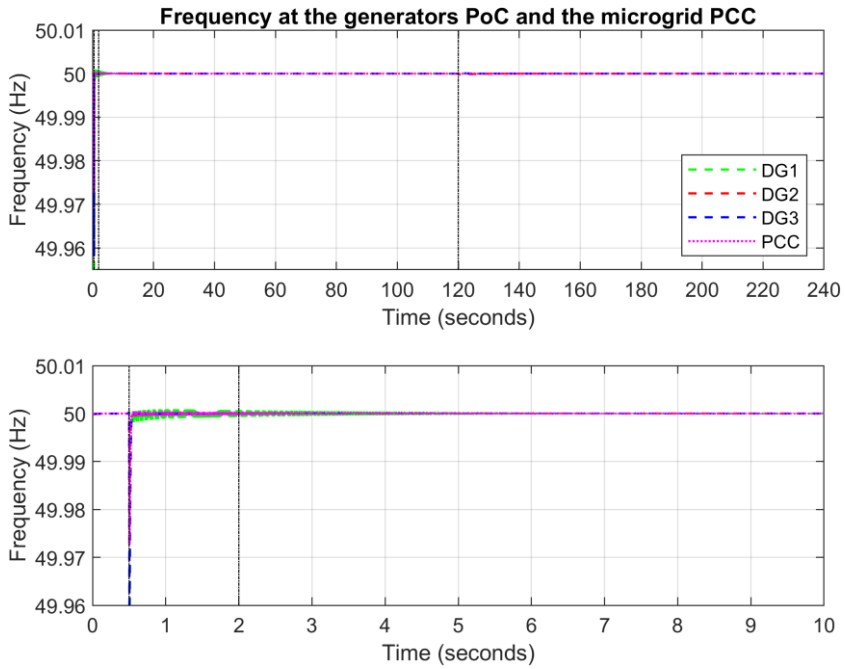

Figure 99 - Results of the simulation of the frequency at the generators PoC and the microgrid PCC in grid-connected mode with primary and embedded control

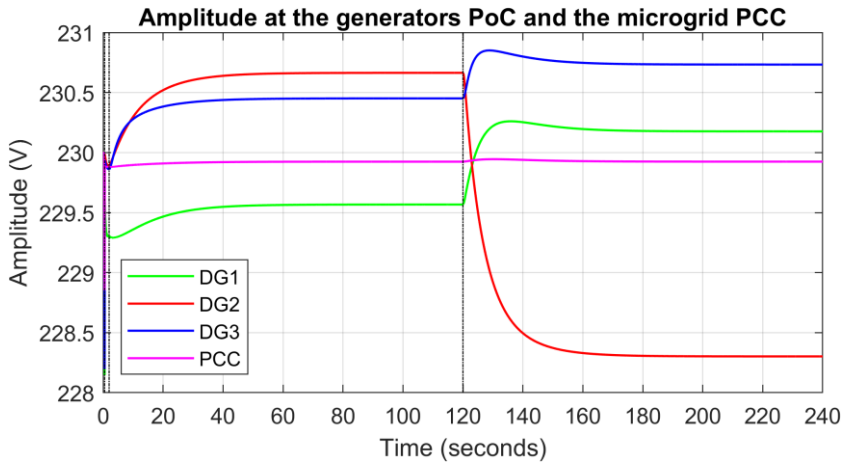

Figure 100 - Results of the simulation of the amplitude at the generators PoC and the microgrid PCC in grid-connected mode with primary and embedded control

Figure 97 shows that the active power flow is achieved considering the references of Table 10 and that in most cases, the response follows a first-order behaviour with a settling time of 60 seconds which is equal to the response obtained in Figure 93. However, the reactive power flow is not accomplished, as seen in Figure 102. This mismatch is caused by the same reason as the amplitude restoration.

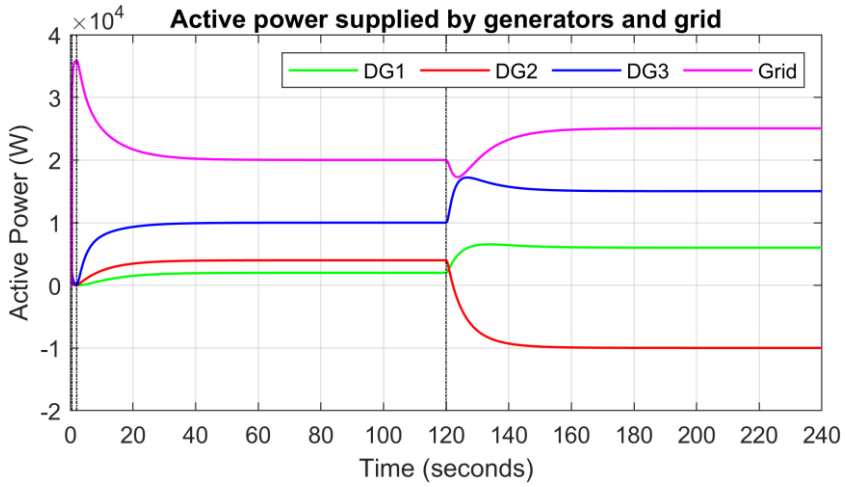

Figure 101 - Results of the simulation of the active power supplied by generators and grid in grid-connected mode with primary and embedded control

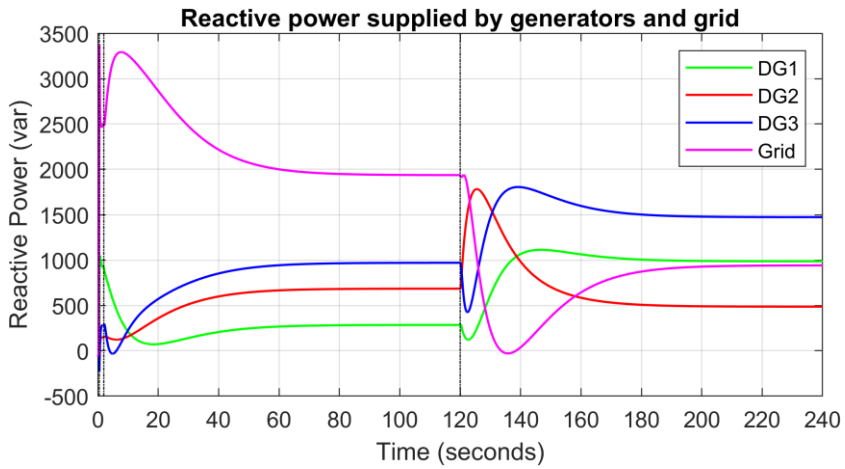

Figure 102 - Results of the simulation of the reactive power supplied by generators and grid in grid-connected mode with primary and embedded control

5. Budget

The budget study has been carried out by deeming certain aspects that considerably reduce the total amount planned. First, the project scope ends in the simulation of the proposed control and no hardware components have been developed or implemented. On the other hand, the simulation and calculation programs with a license without expiration and the computer used to develop the thesis are considered to have an amortization time of 60 months. Since the duration of this thesis has been of around 9 months, the corresponding values are calculated following the next equation:

$$AmortizedValue = \frac{9months}{60months} \cdot TotalValue \tag{5.1}$$

Finally, the budget has been calculated by splitting it into two parts. The first part contemplates the human resources budget, shown in Table 11, whereas
Table 12 displays the used software and required computer cost.

Table 11 - Human resources budget

Price per hour	**15€/hour**
Hours spent	900 hours
Human resources budget	**13500€**

Table 12 - Software and computer budget

Concept	**Value**	**Amortized value**
Computer	700€	105€
MATLAB (Educational)	1200€/*year*	900€
Maple (Educational Single-user License)	1000€	150€
PLECS	1200€	180€
Microsoft 365	99€/year	74.25€
Software budget		**1409.25€**

Finally, Table 13 summarizes both tables and shows the total cost of the thesis, being the human resources budget the 90% of this cost.

Table 13 - Total budget

Human resources budget	**13500€**
Software budget	1409.25€
Total	**14909.25€**

6. Conclusions and future development

6.1. Summary

The control of an AC microgrid based on a distributed hierarchical control, with the feature of having the secondary and tertiary control embedded and allowing the microgrid elements to work as voltage sources at any time, has been designed and simulated.

During the initial stage of the master's thesis, the microgrid concept is presented and studied for the purpose of starting to refer to the AC microgrid hierarchical control. Once the principal topics have been introduced, the main objectives to be achieved and the project's planning are explained. Furthermore, since this thesis is focused on the design of hierarchical control, the research of its principles and the three layers which compose it, primary, secondary and tertiary control, is carried out.

In the second phase of the document, the proposed AC microgrid hierarchical control is explained and designed. Firstly, the AC microgrid system under study is presented to subsequently explain the control law on which the proposed control approach is based. Then, the design of all the layers is performed by taking some assumptions to simplify the study, such as deeming a system with a single generator, applying the regulation and employing stability and dynamics analysis. Overall, the objective has been to obtain a first-order response for the primary, secondary and tertiary control with a time constant as fast as possible, of 1 second and 10 seconds, respectively. Finally, the last part of this stage consists of unifying the considered control loops of the secondary and tertiary control and studying their behaviour depending on the control parameter values selected.

The final section is focused on the simulation and validation of the realized calculations. For that purpose, two simulation setups have been developed. On the one hand, a simulation model that characterises a single generator is developed to verify the considered assumptions in the control design chapter. On the other hand, the proposed hierarchical control is applied to a model that defines the AC microgrid under study in both operating modes and functional analysis is performed.

6.2. Conclusions

The hierarchical control approach proposed and developed in this document partially meets the technical objectives. The conclusions reached are the outcome of comparing the simulation results with the expected response obtained when designing the control.

Regarding the primary control, the active power sharing meets the expected first-order response with a settling time of 1 second, considering the single generator and the microgrid setup. However, the reactive power sharing partially follows the expected behaviour. In general, the response is stable and follows a first-order response with a settling time of 1 second, but the steady-state error obtained in the simulations is greater than expected. This is due to the plant's transfer function used to design the reactive power control loops that assume the line to be only inductive and does not consider the resistive component.

The secondary control meets the expected voltage frequency and amplitude restoration response being in most cases of first order with a settling time of 8 seconds. Moreover, the expected active power flow performed by the tertiary control is achieved in the one generator setup and when the microgrid setup works in grid-connected mode, being first-

order responses with a setting time of 60 seconds. In the case where the microgrid works in island mode, the active power flow is achieved in 20 seconds faster than expected. This deviation is caused by the complexity of the system and the considerations done during the design. About the reactive power flow, the results are generally not as expected. Although all the responses are stable and follow the reactive power references, in most cases, the response is slower and with a different behaviour as planned. In the one converter setup, the response follows the reference and a first-order response, but it is slower than expected. Whereas in the microgrid setup, the responses meet the set points but do not follow the expected behaviour in any mode.

Finally, the unification of the secondary and tertiary control entails two modifications to the original control. On the one hand, a delay in the active power control flow is applied. On the other hand, a conflict between the amplitude restoration and the reactive power flow appears, adding permanent error in each control depending on their weight.

Despite all these inconveniences, the proposed control allows the microgrid generators to work as voltage sources in both operating modes.

6.3. Future development

The possible futures lines of development to achieve a better behaviour and a better controllability level for the microgrid can be the consideration of the existing coupling between the P-ω and Q-E control loops, the tunning of the control by considering all the microgrids generators instead of tuning the controller for only one DER. Other improvements consist of considering the line impedances between generators. And finally, it can be crucial to consider the dynamics of the internal control loops.

Bibliography

[1] I. E. Agency, “Global Energy Review 2021,” 2022. [Online]. Available: https://iea.blob.core.windows.net/assets/d0031107-401d-4a2f-a48b-9eed19457335/GlobalEnergyReview2021.pdf.

[2] R. E. de España, “El sistema eléctrico español Avance 2021,” 2022. [Online]. Available: https://www.ree.es/sites/default/files/publication/2022/03/downloadable/Avance_ISE_2021.pdf.

[3] R. H. Lasseter, “MicroGrids,” in *2002 IEEE Power Engineering Society Winter Meeting. Conference Proceedings (Cat. No.02CH37309)*, 2002, vol. 1, pp. 305–308, doi: 10.1109/PESW.2002.985003.

[4] IEEE, *IEEE Standard for the Testing of Microgrid Controllers*. 2018.

[5] A. Mehrizi-Sani and R. Iravani, “Potential-Function Based Control of a Microgrid in Islanded and Grid-Connected Modes,” *IEEE Trans. Power Syst.*, vol. 25, no. 4, pp. 1883–1891, Nov. 2010, doi: 10.1109/TPWRS.2010.2045773.

[6] D. Heredero Peris, “Control contributions to AC microgrid inverters,” 2017.

[7] G. Venkataramanan and C. Marnay, “A larger role for microgrids,” *IEEE Power Energy Mag.*, vol. 6, no. 3, pp. 78–82, May 2008, doi: 10.1109/MPE.2008.918720.

[8] P. Ledesma, *Regulación de frecuencia y potencia*. 2008.

[9] S. M. Kaviri, M. Pahlevani, P. Jain, and A. Bakhshai, “A review of AC microgrid control methods,” in *2017 IEEE 8th International Symposium on Power Electronics for Distributed Generation Systems (PEDG)*, Apr. 2017, vol. 27, no. 11, pp. 1–8, doi: 10.1109/PEDG.2017.7972498.

[10] V. Nasirian, Q. Shafiee, J. M. Guerrero, F. L. Lewis, and A. Davoudi, “Droop-Free Distributed Control for AC Microgrids,” *IEEE Trans. Power Electron.*, vol. 31, no. 2, pp. 1600–1617, Feb. 2016, doi: 10.1109/TPEL.2015.2414457.

[11] K. De Brabandere, B. Bolsens, J. Van den Keybus, A. Woyte, J. Driesen, and R. Belmans, “A Voltage and Frequency Droop Control Method for Parallel Inverters,” *IEEE Trans. Power Electron.*, vol. 22, no. 4, pp. 1107–1115, Jul. 2007, doi: 10.1109/TPEL.2007.900456.

[12] H. Jiang, V. Kumtepeli, D. D. Nguyen, A. Tripathi, and Y. Wang, “Secondary Reactive Power Balancing and Voltage Stability in Microgrid Using Prioritized Centralized Controller,” in *2018 IEEE Innovative Smart Grid Technologies - Asia (ISGT Asia)*, May 2018, pp. 1209–1214, doi: 10.1109/ISGT-Asia.2018.8467882.

[13] E. Espina, J. Llanos, C. Burgos-Mellado, R. Cardenas-Dobson, M. Martinez-Gomez, and D. Saez, “Distributed Control Strategies for Microgrids: An Overview,” *IEEE Access*, vol. 8, pp. 193412–193448, 2020, doi: 10.1109/ACCESS.2020.3032378.

[14] A. C. Zambroni de Souza and M. Castilla, *Microgrids Design and Implementation*. Cham: Springer International Publishing, 2019.

[15] Y. Khayat *et al.*, “On the Secondary Control Architectures of AC Microgrids: An Overview,” *IEEE Trans. Power Electron.*, vol. 35, no. 6, pp. 6482–6500, Jun. 2020, doi: 10.1109/TPEL.2019.2951694.

[16] Q. Shafiee, C. Stefanovic, T. Dragicevic, P. Popovski, J. C. Vasquez, and J. M. Guerrero, “Robust Networked Control Scheme for Distributed Secondary Control of Islanded Microgrids,” *IEEE Trans. Ind. Electron.*, vol. 61, no. 10, pp. 5363–5374, Oct.

2014, doi: 10.1109/TIE.2013.2293711.

[17] J. W. Simpson-Porco, Q. Shafiee, F. Dorfler, J. C. Vasquez, J. M. Guerrero, and F. Bullo, “Secondary Frequency and Voltage Control of Islanded Microgrids via Distributed Averaging,” *IEEE Trans. Ind. Electron.*, vol. 62, no. 11, pp. 7025–7038, Nov. 2015, doi: 10.1109/TIE.2015.2436879.

[18] J. M. Guerrero, J. C. Vasquez, J. Matas, L. G. De Vicuña, and M. Castilla, “Hierarchical control of droop-controlled AC and DC microgrids - A general approach toward standardization,” *IEEE Trans. Ind. Electron.*, vol. 58, no. 1, pp. 158–172, Jan. 2011, doi: 10.1109/TIE.2010.2066534.

[19] K. De Brabandere, “Voltage and Frequency Droop Control in Low Voltage Grids by Distributed Generators with Inverter Front-End,” 2006.

Glossary

AC	Alternating Current
CL	Closed Loop
DC	Direct Current
DER	Distributed Energy Resources
DG	Distributed Generator
DS	Distributed Storage Elements
LPF	Low Pass Filter
MAS	Multi Agent System
MGCC	Microgrid Central Controller
MISO	Multiple Input, Single Output
OP	Open Loop
PLL	Phase-Locked Loop
PCC	Point of Common Coupling
PoC	Point of Coupling
RL	Resistor-Inductor
SISO	Single Input, Single Output
SSE	Steady-State Error